Picoseconds and femtoseconds Ytterbium fiber laser sources and its applications

Muhammad Ghawas

université de BORDEAUX

université de BORDEAUX

THÈSE PRÉSENTÉE

POUR OBTENIR LE GRADE DE

DOCTEUR
DE L'UNIVERSITÉ DE BORDEAUX

ÉCOLE DOCTORALE DES SCIENCES PHYSIQUE ET DE L'INGÉNIEUR

SPECIALITÉS: Lasers, Matière, Nanoscience

Par **Muhammad GHAWAS**

Sources picosecondes et femtosecondes à base de fibre dopées Ytterbium et applications

Sous la direction de: **Eric FREYSZ**
Co-directeur: **Jérôme DEGERT**

Soutenue le **20 Décembre 2023**

MEMBRES DU JURY

M. Jean OBERLÉ	Professeur	Université de Bordeaux	Président
M. Arnaud MUSSOT	Professeur	Université de Lille	Rapporteur
M. Philippe ROY	Directeur de Recherche	Université de Limoges	Rapporteur
M. Eric FREYSZ	Directeur de Recherche	Université de Bordeaux	Directeur de Thése

Acknowledgment

First and foremost, I wish to express my gratitude to Allah the Almighty, the Most Gracious, and the Most Merciful, for His blessings throughout my life and also in my PhD journey.

I would like to convey my deepest appreciation to my Ph.D. supervisor, Prof. Eric FRESYZ, for his steadfast dedication and continuous guidance throughout my Ph.D. journey. His constant support, always ahead of time, has really helped me deal with the complicated parts of my research work. He always gave really helpful advice and came up with clever solutions to any problems I faced, making sure nothing was too difficult to overcome. Without his support, this Ph.D. journey would have been an insurmountable task. Beyond his exceptional academic mentorship, I am truly grateful for his kind and compassionate attitude, which has made the journey not only intellectually enriching but also personally rewarding. Thanks a lot, Eric! I would also like to extend my gratitude to my co-supervisor, Prof. Jérôme DEGERT, for his guidance, particularly during our group meetings, and for his assistance in reviewing publications and the thesis manuscript. Additionally, I appreciate his support in preparing my thesis presentation.

I also wish to express many thanks to the jury members Prof. Arnaud MUSSOT, Prof. Philippe ROY, and Prof. Jean OBERLÉ for their meticulous review of my thesis work and for providing valuable suggestions throughout the evaluation process and during the thesis defense discussions. Their expertise and insights greatly contributed to the refinement of my research findings. I am truly appreciative of their time and dedication to this endeavor.

I would like to extend my heartfelt appreciation to all my colleagues at LOMA, particularly the PULS team, including Emmanuel ABRAHAM, Laetitia DALSTEIN, Gabriel AMIARD HUDEBINE, Amine OULD HAMOUDA, Olivia ZURITA-MIRANDA, Martin MAILLARD, Valerian FREYSZ, and Mathias HEDEGAARD KRISTENSEN. The collaborative atmosphere fostered in our group meetings and discussions has been vital in broadening my knowledge base. Their insightful questions and suggestions during my group presentations have helped me to stay updated with the latest developments in the field. I am extremely grateful to Valerian for his support at the start of my Ph.D. and throughout its progression. His assistance in providing the necessary components for our experiments has been invaluable. I am also thankful to Olivia for the fruitful discussions regarding the fiber OPO work. Furthermore, I would like to express my thanks to Martin, Gabriel, and especially Laetitia for their assistance with administrative documentation in French throughout my doctoral studies. Laetitia's support in arranging appointments with doctors for my wife during her pregnancy in my final year of Ph.D. is particularly appreciated. I am truly thankful to the entire group for creating memorable experiences during

my time at LOMA.

This doctoral research was conducted in collaboration with the EU Horizon program, ITN-GREAT. I wish to extend my appreciation to all my colleagues at GREAT for their contributions to our successful collaboration, organizing meetings, and offering important suggestions during consortium presentations. The insightful recommendations provided were truly commendable. I am particularly grateful to Dr. Marwan ABDOU AHMED for providing the Gratings for our experiments.

Life beyond LOMA would have lacked excitement without the presence of friends, and I am highly obliged to all those who made my Ph.D. journey truly enjoyable. I extend my gratitude to Muhammad ARSHAD, Samlan CHANDRAN THODIKA, Muhammed Rasi MALACKOTH, and numerous others from the cricketing circle whose names are too many to list individually. Additionally, I am grateful to all my DOTA companions, particularly Abdullah Bhatti, Umair Zeb, Asad Munir, Bilal Ahmed, and Tanseef Shahid, for adding laughter during weekends. Your company has truly made these times enjoyable. And to my DOTA friends, you all may be noobs, but you have certainly added a lot of fun to my weekends.

I am immensely grateful to express my gratitude to my dear father, Amir Khan, and mother, Zohra, for their endless support throughout my Ph.D. journey, despite the physical distance that separated us. Their continuous prayers and moral encouragement served as a constant source of motivation, empowering me to complete my studies and stay in a foreign country successfully. I would also like to thank my siblings (Abbas, Rabia, Eman, Haseena, Sidra, and Amna), whose support played a crucial role in making this journey a fulfilling and rewarding experience. Together, their love and encouragement have been instrumental in my academic achievements, and I am truly fortunate to have such a supportive family.

Last but not least, I express my gratitude to my spouse, Saira, for her unwavering support, enabling me to manage extensive work hours while maintaining a harmonious family life. Particularly in the last year, with the arrival of our son, Abulhaisam, she exerted considerable effort to ensure the seamless coordination of all responsibilities within a tight schedule.

Contents

List of Figures

List of Tables

Table of abbreviations and acronyms

LASER	*Light amplification by stimulated emission of radiation*
HRM	*High reflecting mirror*
PRM	*Partial reflecting mirror*
DM	*Dichroic mirror*
UV,MIR	*Ultraviolet, Mid-Infrared*
AML,PML	Active mode-locking, Passive mode-locking
FWHM	*Full width at Half-maximum*
ANDi	*All-normal Dispersion*
SA	*Saturable absorber*
FWM	*Four-Wave-Mixing*
OPO	*Optical Parametric Oscillator*
FOPO	*Fiber Optical Parametric Oscillator*
ZDW	*Zero Dispersion Wavelength*
PM	*Polarization maintaining*
PCF	*Photonic crystal fiber*
NPR	*Nonlinear polarization rotation*
GVD	*Group velocity dispersion*
GDD	*Group delay dispersion*
SPM	*Self phase modulation*
XPM	*Cross phase modulation*
GWS	*Grating waveguide structure*

Introduction

Ultrafast optics is the branch of physics regarding the generation and manipulation of light pulses on extremely short timescales, typically picosecond (ps) or lower pulse duration. One of the frequently employed methods for generating these short pulse durations involves the utilization of mode-locking [1]. The using of ultrashort laser pulses in both industrial and research applications progressively relies on fiber laser technology, guided by its intrinsic benefits, for instance, stability, compact nature, excellent beam quality, robustness, and easy operation [2]. Initially, the generation of ultrashort pulses in fiber involved employing solitons, which was the balance between the fiber nonlinearity and the anomalous dispersion. But the main limitation of soliton fiber laser was the lower pulse energies, usually in the range of a few hundred picojoules (pJ), and that higher pulse energies will lead to pulse breaking due to increased nonlinearity [3]. To overcome this, different techniques were proposed to achieve higher pulse energies, for instance, stretched pulse fiber laser [4], and self-similar laser [5]. Consequently, all-normal dispersion (ANDi) fiber lasers were proposed [6, 7] which allows to achieve much higher pulse energies (several tens of nanojoules-nJ) compared to conventional soliton lasers. Subsequently, thanks to advancements in high-power pump diodes, the evolution of large mode area (LMA), and photonic crystal fibers (PCFs), mode-locked fiber lasers have achieved the capability to generate pulses with higher energies and short duration [8–12]. Fiber laser uses encompass a range of applications, including but not limited to, spectroscopy [13], nonlinear microscopy and imaging [14–19], supercontinuum generation [20], seed source for optical parametric oscillator [21], and many more. However, for the mentioned applications, the optimal solution involves having a tunable laser operation where one can adjust both the central wavelength and the pulse width as needed.

Recent advancements in tunable fiber lasers and tunable fiber OPO

Tunable ultrashort pulses are widely employed for research and industrial uses, particularly in the field of biomedical applications [22–26]. In the past, when tunable ultrashort pulses were obtained using traditional solid-state mode-locked lasers, for instance using the Ti: Sapphire laser [27], there has been a notable shift towards the predominant utilization of fiber lasers [28] for tunable operation. This shift is attributed to their practical advantages, affordability, stability, compact design, and high-power performance. For applications in the biomedical field especially for coherent Raman imaging applications where large tunability of the central wavelength is required [17], fiber lasers demonstrate a small tuning range due to their limited gain bandwidth [29]. The fundamental concept underlying coherent Raman imaging involves the utilization of stimulated Raman scattering, as extensively explained in the Discussion and Conclusion (Chapter 6). This technique requires two laser sources, with at least one of them being widely tunable in central wavelength to encompass the entire fingerprint region of the Raman shifts for the analyzed biomedical sample [30]. For this purpose, we initially constructed a tunable laser source operating in the vicinity of 1 µm, relying on rod-type ytterbium-doped fiber [31]. Subsequently, we used this laser source as a pump for the development of a tunable fiber optical parametric oscillator (OPO) based on photonic crystal fiber, to broaden the wavelength range towards lower spectral regions (750 nm – 1000 nm). The following sections will provide a brief overview of the current advancements in both laser technologies.

Tunable fiber laser

This section will only discuss state-of-the-art tunable fiber lasers based on ytterbium-doped fiber. The utilization of ytterbium fiber, due to its broad gain bandwidth and low quantum defect [32, 33], is widely favored to generate high-power ultrashort tunable pulses near

1 µm for biomedical applications [34–36]. In response to these requirements, various laser designs have explored tunable yb-doped mode-locked fiber lasers [37–40]. The tunability achieved by tilting the grating and mirror geometry obtains a broad tuning range of 90 nm (980 nm to 1070 nm) but the average power output is limited to the milliwatt level (mW) throughout the entire tuning range [37]. By adjusting the intracavity interference filter in an ANDi laser cavity, a tuning range of almost 35 nm around 1030 nm was achieved. Here again, the maximum output average power was around 150 mW [38]. Likewise, a tuning span of $\sim$ 20 nm and $\sim$ 46 nm, by adjusting Sagnac loop interferometer filter [40] and birefringent filter [39] respectively, in the ANDi laser cavity. Similarly, in these laser cavities, nJ pulses were achieved with the maximum output average power of $\sim$ 25 mW and $\sim$ 60 mW, respectively. Subsequently, different schemes were tried to attain wavelength tunable operation by incorporating techniques such as turning the bandpass spectral filter [38, 41, 42], tilting the grating [29, 37, 43–45], tilting optical mirror [46], programmable controlled digital micromirror device [47], in-fiber-bandpass filter [19], adjusting slit-grating geometry [48], lyot filter [49] and liquid-crystal-on-silicon-based filter [50]. In most of the above-mentioned laser cavities, due to the inclusion of the single-mode fiber in the cavity, the maximum output average power was limited to mW level. Another consequence associated with the single-mode fiber in the laser cavity is that the pulses are heavily chirped when propagated through long dispersive fibers. This necessitates the challenging task of dechirping the pulse accordingly. Various applications demand tunable high power, specifically in the watt range across the tuning spectrum. To enhance power scaling, multiple layers of amplification stages are incorporated to increase the average output power. However, each added stage introduces additional complexities, costs, chirp, and stability challenges. Although, recently very high average power (kilowatt - kW) and peak power (gigawatt - GW) were achieved using multi-core rod type ytterbium fiber utilizing coherent combining technique [51–53]. However, these laser architectures lack tunability in central wavelength, which proves challenging to achieve in such systems. This difficulty arises because the amplification to such high-power levels is optimized only for a fixed wavelength range. The pursuit of a compact single-stage fiber laser system

with moderately high average and peak power, along with the capability to adjust the central wavelength, remains essential for various applications. Hence, we developed a tunable fiber laser system that allows central wavelength adjustments from 1010 nm to 1060 nm, maintaining an average power level above 13 W throughout the tuning range, with a maximum average power of nearly 25 W. Apart from central wavelength tunability, we can also adjust and fine-tune the spectral width (or pulse duration) of the output pulses at different central wavelengths.

Tunable Fiber OPO

In the realm of nonlinear imaging applications, the wavelength range obtained from the gain fiber proves insufficient due to its limited gain bandwidth. There arises a need to expand the wavelength region. While wavelength conversion, particularly in crystals based on $\chi^{(2)}$ nonlinearity, is a well-established technique, this section will primarily focus on the recent progress in fiber-based wavelength conversion. There are different methods to extend the wavelength region using fiber technology, for instance, soliton self-frequency shift (SSFS) [54–63], and fiber OPO [17, 64–66].

Soliton self-frequency shift (SSFS) involves red-shifting in the soliton spectrum, amplifying higher spectral components at the expense of lower ones. Achieving this shift requires negative group velocity dispersion (GVD) [67,68], making the pulses from ytterbium-doped fiber lasers unsuitable for SSFS in conventional silica-based fiber. Photonic crystal fiber with a dispersion-shifted profile near 1 µm allows for SSFS, offering a tunability range exceeding 300 nm [69]. However, there is a drawback in limited output energy due to the soliton area theorem, restricting average power to low levels. Additionally, soliton pulses exhibit femtosecond durations and a broad spectrum, restraining suitability for applications like high-resolution imaging that require a narrower bandwidth.

The utilization of fiber OPO, which relies on the four-wave mixing (FWM) process

[70, 71] in photonic crystal fiber [72], is an emerging technology with particular relevance to biomedical applications, notably coherent Raman scattering imaging techniques [16, 17, 19, 65, 73–77]. Chapter 3 provides an in-depth explanation of the fundamentals of the four-wave mixing process and fiber OPO. For efficient light conversion via FWM, the energy and momentum conservation (i.e., phase-matching condition) is crucial [78]. This process only generates those wavelengths that meet the condition of phase matching and that too with low background signal, enabling this method, a very convenient for CRS-based imaging techniques [17]. Additionally, wavelength tuning and output bandwidth can also be controlled by adjusting the pump wavelength and pump power [78, 79]. While fiber OPO stands as a mature technology, it comes with its inherent limitations. One significant drawback in conventional fiber OPO is that a long dispersive fiber within the cavity is necessary to attain the narrow bandwidth spectrum. This long dispersive fiber limits the output average power [74], and also the resulting signal/idler pulses are highly chirped, requiring external dechirping for achieving Fourier-limited pulse durations. Another limitation associated with the long dispersive fiber within the cavity is that the repetition rate of the generated signal is typically within the range of kHz [16], whereas fast imaging applications often demand a repetition rate of a few MHz [15, 73]. Therefore, there is a requirement for a fiber OPO that produces moderately high-power tunable signal/idler at a high repetition rate. To fulfill this objective, we constructed the fiber OPO solely using photonic crystal fiber, eliminating the need for single-mode dispersive fiber within the cavity. This exclusion enables the utilization of high-power pulses and facilitates high repetition rates.

Apart from SSFS and fiber OPO, there are many techniques available to extend the wavelength regions through fiber technology, for example, using dispersive wave generation [80–84], SPM-enabled spectral selection (SESS) [36, 85–88], and using supercontinuum generation [89, 90], etc., but discussing these methods could lengthen the introduction significantly.

In this work, a self-modelocked picosecond fiber laser is constructed using a rod-type

ytterbium fiber. This laser allows for adjusting both the central wavelength and the duration of pulses. The central wavelength of the generated pulses can be tuned from 1010 nm to 1060 nm, while the spectral width can be adjusted from 0.38 nm to 2.24 nm. Correspondingly, the pulse duration is tuned from 4.5 ps to 1.8 ps at 78 MHz repetition rate. The output average power obtained from this fiber oscillator is up to 25 W. Subsequently, the output of the tunable ytterbium fiber laser is propagated through a photonic crystal fiber (PCF) for the parametric generation of signal (higher frequencies than the pump) and idler (lower frequencies than the pump). The PCF has a zero-dispersion wavelength around 1040 nm. Based on the dispersion properties of the PCF and tunability of the pump source, a very broad tuning range is achieved for the signal (∼770 nm to ∼1000 nm) and idler (∼1130 nm to ∼1590 nm). This fiber OPO is singly-resonant for the signal wavelength and a maximum conversion efficiency of around 20% was achieved. In numerous applications, there is a preference for pulse durations in the femtosecond (fs) regime. However, when it comes to parametric generation, ps pulses are more advantageous. The latter choice will lead to a maximum interaction length for four-wave mixing [78]. Additionally, in comparison to fs pulses, the utilization of ps pulses will have a reduced influence on higher-order nonlinear effects in photonic crystal fiber. Although our ytterbium pump source can be utilized to operate at fs pulse duration, most of this work is entirely based on the ps pulse duration.

Outline of the thesis

This doctoral research has been conducted at the Laboratoire Ondes et Matière d'Aquitaine (LOMA), University of Bordeaux, in partnership with the European Union's H2020 Research Framework Programme (ITN-GREAT). The acronym 'GREAT' stands for '**G**rating **R**eflectors **E**nabled laser **A**pplications and **T**raining. The project 'GREAT', in summary, is about the manufacturing, and application of grating waveguide structures (GWS) for high-power laser applications. In this project, my primary responsibilities included in-

corporating these GWS into our laser configurations to achieve wavelength adjustment, spectral filtering, and compression of the laser pulses. The initial part of my research was dedicated to developing a high-power picosecond/femtosecond tunable fiber oscillator. Subsequently, in the next phase, this high-power fiber laser was used as a pump source to build a tunable fiber optical parametric oscillator.

The first chapter covers fundamental laser principles, introducing concepts such as absorption, spontaneous, and stimulated emission. It also provides a concise overview of population inversion, along with discussions on three-level and four-level laser systems. Moreover, the foundational understanding of fibers and fiber lasers are presented, particularly emphasizing the utilization of ytterbium-doped gain medium for laser operation.

The next chapter directs its attention towards laying the groundwork for generating pulsed output by employing mode-locking techniques, encompassing both active and passive techniques. Following this, the subsequent part of this chapter focuses on the behavior of pulsed signals as they propagate through optical fiber, with a primary focus on examining dispersion and the nonlinear effects. Concluding this chapter explores different regimes for shaping pulses within laser setups.

The third chapter relies on the theoretical background regarding four-wave mixing in optical fiber. The introductory concepts based on the coupled amplitude equation and the phase-matching conditions are discussed. Finally, a brief introduction to fiber optical parametric oscillator (FOPO) is presented.

The fourth chapter reports on the development of an all-normal-dispersion (ANDi) fiber laser. It elaborates on the setup used for experimentation, discusses the results of the experiments, and finally concludes by highlighting the central emphasis on presenting numerical simulations. These simulations were carried out to interpret the experimental findings and enhance the understanding of the subject matter.

In the fifth chapter, the configurations of a fiber optical parametric oscillator (FOPO)

using photonic crystal fiber are presented. A concise numerical simulation addressing four-wave-mixing within the optical fiber is included. This chapter is concluded by presenting the results of the fiber OPO.

Lastly, a discussion and a conclusion are presented with a main focus on the future prospects and the application of these fiber oscillators in nonlinear imaging and supercontinuum generation. Furthermore, potential improvements for both ANDi laser and fiber OPO are discussed.

Chapter 1

Lasers and Fiber laser basics

Contents

This chapter introduces the basics of lasers and fiber lasers, emphasizing ytterbium doped gain medium for laser operation.

1.1 Introduction to lasers

The schematic of a simple laser cavity is shown in Fig. 1.1, and it is comprised of three important parts [91]:

- The gain or amplifying medium, whose atoms, or molecules are excited by the pump for the purpose of stimulated emission.
- Pumping system to excite the gain medium
- The oscillator cavity consists of two mirrors to amplify the stimulated emission by propagating back and forth through the gain medium

The output beam from such a well-designed laser cavity is often monochromatic and coherent in nature [92].

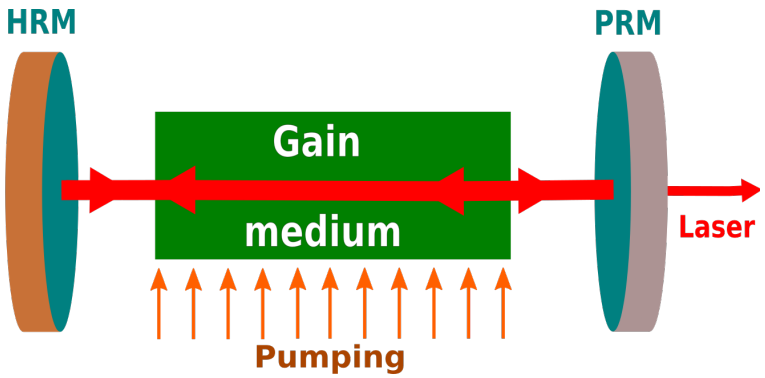

Figure 1.1: Schematic of laser oscillator. The gain medium is excited by the pump laser and the stimulated emission initiated by the spontaneous emission is amplified by making a cavity consisting of a high-reflecting mirror (HRM) and a partially-reflecting mirror (PRM).

1.1.1 Absorption, spontaneous and stimulated emission

There are three basic concepts to understand the working principle related to laser phenomenon as shown in Fig. 1.2:

- **Absorption:** The atoms transition to the higher energy level (E_2) from the ground energy level (E_1) is governed by absorbing the pump energy
- **Spontaneous emission:** The excited atoms in the higher energy level decay to the lower energy level spontaneously and emit a photon of energy hν in a random fashion.
- **Stimulated emission:** The difference between the spontaneous and stimulated emission is that in the latter an incoming photon of energy hν gives rise to the transition of the excited atom from the higher-energy state to lower energy state, hence resulting in the creation of another photon with identical direction, frequency, and phase. The first concept of stimulated emission dates back to 1917 [93], but it found practical application in the 1950s and beyond, first with Masers [94, 95], and later with lasers [96].

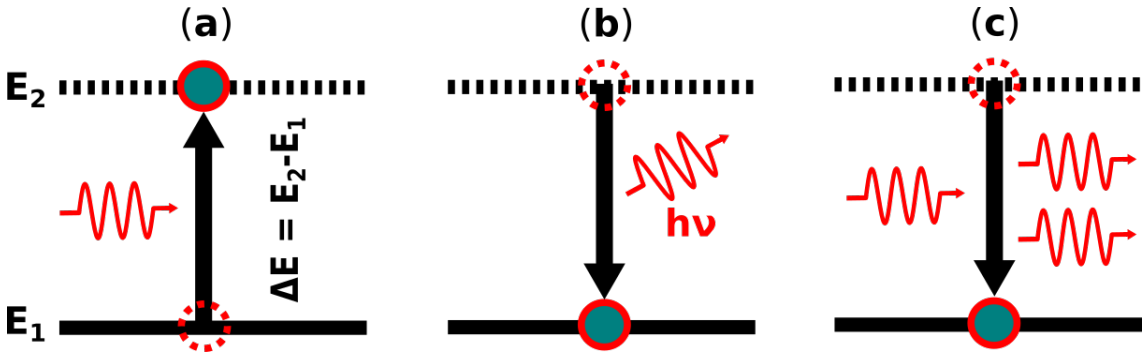

Figure 1.2: Pictorial explanation of two levels (a) absorption, (b) spontaneous emission, and (c) stimulated emission.

1.1.2 Population inversion

Population inversion is an essential concept in laser physics. It corresponds to a situation where the number of atoms or molecules in an excited state (N_2) surpasses that of a lower excited state (N_1) in a laser medium. This situation is necessary for the amplification of light by stimulated emission. In order to achieve population inversion, the gain medium

is pumped, which excites the atoms or molecules and moves them to higher energy levels. According to the Boltzmann distribution law, the number of atoms in an excited state is given by

$$N_2 = N_1 \exp\left(-\frac{E_2 - E_1}{kT}\right), \tag{1.1}$$

where k is Boltzmann constant, and T is the temperature. From this equation, population inversion will occur when $\frac{N_2}{N_1} > 1$ [92]. It is not very feasible (almost impossible) to attain population inversion in a two-level system because pumping atoms into the excited state has an equal chance of stimulating them back down (besides spontaneous emission), so generally the population of the ground state is always larger than the excited state population ($N_1 > N_2$). This makes it generally impossible to achieve population inversion.

1.1.3 Three and four-level laser mechanisms

The three and four-level operations of the laser are shown in Fig. 1.3a and Fig. 1.3b, respectively. The working principle of both mechanisms is that the atoms are excited from the ground energy state (E_1) to the higher energy state (E_2) by pumping. After that, there is a fast transition (non-radiative) to a lower energy level (E_3). The stimulated emission in the presence of an incoming photon occurs when there is a transition from energy state 3 to 1 in a three-level operation, while in the case of a four-level laser operation, the transition is from state 3 to 4, respectively. In both scenarios, energy level 3 should be densely populated to achieve population inversion. In a three-level system, the transition from energy states 2 to 3 is relatively fast (lifetime typically in the range of nanoseconds), while the transition from level 3 to 1 is slow. As the starting pump level and stimulated emission end level are the same, there is a requirement for strong pumping in order to achieve population inversion. In a four-level laser operation the transitions from energy states 2 to 3, and 4 to 1 are faster than the transition from level 3 to 4, ideally $N_4 \approx 0$, this

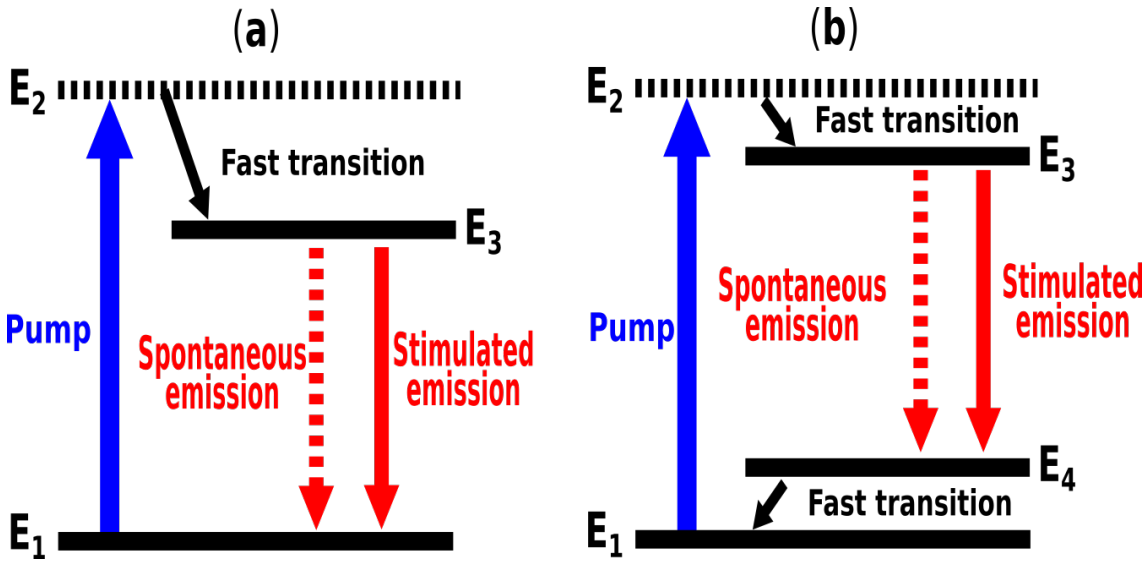

Figure 1.3: Laser operation (a) three-level and (b) four-level. E_1, E_2, E_3, and E_4 are the corresponding energies of level 1 (ground state), level 2, level 3, and level 4, respectively, such that $E_1 < E_4 < E_3 < E_2$.

makes achieving population inversion easy ($N_3 > N_4$) compare to the three-level system.

1.2 Ytterbium-doped laser gain medium

One of the important rare-earth doped elements in the scope of lasers is ytterbium. The energy levels of ytterbium are plotted in Fig. 1.4 [32]. The main energy levels contributing to light amplification are ground energy level ($^2F_{7/2}$) and excited energy level ($^2F_{5/2}$). Both of these energy levels have sub-energy levels (manifold) while absorption and emission are achievable in different sub-energy levels as shown in Fig. 1.4. Even though the transitions occur only between two energy levels, ytterbium behaves like a quasi-three-level system because of the presence of sub-energy levels. Due to this, ytterbium-doped gain media usually need high pump energy.

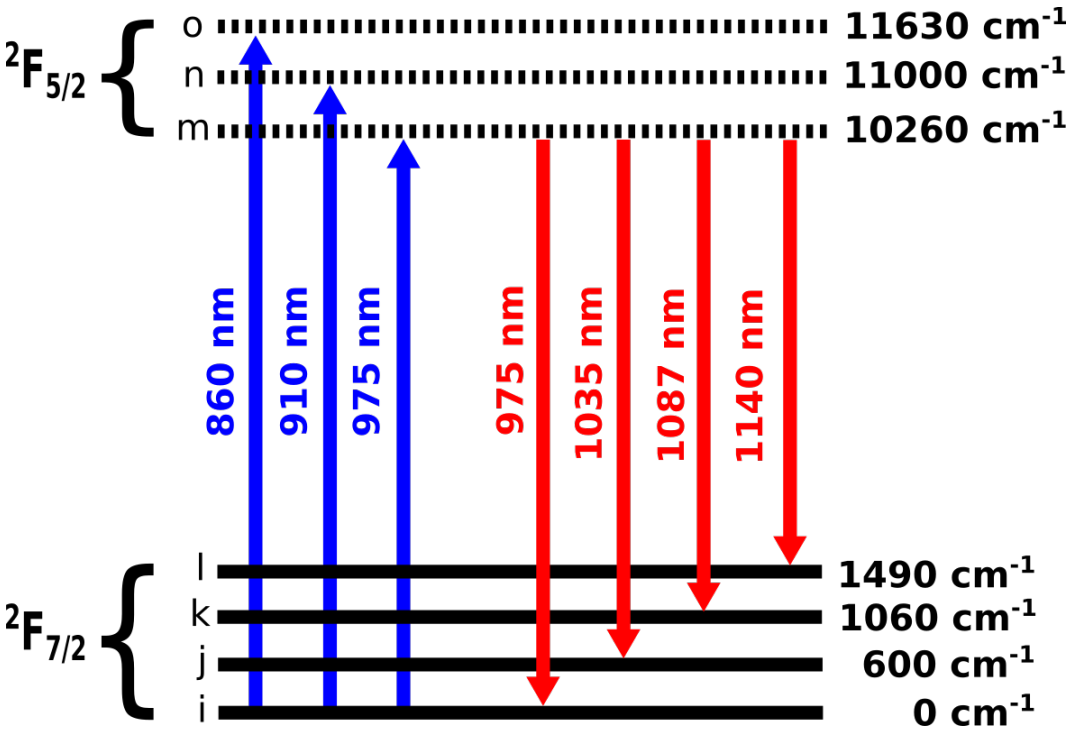

Figure 1.4: Ground and excited energy levels (manifold) of Yb^{3+}. The wavenumber and the transitions related manifold in ground level and excited level are shown [32].

1.2.1 Absorption and emission cross-sections

The cross-section (absorption and emission) is the necessary terminology in laser amplifiers. Having the knowledge of cross-sections of the rare-earth doped gain media, it is possible to predict the spectral regions where the absorption and emission are optimal [97]. For instance, the ideal laser medium needs to absorb pump wavelengths but not others, and emit only at the lasing wavelength, not others. Besides other parameters, the absorption and emission cross-sections are also affected by the host material [98, 99].

The absorption and emission cross-section of Yb^{3+} in germanosilicate glass [33] (shown in Fig. 1.5) can be well-approximated using the McCumber relation [100],

$$\sigma_{emi}(\nu) = \sigma_{abs}(\nu) \exp\left(\frac{E_{ex} - h\nu}{kT}\right), \tag{1.2}$$

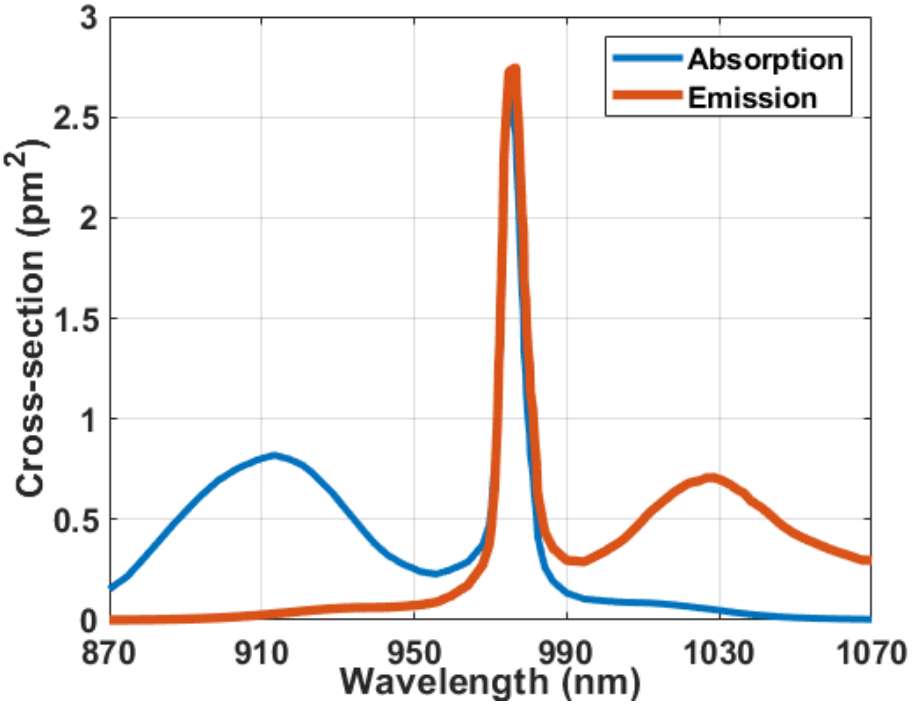

Figure 1.5: Emission and absorption cross-section of Yb in germanosilicate glass. Recreated from [33].

where $\sigma_{emi}(\nu)$ and $\sigma_{abs}(\nu)$ are the emission and absorption cross-section, while E_{ex} is the excitation energy. E_{ex} can be calculated at room temperature using the following relation [101],

$$\exp\left(\frac{E_{ex}}{kT}\right) = \exp\left(\frac{E_{mi}}{kT}\right)\left[\frac{1+\exp\left(\frac{E_{ji}}{kT}\right)+\exp\left(\frac{E_{ki}}{kT}\right)+\exp\left(\frac{E_{li}}{kT}\right)}{1+\exp\left(\frac{E_{nm}}{kT}\right)+\exp\left(\frac{E_{om}}{kT}\right)}\right], \tag{1.3}$$

where $E_{ji} = E_j - E_i$ is the energy difference of 'i^{th}' and 'j^{th}' sub-energy levels, and so on. 'E_{mi}' is the zero-line energy, and it is the difference in energy between the lowest sub-energy level of the excited manifold (m^{th}) and the lowest sub-energy level of the ground manifold (i^{th}), and this corresponds to a 975 nm transition. The values of the energy difference in Eq. 1.3 are calculated using the wavenumber values of ytterbium sub-energy levels in Fig. 1.4. From Fig. 1.5, it is evident that the pump energy can be provided at 910 nm and 975 nm, and the optimal lasing wavelength can be achieved around 1030 nm. Although other rare-earth-doped gain media have their own advantages, the ytterbium-doped gain

medium has several advantages over its counterparts. Due to the low energy difference between the ground and excited state manifolds, the quantum defect (difference between absorbed and emitted photon energies) given in Eq. 1.4 is very low compared to other laser gain media. This also results in high power efficiency, reduced thermal effects, and less excited state absorption [33]. Actually,

$$QD = E_{abs} - E_{emi} = h\nu_{abs} - h\nu_{emi} = h\nu_{abs}\left[1 - \frac{\lambda_{abs}}{\lambda_{emi}}\right] \tag{1.4}$$

So, in the case of the ytterbium-doped gain medium, the emission wavelength is 1030 nm, while the absorption wavelength is around 975 nm, resulting in a QD of $\sim$ 5.34 %, while this value is $\sim$ 36.8 % for erbium-doped gain medium (λ_{emi}: 1550 nm, λ_{abs}: 980 nm).

1.3 Introduction to optical fiber and fiber lasers

The fundamental usage of the fiber is to guide light [102, 103] over a long distance with minimal losses [104,105]. The light is guided through the core (high-index) which is cladded on top to fulfill the principle of total internal reflection and to prevent the light from exiting the core (the cladding has a lower index compared to the core). The main components in an optical fiber are shown in Fig. 1.6.

1.3.1 Photonic crystal fiber

Generally in traditional fiber, the cladding is made of pure silica, while the core is doped glass that has a higher refractive index than the cladding and the light is guided through the core due to index difference. Photonic crystal fibers (PCFs) are fibers that possess a micro-devised cross-section composed of fused silica and air holes that are arranged in a periodic manner along the fiber's propagation axis (Fig. 1.7). PCF is composed of a solid

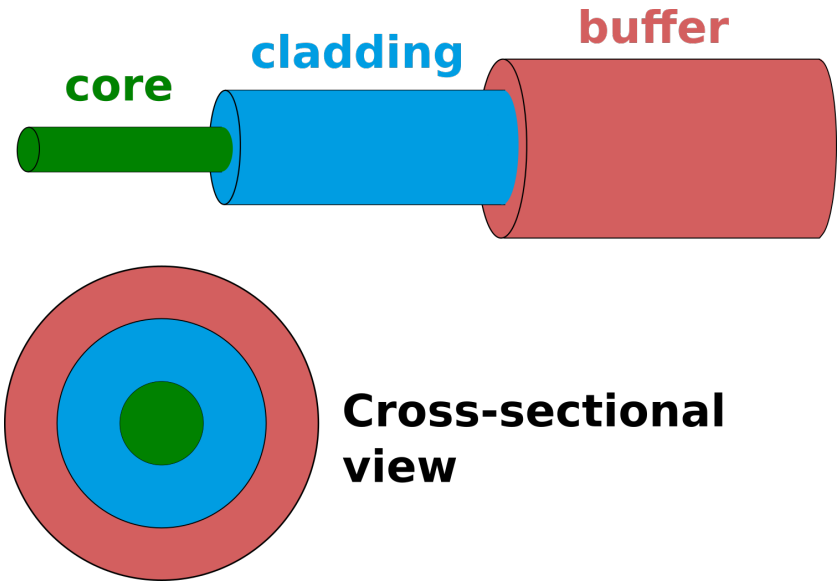

Figure 1.6: Schematic and cross-sectional view of the conventional fiber having a high-index core, a low-index cladding, and protection on top of the cladding.

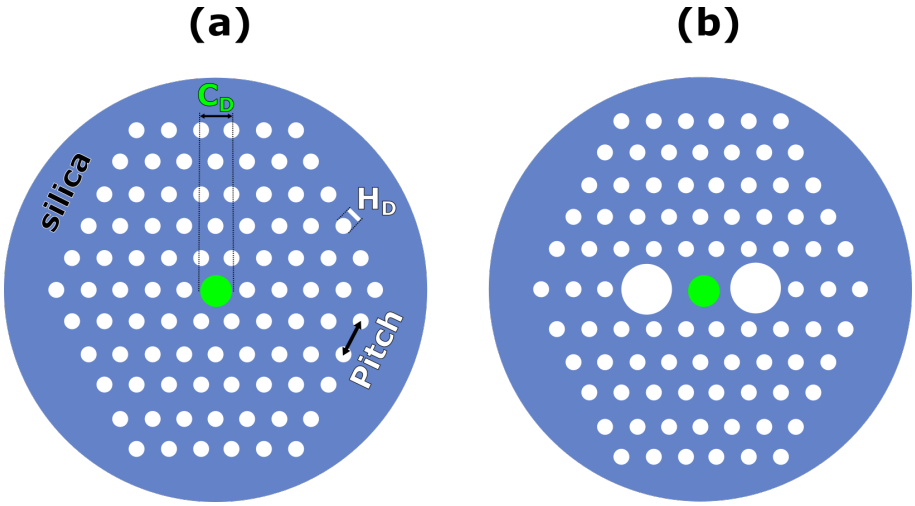

Figure 1.7: (a) Cross-section of the Photonic crystal fiber with an active solid core having a diameter (C_D), arrays of holes with the diameter (H_D) arranged in a hexagonal pattern with the given hole-to-hole distance (Pitch) (b) Cross-section of the polarization maintaining photonic crystal fiber with the same characteristics but with two additional stress-providing larger holes on one of the principle propagation axis to provide the necessary birefringence.

or hollow core, with air holes arranged in various patterns around it, and the arrangement of air holes governs the propagation of light inside the PCF [106, 107]. The basic working

principle of the solid core PCF is similar to the conventional fiber and the refractive index difference between the core and the micro-engineered-cladding is positive [108, 109], while the hollow-core PCF works on the principle of photonic bandgap propagation because the index difference is negative [110]. In addition to other features, one of the key benefits of PCFs is the ability to customize the zero dispersion wavelength (ZDW), and employing such PCFs for parametric generation enables the investigation of those wavelength regions that are not readily accessible with conventional gain-based materials. This is possible because the zero-dispersion wavelength can be shifted according to the required applications in micro-structured fibers [111–113] to a longer or shorter wavelength than the ZDW of single-mode fiber made of fused silica. Figure 1.8 shows the β_2 (Group velocity dispersion, GVD)

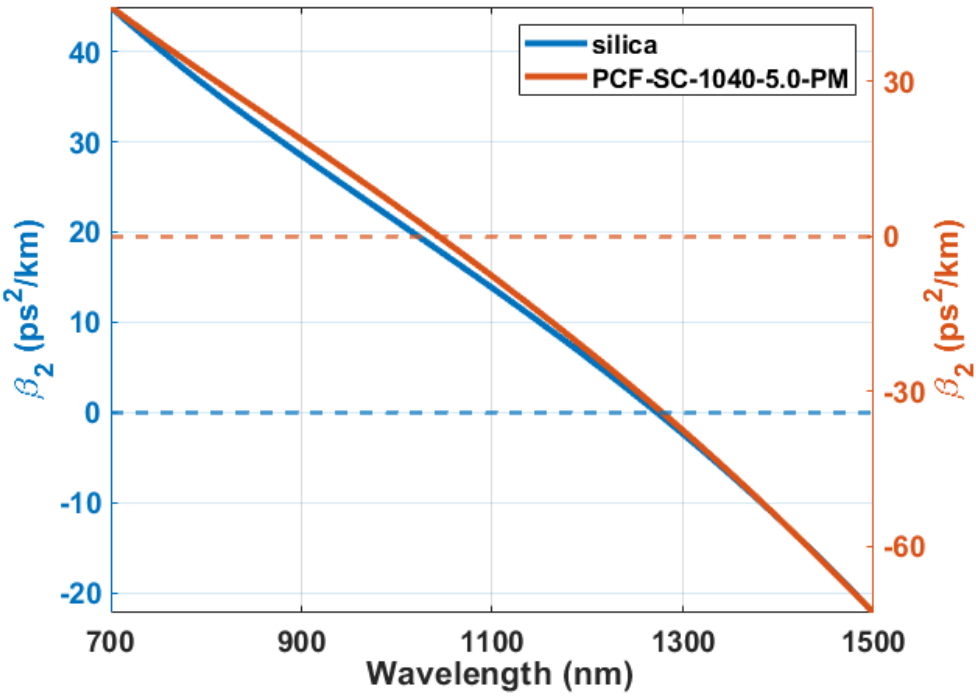

Figure 1.8: β_2 of silica (**cyan**) and the photonic crystal fiber (**orange**). β_2 of the conventional fused silica fiber is calculated using the dispersion of the fused silica, and the latter is computed using $D = -\frac{\lambda}{c}\frac{d^2n}{d\lambda^2}$ while the refractive index (n) is estimated using the Sellmeier equation. The β_2 of the PCF (used in our experiments), is calculated from the dispersion profile provided by NKT-photonics. The zero-dispersion wavelength ($\beta_2 = 0$) is shifted for the PCF fiber to ~ 1040 nm.

plotted against the wavelength for the standard fused-silica fiber and the PCF-SC-1040-5.0-PM (NKT-Photonics). The β_2 is calculated using the dispersion profile of both fibers. The ZDW of the former lies around $\sim 1.27\,\mu m$ while the ZDW of the PCF is shifted to $\sim 1040\,nm$.

1.3.2 Fiber lasers

The classification of laser is typically based on the gain media (solid, liquid, or gas) used for the amplification of light. Gain media in the form of gas [114] are, for instance, but not limited to, CO_2, He-Ne, and excimer lasers (KrF, ArF), etc. Likewise, dye laser comprises liquid gain media [115] such as rhodamine 6G in a solution, etc. All other lasers come in the domain of solid-state lasers, although semiconductor lasers [116,117] that are based on solid gain media, are categorized distinctly. Fiber lasers fall within the scope of semiconductor lasers, where the host material is doped with rare-earth ions. Ytterbium, erbium, neodymium, bismuth, praseodymium, dysprosium, thulium, and holmium are some of the known dopants employed to investigate different spectral regions. The emission spectral regions of the fiber lasers range from ultraviolet (UV) up to mid-infrared (MIR) [32,118–123]. The benefits of fiber lasers are compactness (hundreds of meters of fiber can be coiled), robustness (little or no free space optics), good beam profile (beam shape is confined by the fiber parameters), low maintenance requirements (easy alignment, less thermal issues, high damage threshold), and cost-effective (readily available components). Besides other advantages, rare-earth doped fibers have a broad gain bandwidth which is quite helpful for generating tunable and ultrashort pulsed output. Similarly, fiber lasers have a lower threshold power level thanks to their high gain efficiency, and the latter facilitates attaining high output power.

Chapter 2

Introduction to Mode locking and pulse propagation in optical fiber

Contents

The chapter familiarizes with the concepts of mode locking, with a particular focus on the pulse propagation of the ultrashort pulse inside a fiber.

2.1 Theory of Mode-locking

Mode-locking is a technique to generate short-duration pulses usually with a duration of picosecond (10^{-12} s) or lower [1]. The concept of mode-locking is to have a controlled phase relation among the longitudinal modes oscillating in the laser oscillator [124] in such a way that they constructively interfere at a specific time resulting in intense pulsed output. The frequencies of the allowed longitudinal modes oscillating in a linear cavity are determined by,

$$\nu_m = \frac{mc}{2nL} \tag{2.1}$$

where ν_m is the frequency at m^{th} mode, c is the speed of light, n is the refractive index, and L is the length of the cavity. The frequency separation between the subsequent modes is $\delta\nu = \nu_m - \nu_{m-1} = c/2nL$, which is also called the laser repetition rate f_{rep}. Fig. 2.1 shows the laser gain bandwidth and the corresponding modes oscillating in the cavity. Typically, these longitudinal modes have random phases resulting in uneven output amplitude.

However, in mode-locking, a constant phase relation is set between these modes, enabling them to constructively interfere with each other and produce extremely short optical pulses with the highest possible amplitude Fig. (2.2). The larger the number of modes locked, the shorter the duration, because the bandwidth in the spectral domain has an inverse relation to duration in time. Figure 2.2 shows the superposition of 12 modes, for both the locked phases and random phases among the modes.

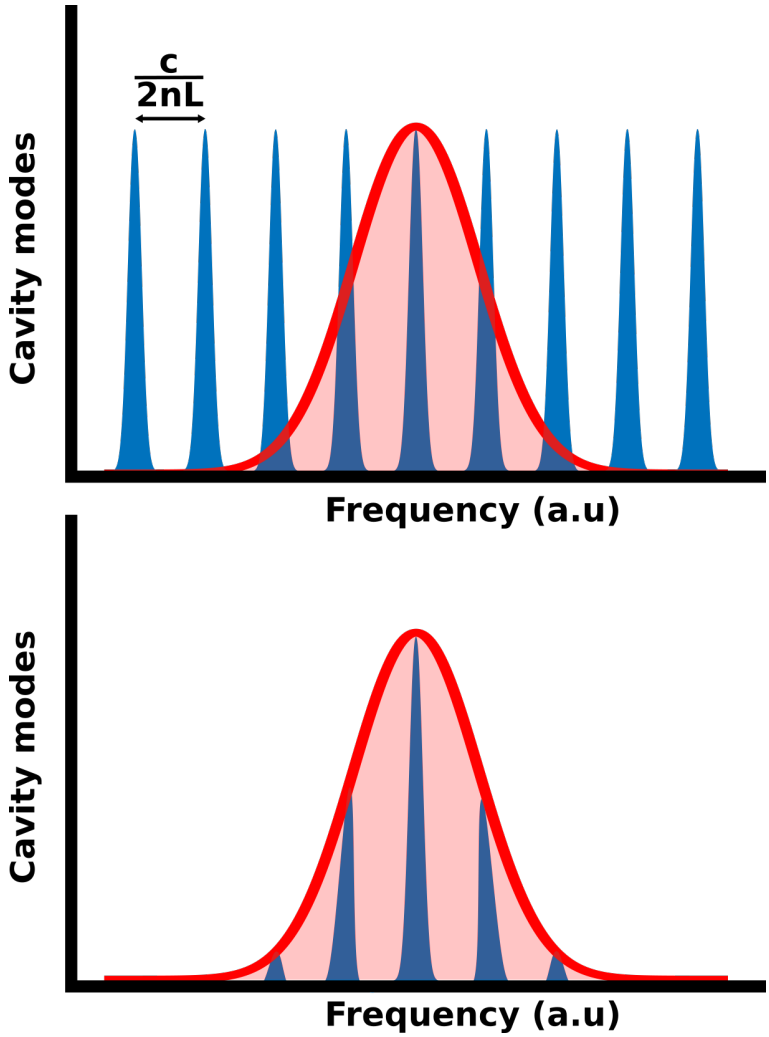

Figure 2.1: Oscillating modes in the laser cavity (blue), laser gain bandwidth (red). The bottom figure shows the pictorial explanation of the modes that fit within the laser gain bandwidth.

2.1.1 Active mode-locking

This method of achieving mode-locking shown in Fig. 2.3, involves an externally driven modulator (either amplitude modulator or phase modulator) [1, 125–127]. The amplitude modulator alters the losses periodically, and when the modulation coincides with the oscillator round-trip time, it leads to the generation of short optical pulses [128]. There are different modulators used for this purpose, such as an electro-optic modulator, an

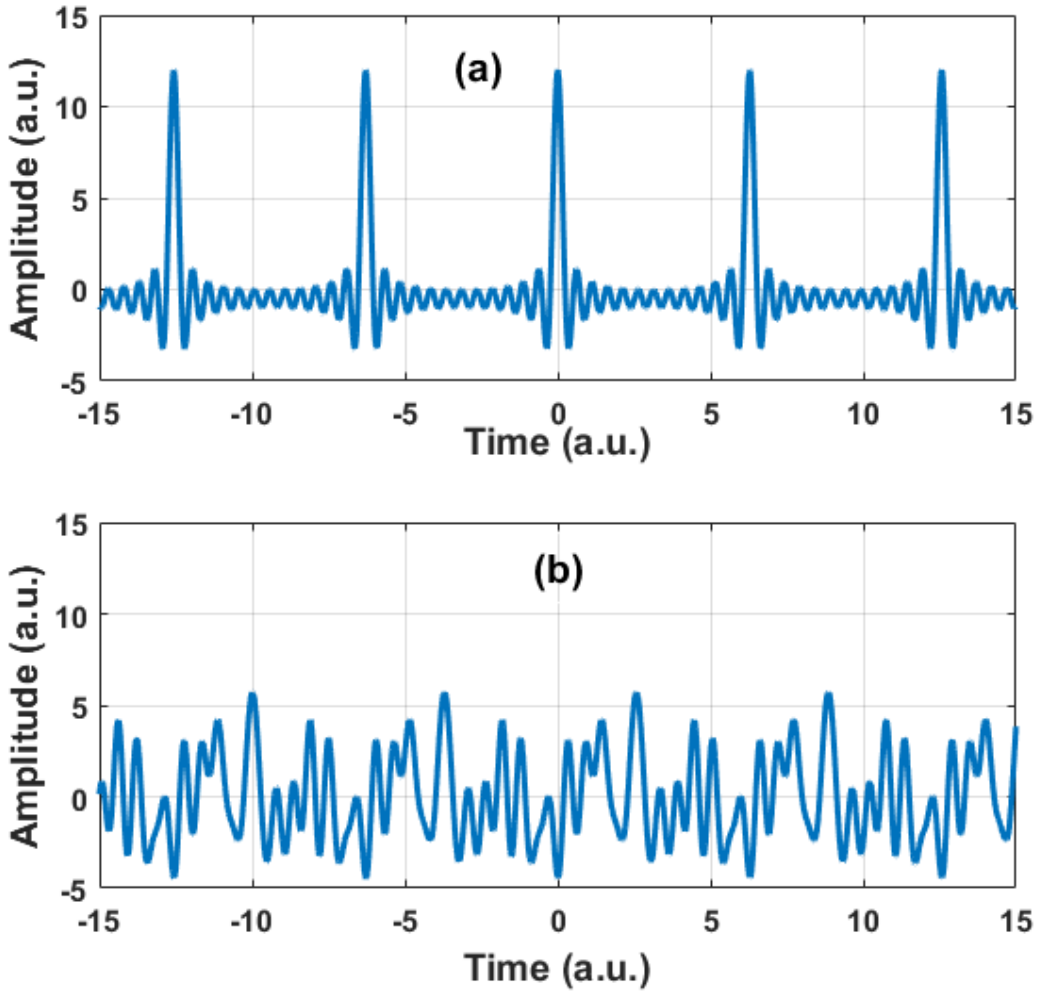

Figure 2.2: (a) Superposition of the 12 modes with no phase offset between them resulting in high amplitude and distinct pulses. (b) Superposition of the same modes with random phase offset between them.

acousto-optic modulator, and a Mach–Zehnder integrated-optic modulator, etc.

2.1.2 Passive mode-locking

Contrary to active mode-locking, passive mode-locking is a technique in which the modulator is not controlled externally, but the modulator (or mechanism) itself provides the required modulation of the losses [129–139]. A passive component, for instance, a sat-

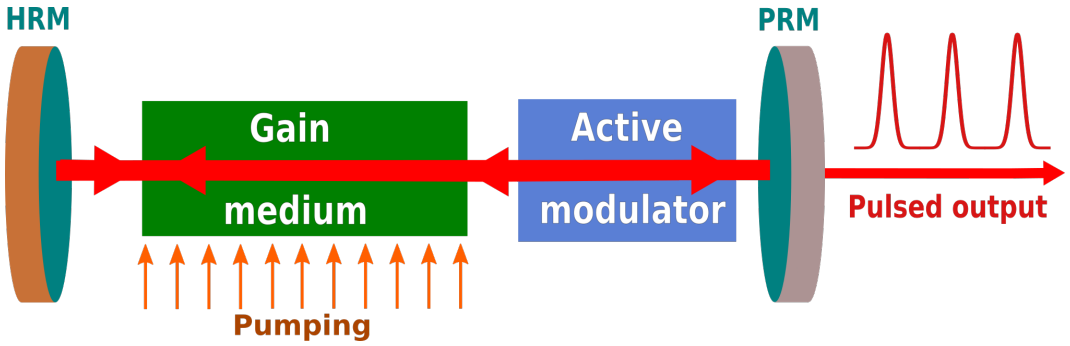

Figure 2.3: Schematic of active mode-locking. Linear laser oscillator in which an active modulator is placed inside the laser cavity, the transmission of the modulator being controlled externally.

urable absorber whose transmissivity (or reflectivity) is intensity dependent is used in the laser cavity. When the pulse propagates through it, the low-intensity part of the pulse suffers greater losses, while the high-intensity part of the pulse saturates the absorber, and transmits (or reflects) through it. This is how short pulse operation is achieved by the use of saturable absorption. Passive mode-locking is classified into two categories: (1) Mode-locking in which a real saturable absorber is used such as semiconductor saturable absorber mirror (SESAM) [140], quantum dot (based on lead-sulfide) [141], carbon nanotubes (CNTs) [142–144], and saturable absorber based on fibers [145], etc.;(2) Artificial saturable absorber in which a mechanism mimicking the working principle of real saturable absorption is developed like in Kerr-lens mode-locking [146], additive pulse mode-locking [147], nonlinear-optical-loop-mirror (NOLM) [148, 149], nonlinear-amplifying-loop-mirror (NALM) [150, 151], and nonlinear polarization rotation (NPR) mode-locking [152]. This latter technique will be discussed in detail as this method is used to mode-locked pulses in our experimental setup.

2.1.2.1 Nonlinear polarization rotation in fiber

The nonlinear polarization rotation in a non-polarizing maintaining fiber has been used widely for the generation of ultrashort pulses [153–158]. This method does not require

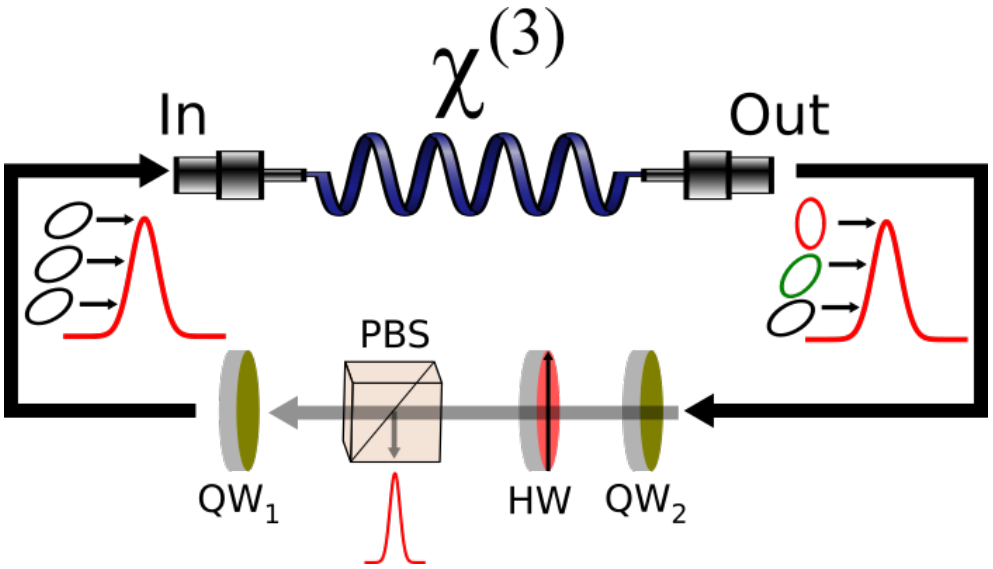

Figure 2.4: Illustration of non-linear polarization rotation inside the optical fiber along with the combination of the wave-plates and output port (PBS).

the real saturable absorber component (e.g. SESAM etc.) inside the laser cavity for the mode-locking. The basic principle of NPR is shown in Fig. 2.4. Using the Jones matrix it can be shown that the polarization rotation $\Delta\Phi$ in a fiber ($\chi^{(3)}$ medium) of length 'L' is given by,

$$\Delta\Phi = \frac{\gamma L}{3}\left[|E_x|^2 - |E_y|^2\right], \tag{2.2}$$

where E_x, and E_y are the polarized components of the light along x- and y-axes, respectively. The nonlinear coefficient γ in the above equation writes:

$$\gamma(\omega_0) = \frac{n_2\omega_0}{cA_{eff}}. \tag{2.3}$$

Here c is the speed of light, n_2 is the nonlinear index and A_{eff} is the effective area of the fiber. The intensity after passing through quarter-waveplates (QW_1, QW_2), half-waveplate

(HW), and a polarizer is given by [159]:

$$I_{NLP} = \frac{1}{2}\left[1 - \sin(2\theta_{QW1})\sin(2\theta_{QW2})\right] + \frac{1}{2}\cos(2\theta_{QW1})\cos(2\theta_{QW2})\cos(2(\theta_{QW1} + \theta_{QW2} - 2\theta_{HW} + \Delta\Phi)) \tag{2.4}$$

where θ_{QW1}, θ_{QW2}, and θ_{HW} are the angles between the principle axis of QW_1, QW_2 and HW and the polarizer axis, respectively. Eq. 2.4 shows that, for a given fiber length (L) and input polarization light, the rotation depends on the intensity of the light. This means that, within a pulse, the high-intensity part will induce more phase shift than the low-intensity part. The rotation of the high-intensity part is different than that of the low-intensity part of the pulse (Fig. 2.4). Secondly, the intensity at the output is sinusoidal in nature, i.e. depends on the cosine of angles.

As shown in Fig. 2.4, a polarizing beam splitter (PBS) cube separates the light into two orthogonal linear polarization states. A quarter wave plate (QW1), after the PBS cube, is used to transform the linear polarization into an elliptical polarization (the low and high-intensity regions have identical rotations). As the pulse traverses through the fiber, the axes of the polarization ellipse rotate due to Kerr nonlinearity as discussed above. The rotation at the central part of the pulse is more than that of its low-intensity part. The quarter-waveplate (QW2) is adjusted in a way to make the polarization linear in only the central part of the pulse. The combination of the half-waveplate and PBS cube only allows the intense part (with linear polarization) while the low-intensity part of the pulse is blocked, hence generating a short pulse at the output. The PBS cube acts both as a polarizer and output coupler in this case. Contrary to a real saturable absorber which is vulnerable to high energy and the output power is limited, the NPR-based mode-locking is much more resistant to high power.

2.2 Pulse propagation in optical fiber

Maxwell's equations are the governing principles that explain the propagation of optical fields in fibers, and these equations are

$$\nabla \times \mathbf{E} = -\frac{\partial \mathbf{B}}{\partial t} \tag{2.5}$$

$$\nabla \times \mathbf{H} = \frac{\partial \mathbf{D}}{\partial t} \tag{2.6}$$

$$\nabla \cdot \mathbf{D} = 0 \tag{2.7}$$

$$\nabla \cdot \mathbf{B} = 0 \tag{2.8}$$

where **E** and **H** are the electric and magnetic fields, while **D** and **B** are the electric and magnetic flux densities. The above equations are written for no free carrier charges otherwise the current density **J** and the charge density ρ are included.

For a pulse, of central frequency ω_0 propagating in optical fiber along the z-axis, the electric field, in the frequency domain obeys the following equation [78]:

$$\nabla^2 \vec{E} + \beta^2(\omega)\vec{E} = \mu_0 \omega^2 \vec{P}_{NL}, \tag{2.9}$$

where $\beta(\omega) = n(\omega)\frac{\omega}{c}$ is the wavenumber, and $\vec{E} = \vec{E}(\vec{r}, \omega - \omega_0)$. $\vec{P}_{NL}(\vec{r}, \omega - \omega_0)$ is nonlinear polarization within the fiber. Using the method of separation of variables, $\vec{E}$ for a linearly polarized field along the propagation axis writes:

$$\vec{E}(\vec{r}, \omega - \omega_0) = \hat{x}F(x, y)A(z, \omega - \omega_0)\exp(i\beta_0 z), \tag{2.10}$$

where $\beta_0 = \beta(\omega_0)$ and $A(z, \omega)$ is a slowly varying function of z (i.e., $\frac{\partial \mathbf{A}^2}{\partial z^2} = 0$), while $F(x, y)$ is the modal distribution in the core region. Moreover, $\beta(\omega)$ can be expanded using Taylor

series approximation around central angular frequency ω_0,

$$\beta(\omega) = \beta_0 + \beta_1(\omega - \omega_0) + \frac{\beta_2(\omega - \omega_0)^2}{2!} + \frac{\beta_3(\omega - \omega_0)^3}{3!} + ..., \tag{2.11}$$

where

$$\beta_j = \left(\frac{d^j \beta}{d\omega^j}\right)_{\omega=\omega_0} \qquad j = 1, 2, 3, ...$$

The higher order terms of $\beta(\omega)$ i.e. $(\beta_3, \beta_4, ...)$ are not significant when dealing with long pulses (durations $\geq$1 ps) while working far from zero-dispersion wavelength, so they can be neglected. Taking into account the impact of both fiber attenuation (α) and nonlinearity, one obtains the following equation for $A(z,t)$ in the time domain [78]:

$$\frac{\partial A}{\partial z} + \beta_1 \frac{\partial A}{\partial t} + i\beta_2 \frac{\partial^2 A}{\partial t^2} + \frac{\alpha}{2} A = i\gamma(\omega_0)|A|^2 A, \tag{2.12}$$

Eq. 2.12 is called the nonlinear Schrödinger equation (NLSE). The term $\beta_1 = \frac{1}{v_g}$ is related to the group velocity v_g which is frequency-dependent, which means that the different spectral components travel at different speeds while propagating in the optical fiber. The variable β_2 is the dispersion of the group velocity $\left[\beta_2 = \frac{d}{d\omega}\left(\frac{1}{v_g}\right)\right]$ and is referred to as the group velocity dispersion (GVD) parameter which accounts for the broadening of the pulse. β_1 and β_2 are related to dispersion parameter D by [78],

$$D = \frac{d\beta_1}{d\lambda} = -\frac{2\pi c}{\lambda^2}\beta_2. \tag{2.13}$$

In the above equation (Eq. 2.12), the propagation of the pulse within a passive fiber is considered. If we extend the NLSE to encompass the propagation through a doped fiber, we must take into account the impact of the gain medium (bandwidth and saturation). Equation 2.12 accounts for the losses, dispersion, and nonlinear effect, which are briefly explained in the following sections.

2.2.1 Absorption effects

The measurement of power attenuation is an important characteristic of an optical fiber and it is one of the factors which limits long-haul propagation unless handled. The output power of the fiber is expressed as,

$$P_{out}(z) = P_{in} \exp(-\alpha z), \tag{2.14}$$

where P_{out} and P_{in} are the output and input power, respectively, while α is the attenuation constant, which quantifies the fiber losses. The losses in optical fiber are the result of various factors [160], which include, but are not limited to, scattering losses, absorption, and losses due to fiber components (connectors, splice, etc.). For efficient and long propagation, all of these losses should be minimized.

2.2.2 Dispersion effects

In order to understand the dispersion effects alone, Eq. 2.12 is simplified to have only the effect of the GVD parameter while ignoring the losses and nonlinear effects. Taking its Fourier-transform [78], it becomes:

$$i\frac{\partial A}{\partial z} = -\frac{1}{2}\beta_2\omega^2 A \tag{2.15}$$

The analytical solution to this equation is,

$$A(z,\omega) = A(0,\omega)\exp\left[\frac{i}{2}\beta_2\omega^2 z\right], \tag{2.16}$$

where $A(0,\omega)$ is the field at the fiber input. The above equation indicates that, as the pulse travels along the fiber, the GVD causes a shift in the phase of each spectral component ω based on the distance z it has traveled, and due to that pulse shape alters and broadens.

For example, let us take a simple Gaussian-shaped pulse at the input of the fiber which is written as,

$$A(0,t) = A_0 \exp\left(-\frac{t^2}{2\Delta\tau^2}\right), \tag{2.17}$$

where $\Delta\tau$ is related to full-width at half maximum of the pulse. By taking the Fourier transform to get $A(0,\omega)$ and plugging it into Eq. 2.16 and then taking the inverse Fourier transform, one gets:

$$A(z,t) = A_0 \frac{\Delta\tau}{\sqrt{\Delta\tau^2 - i\beta_2 z}} \exp\left[-\frac{t^2}{2\Delta\tau^2 - 2i\beta_2 z}\right] \tag{2.18}$$

Separating the modulus and argument of the complex number in Eq. 2.18 leads to:

$$A(z,t) = \frac{A_0\Delta\tau}{\sqrt{\Delta\tau^4 + \beta_2^2 z^2}} \exp\left[-\frac{t^2\Delta\tau^2}{2\left(\Delta\tau^4 + \beta_2^2 z^2\right)}\right] \exp\left(-i\phi_{DI}(z,t)\right). \tag{2.19}$$

The broadening of the width of the pulse ($\Delta\tau_B$) can be seen in the above equation and it is given by,

$$\Delta\tau_B(z) = \sqrt{\left(\frac{\Delta\tau^4 + \beta_2^2 z^2}{\Delta\tau^2}\right)}, \tag{2.20}$$

while the phase change due to dispersion ϕ_{DI} is,

$$\phi_{DI}(z,t) = \frac{-t^2\beta_2 z}{\Delta\tau^4 + \beta_2^2 z^2} + \frac{1}{2}\arctan\left(\frac{\beta_2 z}{\Delta\tau^2}\right). \tag{2.21}$$

So, for clarity, Eq. 2.19 can be expressed as,

$$A(z,t) = A_D(z) \exp\left[-\frac{t^2}{2\Delta\tau_B^2}\right] \exp\left(-i\phi_{DI}(z,t)\right), \tag{2.22}$$

where $A_D(z)$ is the change in the amplitude and its expression (in front of the exponential factors) is given in Eq. 2.19. From this equation, it is clear that after propagating in the

fiber, the pulse shape is still Gaussian while its amplitude and phase change. The equation governing the broadening of the pulse (Eq. 2.20) can be simplified using the normalized factor z/L_D:

$$\Delta\tau_B = \Delta\tau\sqrt{\left(1+\frac{z^2}{L_D^2}\right)}, \tag{2.23}$$

where L_D is termed as the dispersion length ($L_D = \frac{\Delta\tau^2}{|\beta_2|}$). For a fixed propagation distance and GVD parameter β_2, the broadening of the pulse is dependent on the initial pulse duration, for instance, the pulse having a shorter duration will undergo more broadening and vice versa. Figure 2.5 shows the broadening of the unchirped pulse while propagating inside the fiber. The chirp (instantaneous change in frequency), can be expressed by taking

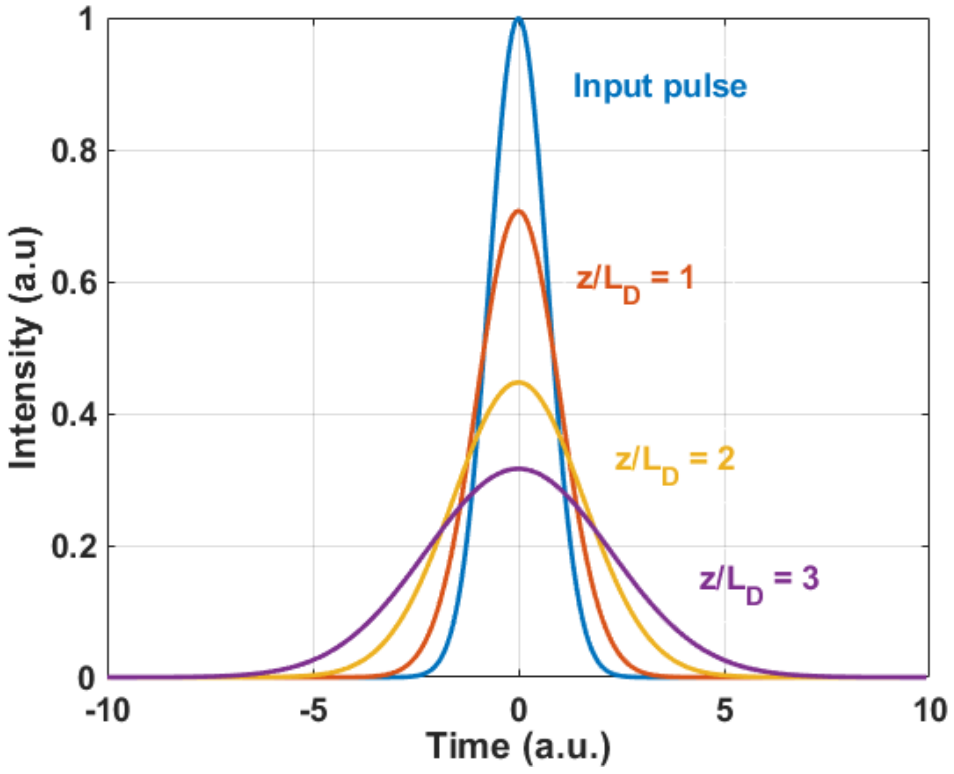

Figure 2.5: Broadening of the Full-width at half maximum of the unchirped pulse while propagating in the fiber for $z/L_D = 1$, 2, and 3, respectively.

the time-derivative of the phase (Eq. 2.21),

$$\delta\omega_{GVD}(z,t) = \frac{2\beta_2 z}{\Delta\tau^4 + \beta_2^2 z^2} t. \tag{2.24}$$

The equation indicates that the pulse undergoes a linear chirp (linear dependence on t) due to the influence of GVD while it travels through the fiber. This depends on the sign of β_2. When $\beta_2 > 0$ (normal dispersion) the leading edge of the pulse ($t < 0$) will undergo a negative chirp while the trailing edge will exhibit a positive chirp and the opposite will occur when $\beta_2 < 0$ (anomalous dispersion). The pulse will broaden in any case because its width depends on β_2^2 (Eq. 2.20). The above discussion did not take into account the temporal chirp. Temporal chirp ($\delta\omega$) is the variation of the pulse instantaneous frequency over time. An up-chirp with a chirp parameter $C > 0$, signifies that the instantaneous frequency increases with time, and vice versa for a down-chirp. If the pulse is initially chirped ($C \neq 0$) then the pulse may experience broadening or compressing based on the sign of $\beta_2 C$. When it is positive (both β_2 and C have the same sign), the pulse accumulates the initial chirp and the dispersion-induced chirp, and, as a result, the pulse widens more rapidly than that of the unchirped pulse. Alternatively, when β_2 and C have opposite signs, the pulse will undergo compression at first and eventually broaden again [78].

2.2.3 Nonlinear effects in optical fiber

In optics, linear and nonlinear effects refer to phenomena that are not affected by changes in intensity and those that are influenced by changes in intensity, respectively. Besides the inelastic scattering nonlinear effects, the reason for other nonlinear effects in optical fibers is the alterations in the medium's refractive index due to propagating pulse intensity (Kerr effect). The Kerr effect can appear in various ways, including self-Phase Modulation (SPM), cross-Phase Modulation (XPM), and four-wave mixing (FWM), depending on the input signal. In this thesis, the SPM and FWM will be discussed while neglecting the effects of XPM. The basic equation to describe the nonlinear effects in an optical fiber for

a linearly-polarized light along the principal axis of the fiber is given by:

$$P = \epsilon_0 \left[\chi^{(1)} E + \chi^{(2)} EE + \chi^{(3)} EEE + \cdots \right], \tag{2.25}$$

where $\chi^{(n)}$ is n^{th} order susceptibility and is a tensor of rank $n+1$. The first term in the above equation is the effect induced by linear susceptibility. As optical fiber exhibits inversion symmetry $\chi^{(2)} = 0$, so the lowest-order nonlinear effects in fibers are attributed to the third-order susceptibility $\chi^{(3)}$.

The intensity-dependent index of refraction can be written as,

$$n(\omega, I) = n_0(\omega) + n_2 I \tag{2.26}$$

where $n_0(\omega)$ is the material's linear refractive index while n_2 is the nonlinear index responsible for the effects of SPM and XPM and is given by:

$$n_2 = \frac{3}{8n_0} \Re \left(\chi^{(3)} \right). \tag{2.27}$$

2.2.4 Self-phase modulation

Self-phase modulation (SPM) is an intensity-dependent phenomenon that causes the optical pulses to become broader in spectral domain [161–166]. The fundamental explanation of the SPM is that, when a light of high intensity passes through an optical fiber, there is a change in the refractive index of the fiber material (Eq. 2.26). This change in the refractive index, in turn, modifies the phase of the light pulse. This effect is known as self-phase modulation because the pulse itself modifies its own phase. The phase shift is proportional to the square of the intensity of the pulse, so it implies that the high-intensity part of the pulse will induce more phase shift than the low-intensity part of the pulse. The pulse propagation through optical fiber with only nonlinear effects (ignoring the losses and

dispersive effects) is written as:

$$\frac{\partial A}{\partial z} = i\gamma|A|^2 A \tag{2.28}$$

This equation can be readily solved in the time domain,

$$A(z,t) = A(0,t)\exp\left[i\gamma|A(0,t)|^2 z\right], \tag{2.29}$$

where $A(0,t)$ is given in Eq. 2.17. The temporal nonlinear phase is given by:

$$\phi_{NL} = \gamma|A(0,t)|^2 z, \tag{2.30}$$

and it is proportional to both the intensity of the pulse and the propagation distance. SPM results in a phase shift that is determined by the intensity of the pulse, but it does not have any effect on the shape of the pulse (Eq. 2.29). The instantaneous frequency of a Gaussian pulse is plotted in Fig. 2.6 and can be calculated by taking the time-derivative of the nonlinear phase,

$$\delta\omega_{SPM}(z,t) = 2\gamma z\left(\frac{t}{\Delta\tau^2}\right)\exp\left[\frac{-t^2}{\Delta\tau^2}\right] \tag{2.31}$$

The corresponding broadening of the pulse in the spectral domain is shown in Fig. 2.7. The fiber was assumed to have a γ value of 11 $W^{-1}{\cdot}km^{-1}$ while the distance covered by the pulse was approximately 0.18 km. The pulse initial duration was evaluated to be 6.6 ps having a peak power of 20 W. The nonlinear phase comes out to be $\phi_{NL} \approx 12.5\pi$. The structured spectral shape of the pulse after the propagation in the optical fiber is due to the fact that each frequency has two distinct nonlinear phase shifts (for instance in Fig. 2.6 at two different times (t_1 and t_2) the instantaneous frequency values are the same, but the phase shifts are different because the phase shift profile follows the pulse temporal shape) and they interfere constructively or destructively with each other, resulting in such a structured (oscillatory) pattern [78]. Contrary to the chirp induced by the GVD (either

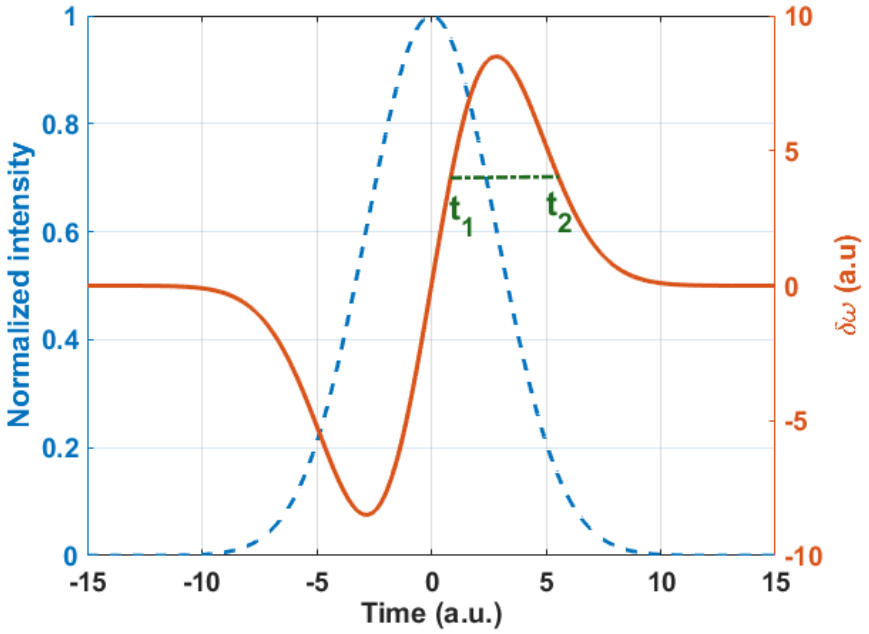

Figure 2.6: The input pulse with pulse duration of 6.6 ps is shown in **dotted blue**, while the associated frequency chirp is plotted in **orange**. The other parameters for the calculation are: fiber length = 180 cm, $\gamma = 11$ W^{-1}·km^{-1}, while the peak power is 20 W. The chirp profile follows the profile of the time derivative of the Gaussian pulse.

positive or negative on both the front and back end of the pulse, respectively), the chirp caused by the SPM is always negative at the front edge of the pulse and positive at the back edge of the pulse (Fig. 2.6, considering $n_2 > 0$). Similarly, the chirp is linear with a positive slope near the central part of the pulse, and this linear shape of the chirp is related to the Gaussian pulse shape. The chirp profile of other pulse shapes, for instance, super-Gaussian, is discussed in chapter 4.

2.3 Pulse shaping regimes of operation

The complicated nonlinear dynamics of the pulses in mode-locked fiber lasers originate from the interaction of multiple aspects in the cavity, including dispersion, and nonlinear effects [167]. The operating regimes (and the corresponding pulse shape associated with it) are the

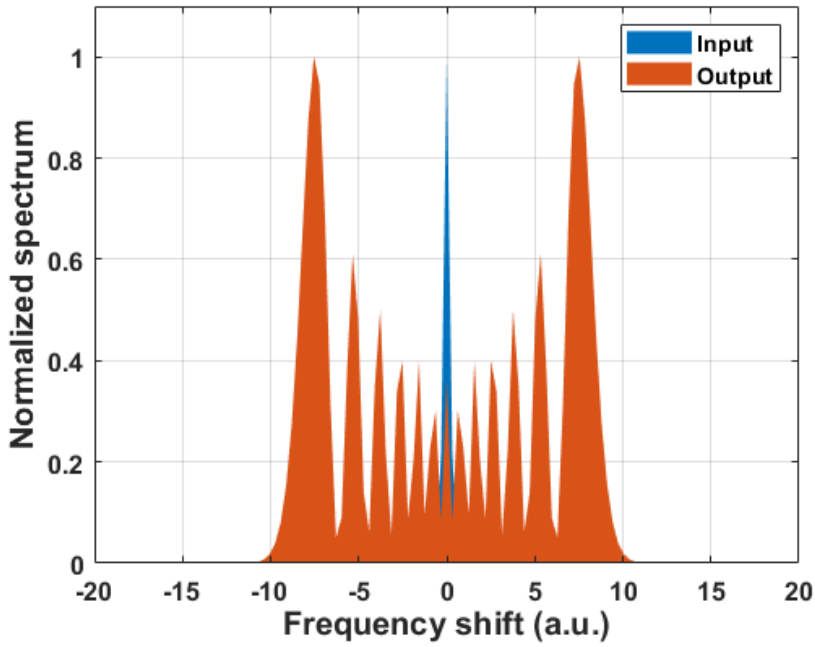

Figure 2.7: The injected pulse spectrum in the optical fiber is plotted in **blue** while the output spectrum is plotted in **orange**. The input spectrum is calculated by taking the Fourier transform of an unchirped Gaussian pulse having a pulse duration of 6.6 ps. For the calculation purpose only the effect of self-phase modulation is considered ignoring all other effects including the losses.

soliton regime (sech^2), stretched-pulsed regime (Gaussian), self-similar regime (parabolic), and dissipative soliton regime (flat-top). Although nonlinear effects significantly impact the dynamics of these various regimes, the primary factor used to designate these regimes is the overall group velocity dispersion (GVD) of the laser cavity.

2.3.1 Soliton regime

The pulse propagation equation (Eq. 2.12) in the optical fiber shows two factors that vary the phase i.e. GVD and the nonlinearity. Their effects are discussed above separately, but the Soliton regime combines the effect of GVD and nonlinearity. The soliton is a solution [168–175] of the Eq. 2.12 in which the phase shift caused by the nonlinearity

is compensated by the phase shift induced by the anomalous dispersion and in this case, the chirp is perfectly adjusted. The soliton maintains its shape and amplitude along its propagation in the optical fiber in both temporal and spectral domains due to the balance between dispersion and nonlinearity. For the soliton formation, the laser cavity needs to have a negative dispersion ($\beta_2 < 0$), and, in this case, the solution of Eq. 2.12 depends on the soliton order integer (N) given in the absence of attenuation ($\alpha = 0$), by:

$$N = \sqrt{\frac{\gamma P_p \Delta\tau^2}{|\beta_2|}} \tag{2.32}$$

where $N = 1$ refers to fundamental soliton order where the phase alteration caused by the GVD and SPM is nullified completely, while for $N > 1$, they are identified as higher-order solitons. The term P_p is the peak power of the pulse. For $N = 1$ the solution takes the form,

$$A(t, z) = \sqrt{P_p}\left[\text{sech}\left(\frac{t}{\Delta\tau}\right)\right]\exp\left(i\frac{\gamma P_p z}{2}\right), \tag{2.33}$$

where $P_p\Delta\tau^2 = \frac{|\beta_2|}{\gamma}$ is the square of the product of the amplitude and duration of the fundamental soliton. As β_2 and γ are fixed by the fiber characteristics, it suggests that $P_p\Delta\tau^2 \approx$ constant and the energy of the pulse associated with it is given by $E_p \approx \frac{|\beta_2|}{\gamma\Delta\tau}$ [168]. It is clear that the energy is limited and this is the main reason for not achieving high-energy pulses using fundamental soliton operation compared to its counterparts (dissipative soliton). For specific values of β_2 and γ of the fiber, the solutions for the fundamental soliton follow the curve shown in Fig. 2.8 which shows that low-energy soliton is achieved for long pulse durations and high-energy soliton is obtained for short pulse durations. Getting high-energy pulses is possible either by increasing the injected power into the fiber or by lowering the pulse duration, but there are limitations to both. Increasing the input power will increase the output pulse energy up to a certain extent (restricted by the energy-area-theorem), and further increasing the input power will result in multiple pulsing [3]. Additionally, when there is no exact balance between the β_2 and γ, then

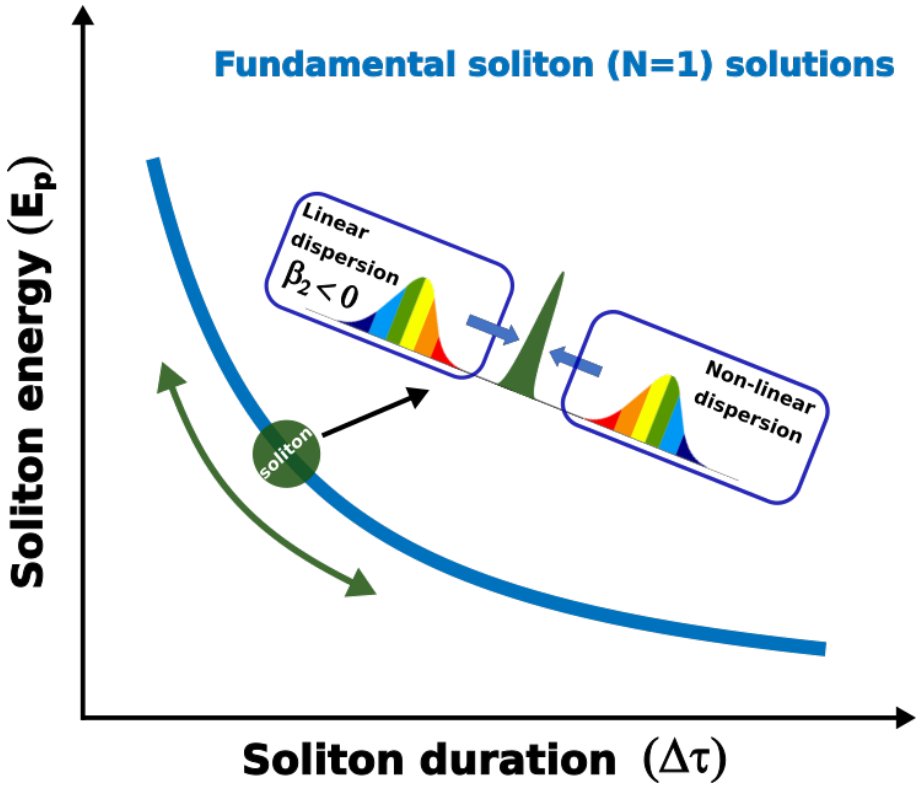

Figure 2.8: The solutions of the fundamental soliton (N=1) at different pulse durations and the corresponding output pulse energy. The solution suggests that high-energy solitons are only achievable for short pulse durations.

there exists a higher-order soliton. Another limitation to the soliton regime is the pulse wave-breaking [176], when the phase acquired due to nonlinearity exceeds by a lot than dispersion, then the linear dispersion is not enough to compensate and eventually pulse wave-breaking occurs.

2.3.2 Stretched-pulse regime

One way to handle nonlinearity is by constructing the fiber laser cavity with alternating sections of normal and anomalous group velocity dispersion (GVD). During one complete round trip, the pulse stretches and compresses, causing a breathing effect [177–179]. Due to this stretching of the pulse in the laser cavity, this regime of operation is designated as a

stretched-pulse regime. As the chirp fluctuates within the laser cavity (twice in one round trip), it is often necessary to dechirp the output pulse. The utilization of both soliton and chirped pulses enables higher pulse energies due to the fact that a chirped pulse with the same peak power as a transform-limited pulse possesses more energy [180].

2.3.3 Self-similar regime

A pulse that adjusts itself to get a resized replica of itself while traversing in a normal dispersion region of the laser cavity is a solution to the NLSE which has an intensity profile that resembles a parabolic shape [5, 181]. Usually, in this regime, the nonlinearity is minimal in the anomalous dispersion section of the laser cavity to prevent the soliton formation, while the combined effect of GVD and SPM leads to the upsurge of a linear chirp across the pulse in the normal dispersion section of the cavity. Interestingly, this linear chirp has been demonstrated to make the pulse resistant to optical wave breaking [182].

2.3.4 Dissipative soliton regime

The soliton regime discussed above takes only the dispersive effect and not the dissipative effects at all. The concept of dissipative soliton is the extension of the soliton regime that considers the effects of the gain and losses in addition to the dispersive effects as shown in Fig. 2.9. Dissipative solitons arise due to the combined effect of normal cavity dispersion, nonlinearity, gain-bandwidth filtering, and gain saturation. The characteristics of dissipative solitons are governed by the complex Ginzburg-Landau equation (CGLE) [183, 184](which is the extension of the NLSE) considering propagation in gain fiber:

$$\frac{\partial A}{\partial z} + \beta_1 \frac{\partial A}{\partial t} + i\beta_2 \frac{\partial^2 A}{\partial t^2} = i\gamma(\omega_0)|A|^2 A + (G_T + \zeta|A|^2)A + \frac{1}{\Omega_{BW}} \frac{\partial^2 A}{\partial t^2}, \tag{2.34}$$

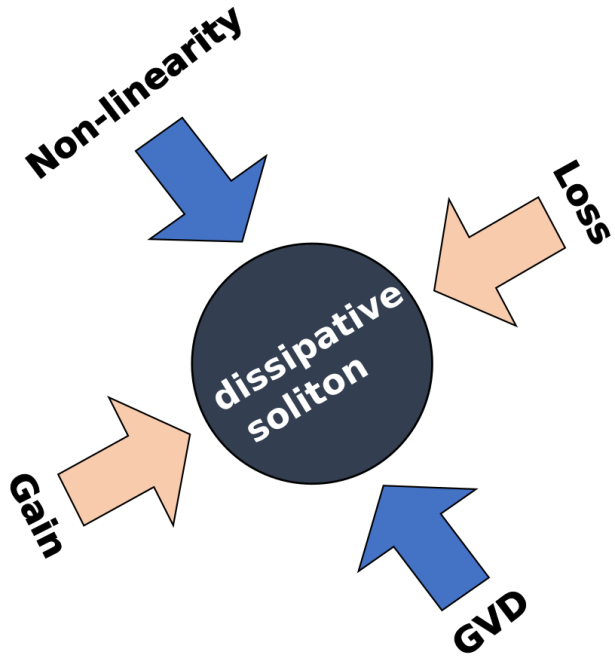

Figure 2.9: Dissipative soliton is the localized solution that originates from the combined balance between the linear dispersion and nonlinearity, and between the gain and the loss.

where G_T is the combined effects of the gain and output coupling losses, Ω_{BW} denotes the spectral amplitude effects (gain or spectral filter bandwidth), while ζ comprises the amplitude modulation effects of the saturable absorber. The solution of this equation is a chirped hyperbolic-secant profile [136]. Contrary to the conventional soliton, when the laser cavity has $\beta_2 > 0$, which designates the normal dispersion regime operation, the key factors for producing stable pulses within the fiber cavity are the dissipative mechanisms of spectral filtering and saturable absorption, while the pulse shape grows to have a parabolic profile with linear frequency chirp [6, 181, 185]. The pulse shaping is governed by the gain narrowing as a result of filtering the edges of the pulse in the spectral domain [6, 136]. The fiber laser oscillator with all components having normal dispersion ($\beta_2 > 0$) is referred to as the "All-normal-dispersion (ANDi)" laser cavity. The important factors to consider in an all-normal-dispersion laser cavity are spectral filtering, nonlinear phase shift, and the GVD, which eventually characterize pulse shaping and pulse evolution inside the laser cavity. A detailed study of all these effects is investigated in Ref. [186]. One of the important aspects

of the ANDi laser is that the output pulses are heavily chirped and it needs to be de-chirped outside.

2.4 All-normal dispersion fiber laser

As discussed, ultrashort pulse generation necessitates compensating for group velocity dispersion (GVD). A significant net anomalous GVD leads to soliton-like pulses, whereas nearly zero net GVD allows for stretched-pulse operation. Researchers have investigated mode-locked laser operation with a substantial net normal GVD to achieve stable high-energy pulses, exemplified by the chirped pulse oscillator [187] and self-similar laser [5]. An all-normal-dispersion (ANDi) laser was introduced to achieve high-energy pulses, which uses spectral filtering to shape highly-chirped pulses without any anomalous GVD elements [186] in the cavity. The interplay of normal dispersion, self-phase modulation, and gain produces robust pulses with positive frequency chirp, enabling superior pulse energy performance by preventing pulse breaking due to fiber nonlinearity [188]. The pulse chirp shows a monotonic increase in the normal dispersion sections of the laser cavity. Fig. 2.10 illustrates the key elements of the conventional all-normal-dispersion fiber laser [186]. A

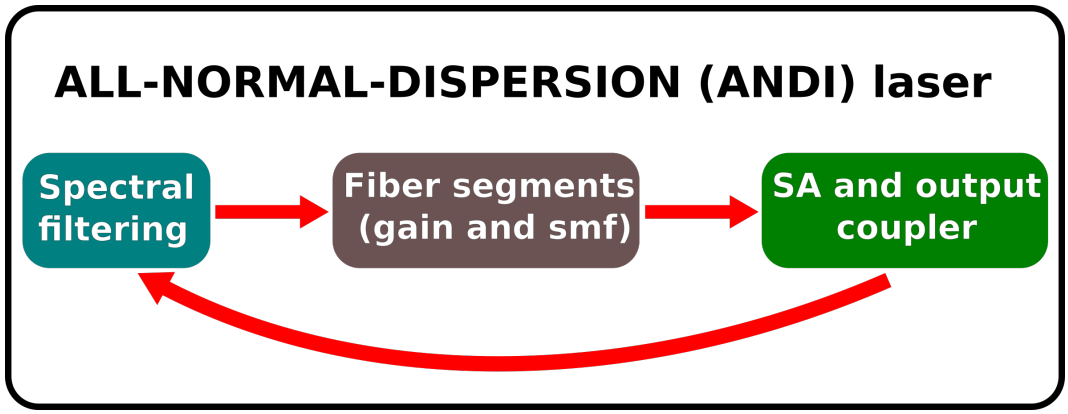

Figure 2.10: Main components of the ANDi fiber laser. SMF: single-mode-fiber, SA: Saturable absorption.

brief explanation of the pulse propagation in the spectral domain in the ANDi fiber cavity is as follows. The pulse spectrum displays sharp edges after propagating through the spectral filter, and the top of the spectrum has a shape according to the transmission curve of the filter, for instance Gaussian-shaped transmission curve will result in a Gaussian-type spectrum with sharp edges. Subsequently, the spectrum undergoes broadening as it passes through segments of the gain fiber and the single-mode fiber. The broadening effect is more pronounced after passing through the gain fiber due to the high peak power. This leads to an increased nonlinear phase shift, causing sharp peaks to emerge at the spectrum's edges, often referred to as a 'cat-ear' or 'Batman-shaped spectrum' [186, 189]. The time-domain explanation of the pulse propagation in the ANDi fiber laser cavity is as follows. The duration of the pulse consistently gets longer within the sections of single-mode and gain fibers. Afterward, the self-amplitude modulation takes place in both the saturable absorber and the spectral filter, but the spectral filter predominantly affects the temporal development of the pulse and brings the pulse duration down to its initial duration [186].

Chapter 3

Four-wave-mixing (FWM) in optical fiber and fiber optical parametric oscillator(FOPO)

Contents

This chapter provides an overview of the four-wave mixing (FWM) process in optical fibers. It explains the coupled amplitude equations governing FWM and derives equations for parametric generation and amplification. In addition, it also covers the discussion about the phase matching condition specific to FWM in optical fibers. The chapter concludes with a brief introduction to the fiber optical parametric oscillator (FOPO).

3.1 Introduction to four-wave mixing (FWM)

After the invention of the laser [96], the field of nonlinear optics greatly evolved since then [190]. Besides all other phenomena associated with the nonlinear optics field, this discussion is only dedicated to the four-wave mixing process. The Four-wave mixing is a parametric process involving the interaction among four waves or four photons [78, 191] through the third-order nonlinear susceptibility $\chi^{(3)}$. The process of four-wave mixing is explained in Fig 3.1. The four photons interact in such a way that two photons at the pump frequencies $(\omega_{p1}, \omega_{p2})$ are annihilated and simultaneously generate two other photons at different frequencies (ω_s, ω_i). The conservation of energy governs the frequencies that are generated during the process $(\omega_s + \omega_i = \omega_{p1} + \omega_{p2})$, while the efficiency related to the parametric generation is well-explained by the conservation of momentum principle, which leads to the phase-matching condition. The latter is discussed in detail in the upcoming section (Sect. 3.1.2). In a single-pump configuration, two photons at the pump frequency (ω_p) are annihilated, generating two photons at signal and idler frequencies (ω_s, ω_i). In this case, there are basically three-waves [192] involved in this process, and it is called the degenerate-four-wave mixing (DFWM), as shown in Fig. 3.2

3.1.1 Coupled amplitude equations of FWM and parametric generation

The conventional approach for representing the nonlinear response of a fiber is to express the resulting polarization as a series of powers of the induced electric field [193, 194] while considering the electric field is linearly polarized along the principal axis of a single mode fiber:

$$P = \epsilon_0 \left[\chi^{(1)}E + \chi^{(2)}EE + \chi^{(3)}EEE + \cdots\right], \tag{3.1}$$

where P is the induced polarization and E is the electric field. $\chi^{(1)}$, $\chi^{(2)}$, and $\chi^{(3)}$ are the linear, second-order nonlinear, and third-order nonlinear susceptibilities. As fibers

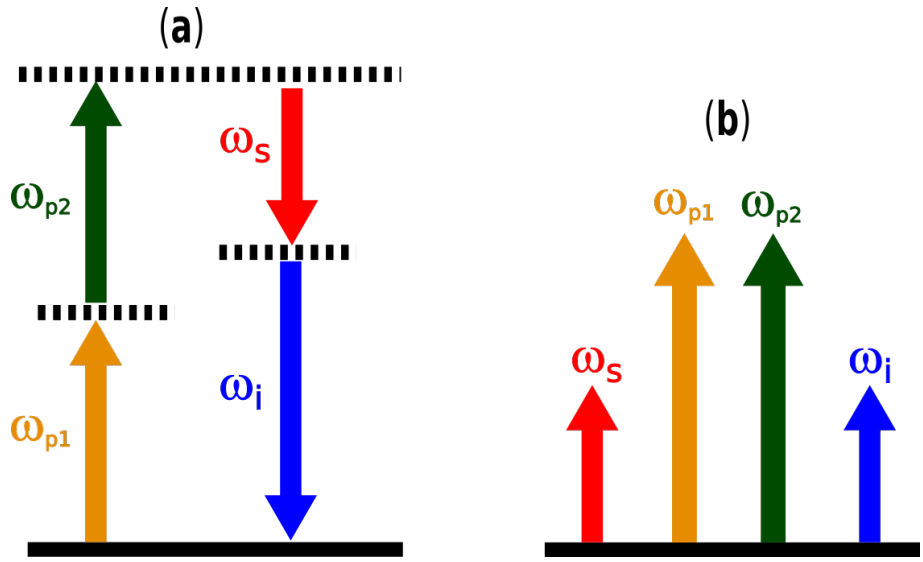

Figure 3.1: (a) Energy level diagram of FWM (b) Involved frequencies in FWM.

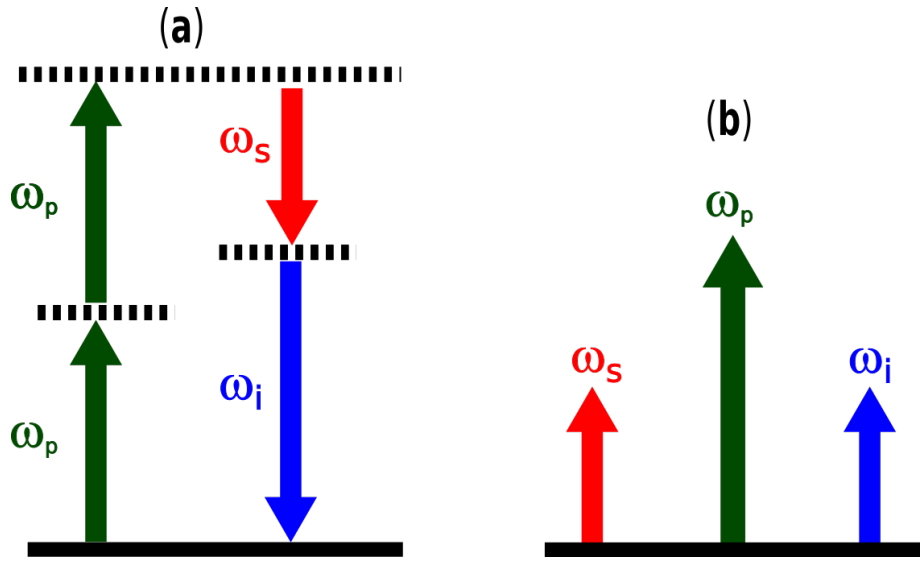

Figure 3.2: (a) Energy level diagram of degenerate-FWM (b) Involved frequencies in DFWM.

are centrosymmetric materials, the lowest-order non-linearity comes from $\chi^{(3)}$. FWM is governed by the third-order nonlinear susceptibility $\chi^{(3)}$,

$$P^{(3)} = \epsilon_0 \left[\chi^{(3)} EEE\right]. \tag{3.2}$$

The following group of equations describes the evolution of the amplitude of four waves at frequencies ω_{p1}, ω_{p2}, ω_s, and ω_i associated with the FWM process while propagating collinearly in z direction [78],

$$\frac{dA_{p1}}{dz} = -\frac{\alpha}{2}A_{p1} + i\gamma\left[|A_{p1}|^2 + 2|A_{p2}|^2 + 2|A_s|^2 + 2|A_i|^2\right]A_{p1} + \left[2i\gamma A_{p2}^* A_s A_i\right]e^{i\Delta\beta z} \quad (3.3)$$

$$\frac{dA_{p2}}{dz} = -\frac{\alpha}{2}A_{p2} + i\gamma\left[2|A_{p1}|^2 + |A_{p2}|^2 + 2|A_s|^2 + 2|A_i|^2\right]A_{p2} + \left[2i\gamma A_{p1}^* A_s A_i\right]e^{i\Delta\beta z} \quad (3.4)$$

$$\frac{dA_s}{dz} = -\frac{\alpha}{2}A_s + i\gamma\left[2|A_{p1}|^2 + 2|A_{p2}|^2 + |A_s|^2 + 2|A_i|^2\right]A_s + \left[2i\gamma A_{p1} A_{p2} A_i^*\right]e^{-i\Delta\beta z} \quad (3.5)$$

$$\frac{dA_i}{dz} = -\frac{\alpha}{2}A_i + i\gamma\left[2|A_{p1}|^2 + 2|A_{p2}|^2 + 2|A_s|^2 + |A_i|^2\right]A_i + \left[2i\gamma A_{p1} A_{p2} A_s^*\right]e^{-i\Delta\beta z} \quad (3.6)$$

where A_{p1}, A_{p2}, A_s, and A_i are the amplitudes of pumps, signal, and idler waves respectively, while the * represent the conjugate field, and α is the absorption coefficient. The important thing to notice in Eqs. 3.3 - 3.6, is the $\Delta\beta$ term which is the phase mismatch term, defined as $\Delta\beta = \beta_{p1} + \beta_{p2} - \beta_s - \beta_i$. The above equations account for different effects, i.e. the losses, the SPM, the XPM, and the pump depletion. For simplicity, the intensities of the pump frequencies are assumed to be high enough (and the losses are lower enough) so that they are considered undepleted during the FWM process, and the solution for the pump equations (Eqs. 3.3 and 3.4) then writes,

$$A_{p1}(z) = A_{p1}(0)\exp\left[i\gamma(P_{p1} + 2P_{p2})z\right], \quad (3.7)$$

$$A_{p2}(z) = A_{p2}(0)\exp\left[i\gamma(2P_{p1} + P_{p2})z\right]. \quad (3.8)$$

Here, $P_{p(1,2)} = |A_{p(1,2)}(0)|^2$ is the pump power at $z = 0$. From the Eqs. 3.7, and 3.8, it is clear that the phase of the pump waves is altered as a result of SPM and XPM. Replacing the solutions of the pump equations in Eq. 3.5 and 3.6, respectively, the coupled amplitude equations for the parametric waves are:

$$\frac{dA_s}{dz} = 2i\gamma\left[(P_{p1} + P_{p2})A_s + A_{p1}(0)A_{p2}(0)\exp\left\{-i\left(\Delta\beta - 3\gamma(P_{p1} + P_{p2})\right)z\right\}A_i^*\right], \quad (3.9)$$

$$\frac{dA_i}{dz} = -2i\gamma\left[(P_{p1} + P_{p2})A_i^* + A_{p1}(0)^* A_{p2}(0)^*\exp\left\{i\left(\Delta\beta - 3\gamma(P_{p1} + P_{p2})\right)z\right\}A_s\right]. \quad (3.10)$$

The approximate general solutions of these equations are by considering the boundary conditions of the undepleted pump and only the presence of the signal field $A_s(0)$ at $z = 0$ i.e., along with the pump fields [70, 78],

$$A_s(z) = A_s(0)\left[\cosh(gz) + i\left(\frac{\kappa}{2g}\right)\sinh(gz)\right]e^{(-i\kappa z/2)}, \tag{3.11}$$

$$A_i(z)^* = A_s(0)\left[-i\frac{\gamma}{g}A_{p1}(0)A_{p2}(0)\sinh(gz)\right]e^{(i\kappa z/2)}. \tag{3.12}$$

Here, $\kappa = \Delta\beta + \gamma(P_{p1} + P_{p2})$ is the absolute phase matching term, while g is the parametric gain which is written as,

$$g = \sqrt{\left(\frac{2\gamma P_{p1}P_{p2}}{P_{p1}+P_{p2}}\right)^2 - \left(\frac{\kappa}{2}\right)^2}. \tag{3.13}$$

In the case of single pump configuration (degenerate four-wave-mixing), the κ and g can be simplified to $\kappa = \Delta\beta + 2\gamma P_p$, $g = \sqrt{(\gamma P_p)^2 - \left(\frac{\kappa}{2}\right)^2}$, respectively. The FWM process is efficient at perfect phase-matching conditions, for that, κ should be zero, and the gain is maximum at this point. From now onward in the manuscript, the degenerate case will be considered for simplicity. The power of the signal and idler fields ($|A_s(z)|^2$ and $|A_i(z)|^2$) can be calculated from Eq. 3.11 and 3.12, respectively,

$$P_s(z) = P_s(0)\left[1 + \left(1 + \frac{\kappa^2}{4g^2}\right)\sinh^2(gz)\right], \tag{3.14}$$

$$P_s(z) = P_s(0)\left[\left(1 + \frac{\kappa^2}{4g^2}\right)\sinh^2(gz)\right]. \tag{3.15}$$

It can be seen from Eqs. 3.14 and 3.15, that the signal and idler powers are amplified with the propagation distance z. For the fiber length (L), the amplification factor of the signal field is,

$$G_s = \frac{P_s(L)}{P_s(0)} = \left[1 + \left(1 + \frac{\kappa^2}{4g^2}\right)\sinh^2(gL)\right]. \tag{3.16}$$

The parametric gain bandwidth (BW_{G_s}) (full-width at half maximum of the parametric amplification factor (Eq. 3.16)) can also be calculated from the above equation and relies on various variables, for instance, pump peak power, propagation distance, and the dispersion properties of the fiber [70, 78], and it is approximated by:

$$\mathrm{BW}_{G_s} \approx \frac{\pi}{L} \frac{1}{\sqrt{2\gamma P_p |\beta_2|}}. \tag{3.17}$$

The simulation and experimental results of the β_2 dependency on the amplification bandwidth are well-explained in the upcoming chapter. Noteworthy is that the higher-order dispersion parameters are included while working near zero-dispersion wavelength.

3.1.2 Phase matching condition

As discussed in the last section, the highest value for the parametric gain and its amplification factor is achieved for perfect phase matching condition $\kappa \approx 0$. One can write κ as follows:

$$\kappa = \Delta\beta_L + \Delta\beta_{NL}, \tag{3.18}$$

where $\Delta\beta_L$ and $\Delta\beta_{NL}$ represent the mismatch terms due to linear and nonlinear effects respectively. The linear effects are due to the material and wave-guide dispersion effects [78] and are related to the fiber properties. As for the equations and discussion, the single-mode operation is considered, which is why the wave-guide contribution is neglected. So, κ writes:

$$\kappa = [\Delta\beta_L] + [\Delta\beta_{NL}] = [-2\beta(\omega_p) + \beta(\omega_s) + \beta(\omega_i)] + [2\gamma P_p]. \tag{3.19}$$

Extending the linear part of the Eq. 3.19 by Taylor series approximation centered around the pump frequency, it can be written as,

$$\kappa = \frac{\beta_6(\omega_p)}{360}\Delta\omega^6 + \frac{\beta_4(\omega_p)}{12}\Delta\omega^4 + \beta_2(\omega_p)\Delta\omega^2 + 2\gamma P_p, \tag{3.20}$$

where $\Delta\omega = \omega_s - \omega_p = \omega_p - \omega_i$ is the angular frequency shift. The above equation indicates that only the even-order dispersion parameters contribute to the linear phase mismatch. Although the contribution of the higher order-dispersion terms (β_4, β_6) are negligible compared to β_2, but they can be significant when working near zero-dispersion wavelength ($\beta_2 \approx 0$). As the nonlinear contribution is always positive, for the phase-matching to occur, the pump wavelength should lie in the anomalous dispersion regime [78]. If the pump wavelength is in the normal dispersion range, then the phase matching can be attained given the fact that higher dispersion terms (β_4 and so on) are made negative [195], and this is possible in micro-structured fibers [196, 197]. The implication of Eq. 3.20 is discussed in the simulation part in chapter 5.

3.2 Fiber optical parametric oscillator

To make a fiber optical parametric oscillator (FOPO), a feedback loop is constructed around the fiber optical parametric amplifier (FOPA) discussed above. Typically, without a seed signal, the FOPO is made via a single pump configuration, and the signal and idler waves are generated from quantum noise depending on the phase-matching requirements [78] and amplified when circulated in the feedback cavity. The simple fiber OPO cavity comprised of $\chi^{(3)}$ nonlinear material is shown in Fig. 3.3. Although this section is dedicated to $\chi^{(3)}$-based OPOs, they are still lacking in various aspects compared to $\chi^{(2)}$-based OPOs. Initially, OPOs were exclusively attainable utilizing solid-state devices and the prime advantage of these OPOs was their ability to generate the signal and idler wavelengths over a wide range compared to $\chi^{(3)}$-based OPOs. This flexibility allows for

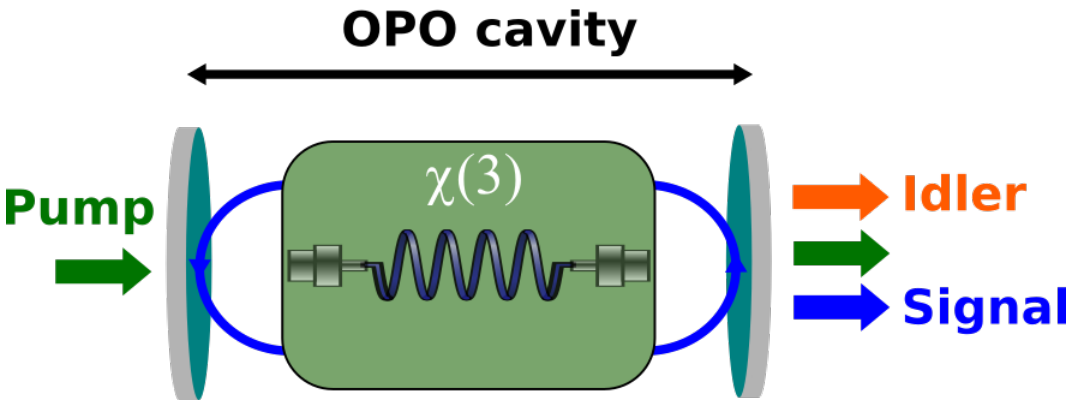

Figure 3.3: OPO linear cavity comprised of $\chi^{(3)}$ material (nonlinear fiber) and the feedback mirrors. The cavity is resonant for the signal and is amplified when propagating back and forth in the OPO cavity.

the generation of wavelengths that are challenging or even unattainable using traditional lasers, such as those in the UV and mid-to-far-infrared regions [198–200]. Additionally, the magnitude of non-linearity is low in $\chi^{(3)}$-based OPOs compared to $\chi^{(2)}$-based OPOs, this means the threshold power levels are low for the latter, and the parametric generation can be achieved even with CW-pump configuration. While they possess numerous benefits, they also come with their own set of drawbacks, the primary ones being their bulky size and expensive nature. Additionally, they are prone to thermal and phase-mismatch instabilities. Conversely, fiber-based OPOs based on four-wave-mixing have been shown to exhibit interesting features such as good beam quality, robustness, and compactness [16,17,74,201].

Chapter 4

ANDi laser setups, experimental results and simulations

Contents

In this chapter, we will explore first the experimental configuration and result of the conventional femtosecond all-normal-dispersion (ANDi) fiber laser. We then proceed to

discuss the picosecond ANDi fiber laser, explaining both experimental findings and thorough numerical simulations. Finally, we conclude the chapter by addressing pulse evolution within Gaussian and super-Gaussian filters. It is worth noting that the contents presented in this chapter are mainly taken from our published article [31].

4.1 Femtosecond ANDi laser

Before going into the specifics of the main ANDi setup for this Ph.D. work, I will first explain the conventional femtosecond ANDi setup that was built in our laboratory. I have conducted a brief characterization of this setup to externally compress the pulses.

The schematic shown in Fig. 4.1 consists of a combination of single-mode and gain fibers, along with the waveplates, polarizer, and birefringent filter. The pump laser diode pumps the gain fiber at 976 nm through the combiner and the signal light generated is

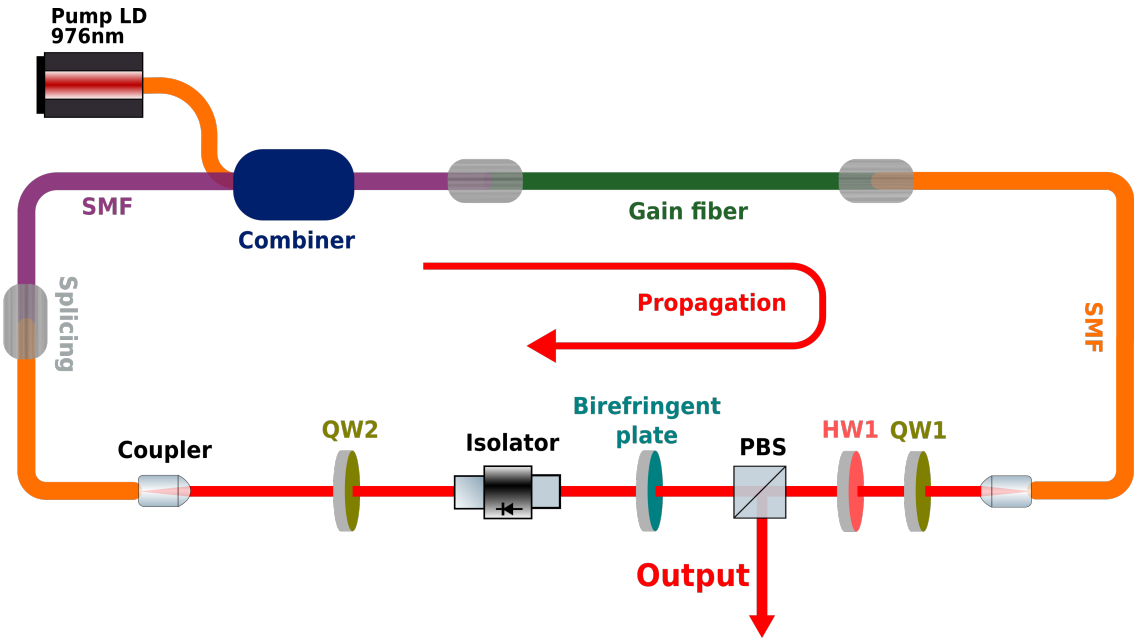

Figure 4.1: Experimental setup for the ANDi fiber oscillator. LD: laser diode, SMF: single-mode fiber, PBS: polarizing beam splitter, QW: quarter-waveplate, HW: half-waveplate.

propagated through the laser cavity. The gain fiber spans approximately 180 cm, followed by a single-mode fiber of about 70 cm in length. The total length of single-mode fibers leading to the coupler before the gain fiber measures $\sim$ 90 cm. The free space, including all the components, accounts for an additional 34 cm. Altogether, the cavity's total length measures approximately 530 cm, resulting in a repetition rate of roughly 57 MHz. The core diameter of the single mode fibers and gain fiber is around 10 µm with the standard cladding diameter of 125 µm. Pulsed operation in the laser cavity is achieved by the nonlinear polarization rotation (NPR) technique as discussed in Section 2.1.2.1. Thanks to the NPR along with the combination of two $\lambda/4$-waveplates (QW1, QW2), one $\lambda/2$-waveplate (HW1), optical isolator, called hereinafter nonlinear output port (NLOP), only the high-intensity part of the pulse is transmitted inside the laser cavity, while blocking the low-intensity part of the pulse, imitating the principle of operation of saturable absorber (SA). The photograph of the laser setup in the laboratory is shown in Fig. 4.2. In the following paragraphs, we will briefly present the results achieved using this ANDi laser.

The average power obtained for the mode-locked output was around 601 mW at the pump power of 1.8 W. The RF and optical spectra obtained at the output are plotted in

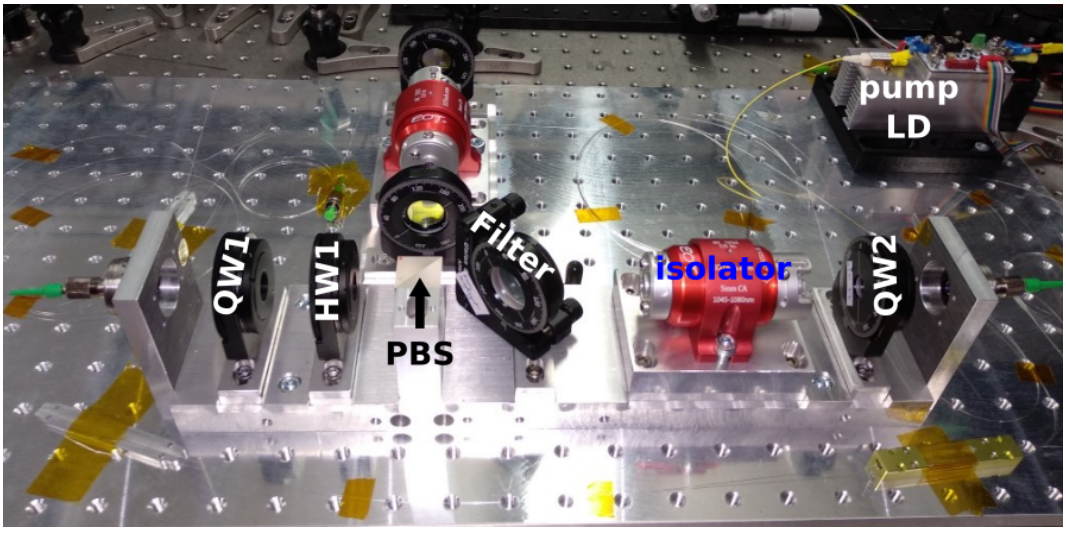

Figure 4.2: Photograph of the all-normal-dispersion (ANDi) fiber laser with the mentioned free space components.

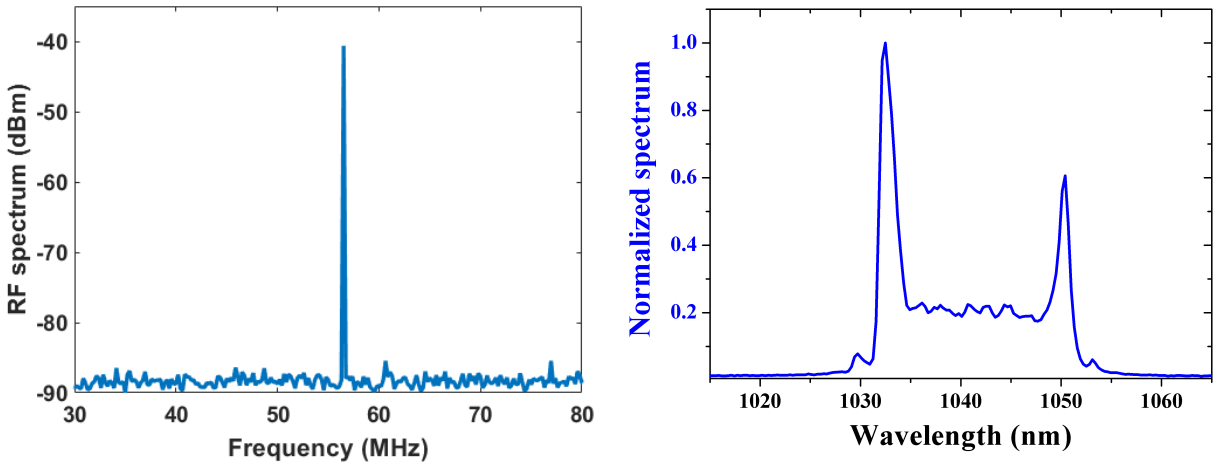

Figure 4.3: (**Left**) The RF spectrum at the output of ANDi fiber laser shows the fundamental repetition rate of around 56.6 MHz. (**Right**) Optical spectrum obtained at the output of ANDi laser. The spectral width is around 20 nm, while the spectrum has a characteristic shape of 'cat-ear' or 'Batman'.

Fig. 4.3. The fundamental repetition rate is $\sim$ 56.6 MHz. The optical spectrum has a characteristic shape of 'cat-ear' or 'Batman-shaped' [186, 189]. The spectral width of the spectrum is $\sim$ 20 nm. The autocorrelation trace obtained at the output of the ANDi laser cavity is graphed in Fig. 4.4. The autocorrelation width is around 3.16 ps. Considering a Gaussian pulse, the pulse duration is $\sim$ 2.24 ps. For a Gaussian pulse, the pulse duration is written as, $\tau_p = \tau_{ac}/\sqrt{2}$, with τ_{ac} as autocorrelation full-width at half maximum.

We have also carried out simulations for this ANDi laser to validate the experimental results. The computations were performed using Julia programming, considering the same parameters as presented in the experimental results. The pulse is propagated through the gain fiber and single-mode fibers having lengths similar to the ones we used in the experimental setup. Afterward, the pulse is sent through a saturable absorber (SA) that mimics the role of the nonlinear polarization rotation for pulsed operation. The propagation of the laser pulse within the amplifying fiber is simulated by solving the nonlinear Schrödinger equation (Eq. 2.34). The numerical model is solved with a standard split-step algorithm. At a repetition rate of almost 57 MHz, an average power of 554 mW (pulse energy: $\sim$ 9.8 nJ) is achieved. The simulated spectrum with a spectral width of around

22 nm is obtained at the output (Fig. 4.5). Correspondingly, the obtained autocorrelation trace is plotted in the same figure. The autocorrelation width is $\sim$ 3.47 ps. It is evident that the experimental and simulated spectra and durations are in good agreement. The next section will discuss the compression of the pulses of this ANDi laser.

4.1.1 Compressor results

As mentioned before, the pulses obtained from the ANDi laser cavity are heavily chirped and must be compressed internally or externally to obtain the high peak power that can not be achieved with a soliton regime. The compressor we built to compress the pulse at the output of the ANDi fiber laser is based on two transmission gratings (Edmund Optics-LightSmyth grating) placed parallel to each other in a Treacy arrangement [202] (Fig. 4.6).

This parallel geometry of the gratings can be used to compensate for the second-order dispersion, i.e. group delay dispersion (GDD). The GDD value after the double passes

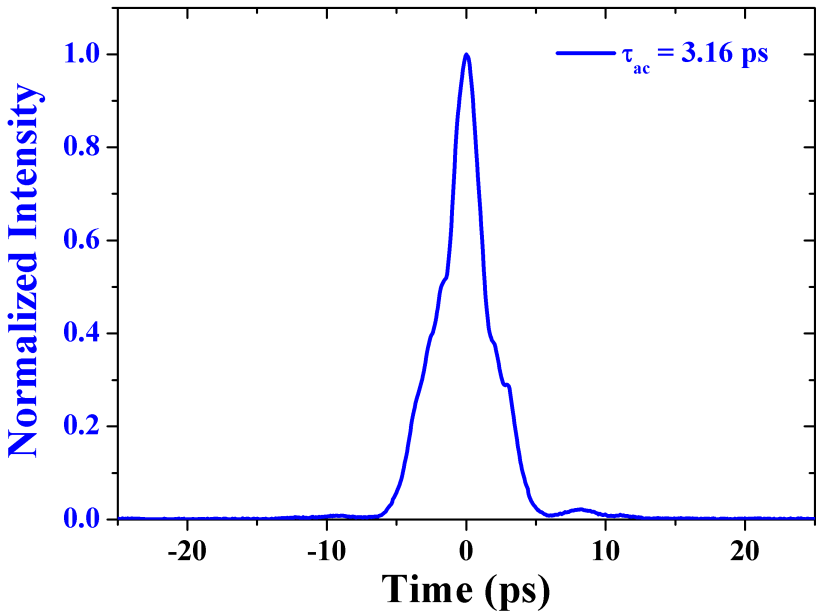

Figure 4.4: Autocorrelation trace measured at the output of the ANDi laser cavity. The autocorrelation width τ_{ac} is around 3.16 ps.

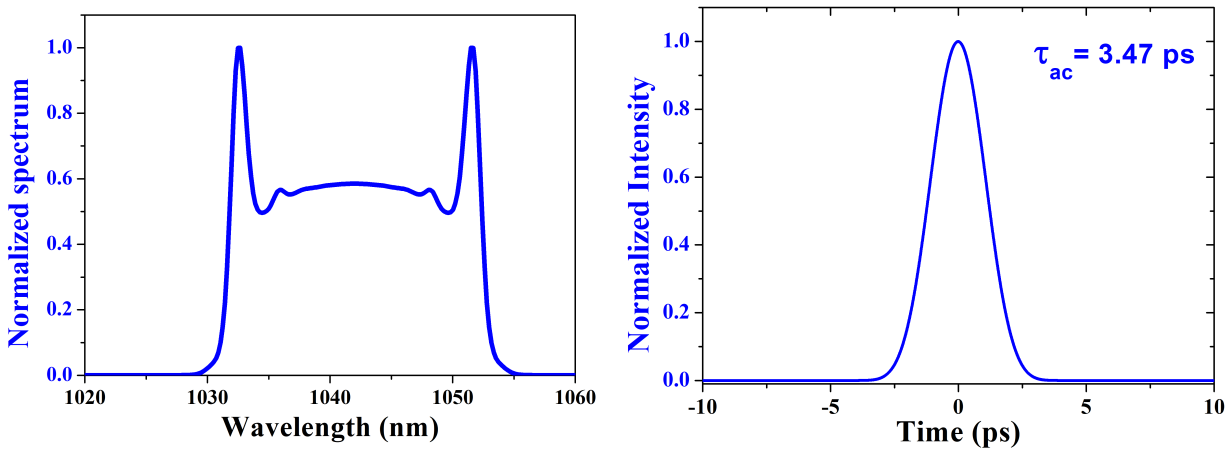

Figure 4.5: (**Left**) Simulated spectrum obtained at the output of ANDi laser. The spectral width is $\sim 22\,\text{nm}$, while the spectrum has a characteristic shape of 'cat-ear' or 'Batman'. (**Right**) The corresponding autocorrelation trace with $\tau_{ac} \sim 3.47\,\text{ps}$.

from the gratings depends on the incident angle (θ_i), order of diffraction (m), the distance between the two gratings (L_G), grating period (d), and the central wavelength (λ_0),

$$GDD = \frac{Nm^2\lambda_0^3 L_G}{2\pi c^2 d^2}\left[1+\left(m\frac{\lambda_0}{d}+\sin\theta_i\right)^2\right]^{-\frac{3}{2}}, \tag{4.1}$$

where N is the number of passes (for double pass $N = 2$), while c is the speed of light. The distance between the gratings is adjusted to compensate for the different values of GDD.

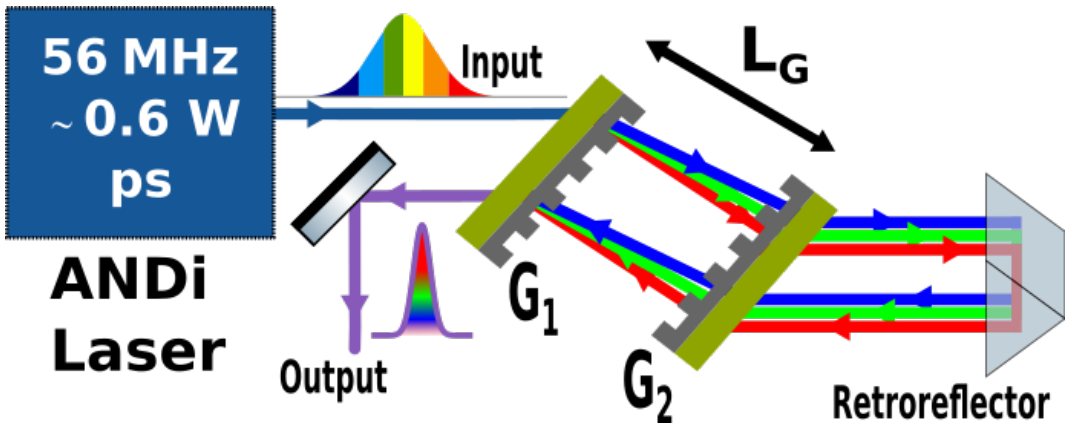

Figure 4.6: Compressor built from two parallel transmission gratings (G_1 and G_2) in Treacy arrangement.

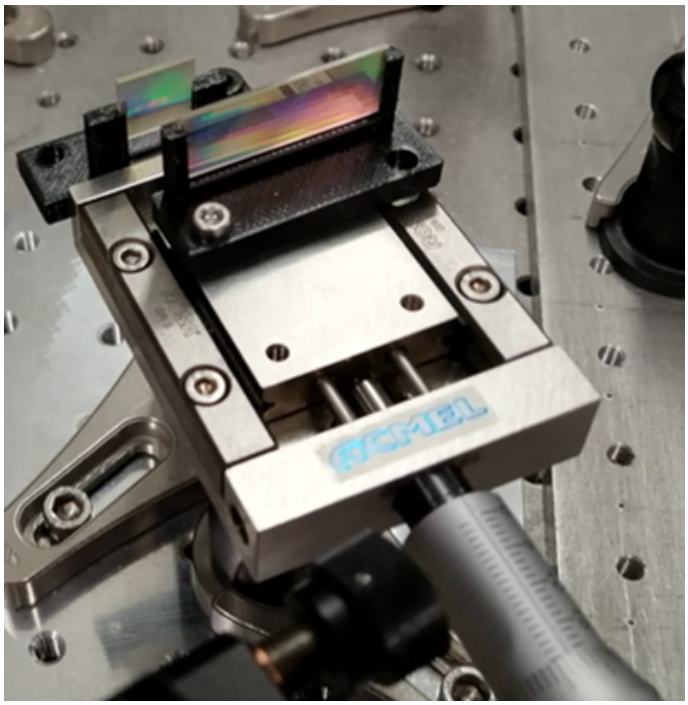

Figure 4.7: The compressor setup used in the experiment is made of two parallel transmission gratings, while the second grating is placed on the translation stage to adjust the distance between the gratings.

That is why the second grating G_2 is usually put on the translation stage as shown in Fig. 4.7. The transmission grating we used to compress the output pulse has a grating period of 1000 nm (1000 lines/mm), and the working angle of incidence is 31.3°. The following discussion calculates the GDD value from the ANDi laser that needs to be balanced to get transform-limited pulse duration. The accumulated GDD at the output of the ANDi laser while considering a Gaussian pulse is given by:

$$GDD_{ac} = \frac{\Delta\tau_0^2}{4\ln 2}\sqrt{\left(\frac{\Delta\tau}{\Delta\tau_0}\right)^2 - 1}, \tag{4.2}$$

where $\Delta\tau$ is the pulse duration obtained from the ANDi laser, while $\Delta\tau_0$ is the transform-limited pulse duration. The latter is obtained by taking the Fourier transform of the spectrum measured at the output of the ANDi laser. By taking the Fourier transform of the spectrum (shown in Fig. 4.3), the transform-limited autocorrelation width comes out

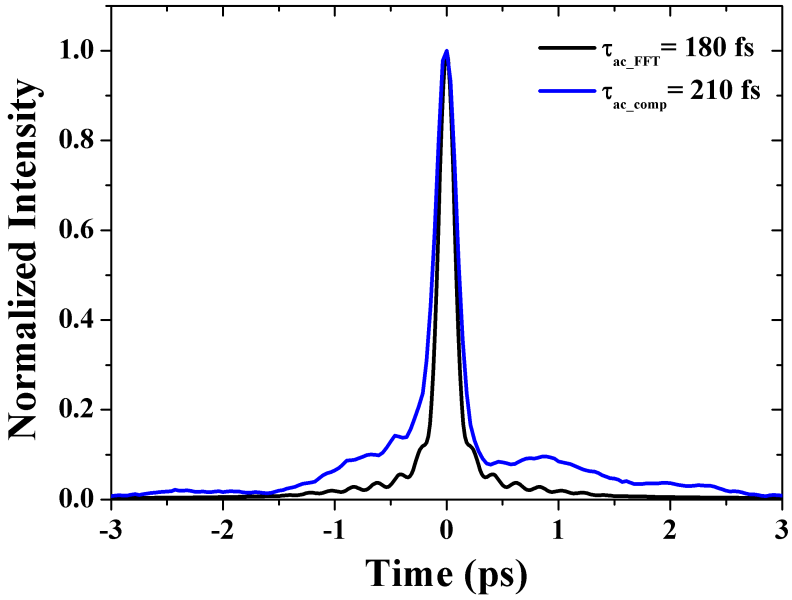

Figure 4.8: Transform limited autocorrelation trace obtained by taking Fourier transform of the spectrum shown in Fig. 4.3, and the compressed autocorrelation trace.

to be $\sim$ 180 fs (Fig. 4.8). The transform-limited pulse duration (considering a Gaussian pulse) is around 127 fs. By using the formula given in Eq. 4.2, the accumulated GDD is around 0.102 ps^2. The distance between the gratings to compensate for the mentioned GDD can be calculated using Eq. 4.1, and it turns out to be $\sim$ 1.6 cm around 1040 nm. After the compression, the autocorrelation width is around $\sim$ 210 fs (Fig. 4.8). The compressed pulse duration is about 149 fs which is almost Fourier-limited. The difference in the expected width is due to higher orders of dispersion that are not compensated by the compressor. The measured average power after the compressor was $\sim$ 480 mW, which shows almost 95 % single-pass diffraction efficiency of the grating. This corresponds to a peak power of around 57 kW.

4.2 Picosecond ANDi laser

The picosecond all-normal-dispersion (ANDi) laser oscillator is built around the large-mode-area (LMA) rod-type ytterbium-doped fiber (NKT photonics, AeroGAIN-ROD modules, Model 1.1), as shown in Fig. 4.9. The length of the fiber is 0.8 m, and it is optimized for the wavelength range between 1030 nm – 1040 nm. The rod-type fiber has a mode field diameter of 45 µm ± 4 µm and a pump-cladding diameter of 200 µm ± 10 µm at 1030 nm. The cladding absorption is ∼ 14 dB around 976 nm. The Yb-doped fiber is pumped by a 2 nm broad laser diode at 976 nm through a dichroic mirror (DMSP1000-Thorlabs) which has a high reflectivity of ∼ 99% around 1030 nm and high transmissivity of ∼ 95% around 976 nm. Pulsed operation in the laser cavity is achieved by the nonlinear polarization rotation technique. A transmission grating (TG) having a period of 575 nm (1739 lines/mm) is inserted inside the laser cavity. The TG is used to disperse the s-polarized pulse beam into its spectral components while the optimized angle of incidence (AOI) is 63.6°. The

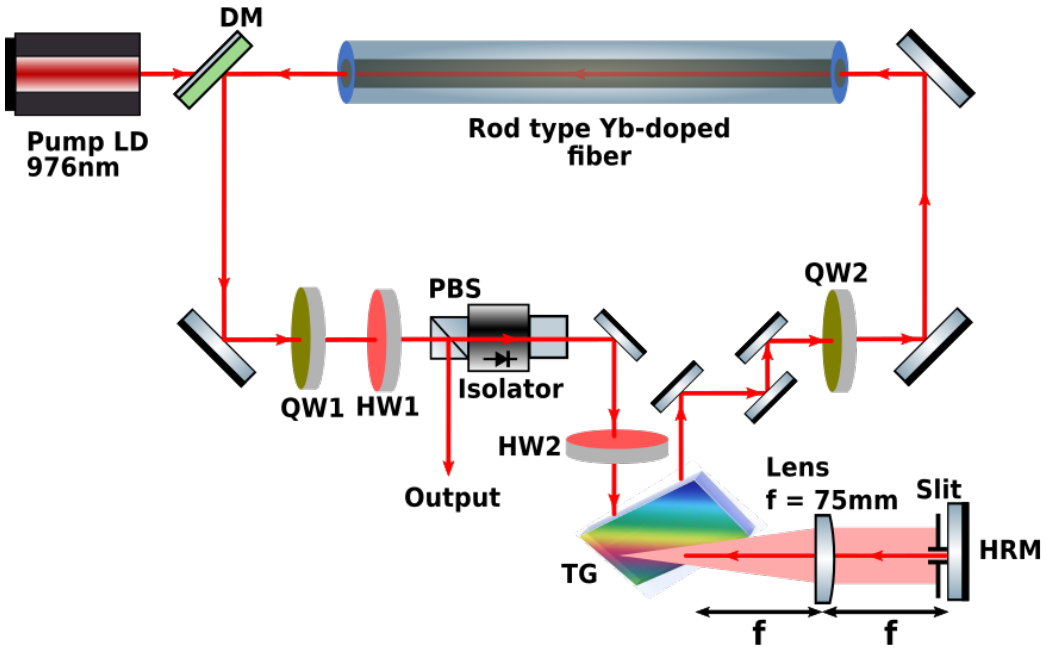

Figure 4.9: Experimental setup of the rod-type ytterbium fiber laser oscillator. DM: Dichroic mirror, TG: Transmission grating.

single-pass efficiency of this grating was observed to be around 97%. The spreading of the wavelengths from the grating is governed by the equation

$$d \sin(\theta_m) = m\lambda \pm d \sin(\theta_i), \tag{4.3}$$

where d is the grating period, m is the order of diffraction, while θ_m and θ_i are the diffraction and incident angles, respectively. Whereas, the $\pm$ sign is used for the light propagation for transmission (+) or reflection grating (−), respectively. Based on the values of the grating period and the incident angle, the 1st order diffracted angles are from -61.4° to -71.4° for 1020 nm to 1060 nm, respectively. With a lens having a focal length of 75 mm, the dispersed light is collimated and imaged onto a high reflecting mirror (HRM). The reflected light from the HRM is sent back through the transmission grating and propagates through the ring laser cavity.

The output pulses are detected with a 2 GHz Si-based photo-detector (Thorlabs DET025-M) and analyzed using an oscilloscope (RIGOL MSO5204) while their spectra are measured using an optical spectrum analyzer (Thorlabs OSA205C). Similarly, the RF spectrum of the pulses is analyzed using an RF spectrum analyzer (Agilent Technologies N9340B). Lastly, the pulse duration is measured by a homemade intensity autocorrelator using a BBO crystal (type I phase matching at 1030 nm).

4.2.1 Picosecond ANDi laser results

In this section, the results obtained from our laser setup are discussed. The pump threshold power of our fiber laser is $\sim$ 17 W. Above this pump power, we improved the output power by rotating the waveplates. A slope efficiency of around 47 % was achieved for the CW output. Mode-locking is achieved with about 65 W of pump power. To ensure a stable mode-locking regime, the waveplates are optimized. Their optimized angles are QW1 = 141°, QW2 = 129°, and HW1 = 99°, respectively. The oscilloscope trace and the RF

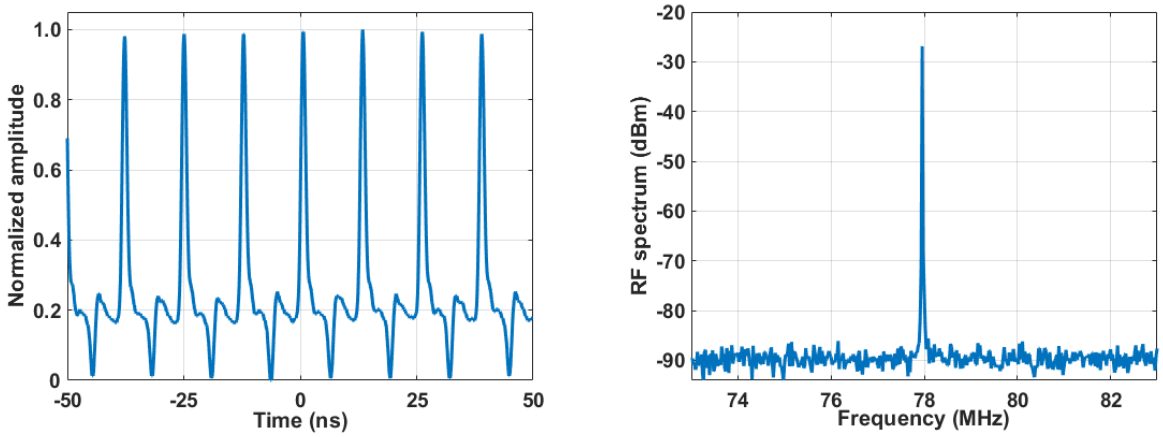

Figure 4.10: (**Left**) Oscilloscope trace of the laser pulses. (**Right**) The RF spectrum (SNP $\sim 65\,\mathrm{dB\,m}$), at a resolution bandwidth (RBW) of 1 kHz, shows the fundamental repetition rate around $\sim 78\,\mathrm{MHz}$.

spectrum (recorded with a resolution bandwidth of 1 kHz) of the output pulse centered at 1030 nm are plotted in Fig. 4.10. The fundamental repetition rate is close to 78 MHz and the signal-to-noise peak (SNP) is about $\sim 65\,\mathrm{dB}$ indicating a stable pulse mode-locking.

The pulse beam profile and the data points to measure the M^2 are plotted in Fig. 4.11, leading to $M^2 \leq 1.3$.

In order to continuously adjust the spectral width and the central wavelength of the

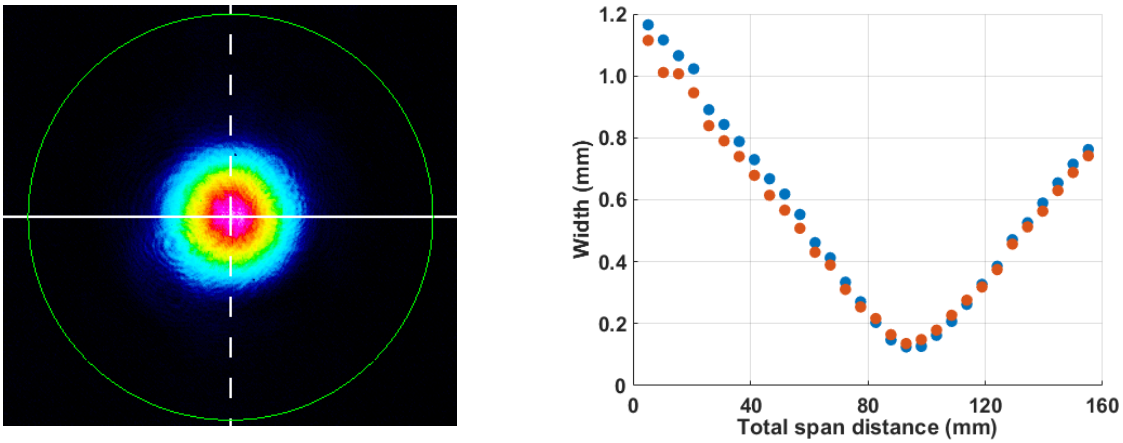

Figure 4.11: (**Left**) Beam profile at the output of the Yb rod-type fiber laser cavity (**Right**) Data points to measure the M^2 of the beam, which comes out to be ~ 1.24.

generated pulses, we made sure that the laser is robustly self-mode-locking. This is accomplished by precisely adjusting the distance from the TG to the lens, and from the lens to the HRM. Hence, both the lens and the HRM are mounted on precision translation stages to keep the distances between the TG to the lens and from the lens to the HRM almost equal to the focal length of the lens. Even if the slit is placed almost against the HRM, still it is not exactly in the focal plane of the lens. This implies that the slit is not sharply filtering the spectrum of the laser pulse. This is why, in the simulations presented afterward, we will consider the slit acts as a super-Gaussian filter of low order.

4.2.1.1 Spectral width tunability

The spectral width of the output pulses is continuously adjusted by changing the size of the slit. For this set of experiments, the slit size is varied from 0.26 mm to 0.70 mm around the central wavelength of 1030 nm. Accordingly, the spectral width (full-width at half maximum (FWHM) $\Delta\lambda$) of the output pulses is tuned from $\sim$ 0.38 nm to $\sim$ 2.24 nm as shown in Fig. 4.12.

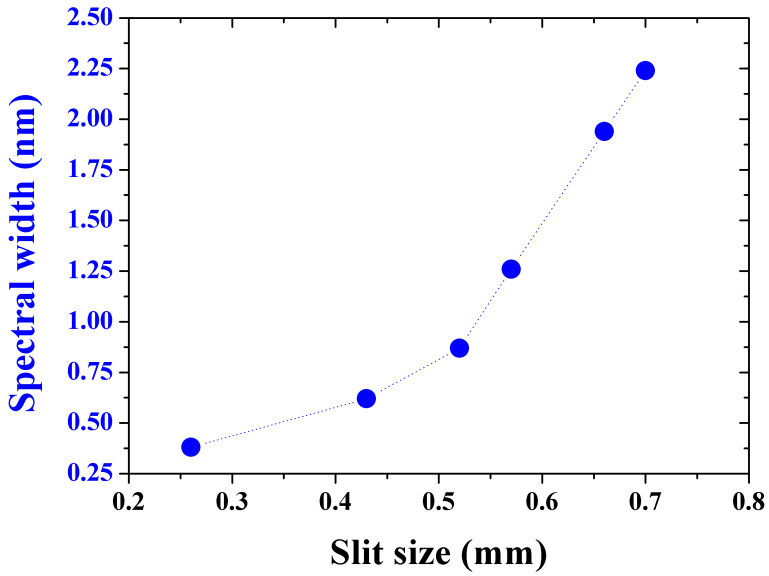

Figure 4.12: Variation of the spectral width of the pulses according to the slit size.

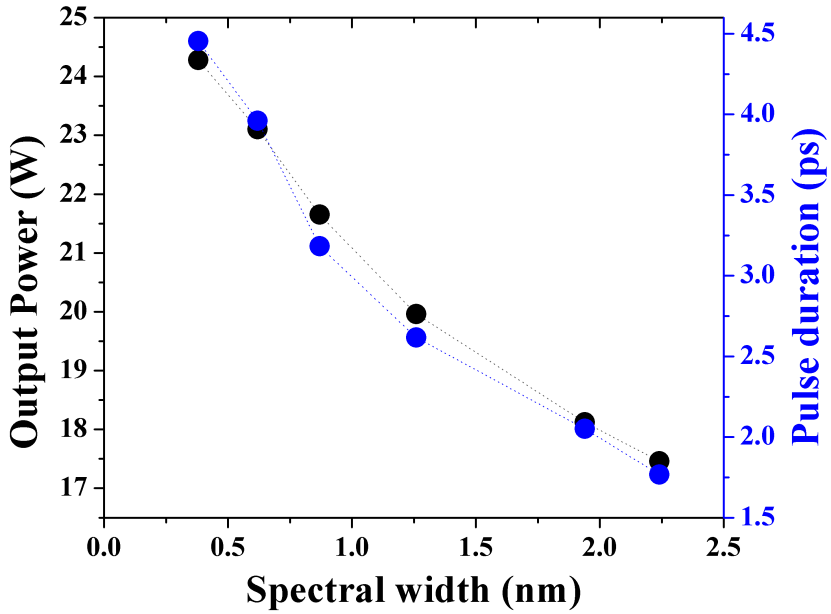

Figure 4.13: Evolution of the average output power and pulse duration versus the spectral width of the generated pulse.

Figure 4.13 displays the evolution of the output average power and the pulse duration when the spectral width of the output pulses is varied for the pump power of 78 W. The output average power is reduced from $\sim$ 24.3 W to $\sim$ 17.6 W as the slit size is increased. Likewise, the pulse duration is also decreased from $\sim$ 4.5 ps to $\sim$ 1.8 ps. The pulse duration is calculated from the autocorrelation traces plotted in Fig. 4.14, considering the Gaussian pulses. The reduction of the pulse duration at half-width is concomitant with the broadening of the pulse spectral width (shown in Fig. 4.12). The corresponding output pulse spectra along with their FWHM spectral widths are shown in Fig. 4.15. Additionally, sharp peaks are observed at the edges of the spectrum when the spectrum gets broader ($\Delta\lambda$ = 1.94 nm and 2.24 nm) as a result of the increase of SPM [6]. Even if the pulse spectral profiles are structured for the broader spectra, the FWHM spectral widths and the root mean square spectral widths deviate from each other by less than 3%. The autocorrelation FWHM is 6.3 ± 0.1 ps for the spectrum having $\Delta\lambda \sim 0.38$ nm. The autocorrelation width is decreased as the spectral width of the output pulses is increased and it goes down to

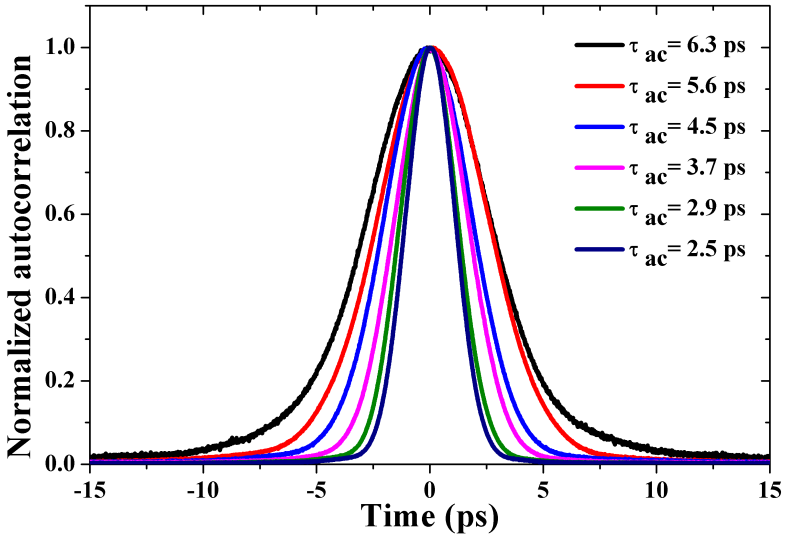

Figure 4.14: Autocorrelation traces recorded using intensity autocorrelator corresponding to the spectra plotted in Fig. 4.15. The autocorrelation FWHM decreases from the $\tau_{ac} = 6.3 \pm 0.1$ ps (corresponds to the spectral width of ~ 0.38 nm) down to $\tau_{ac} = 2.5 \pm 0.1$ ps (corresponds to the spectral width of ~ 2.24 nm).

2.5 ± 0.1 ps. Considering a Gaussian pulse, this indicates the pulse duration $\Delta\tau$ decreasing from ~ 4.5 ps to ~ 1.8 ps. The reduction of the pulse duration is accompanied by a decrease of the average output power from $P_{out} \sim 24.3$ W to $P_{out} \sim 17.6$ W (Fig. 4.13). The reduction of the average power recorded while enlarging the slit width is likely due to SPM. As the SPM increases, the pulse spectrum broadens and experiences more losses during its transmission through the slit. The pulse energy E_p and the peak power of the output pulses can be estimated through

$$P_p \approx \frac{P_{avg}}{R_R \Delta\tau} = \frac{E_p}{\Delta\tau}, \tag{4.4}$$

where P_p and P_{avg} are the peak and average power, respectively, while R_R is the fundamental repetition rate. Using the above equation, the pulse energy ($E_p = \frac{P_{avg}}{R_R}$) reduces from ~ 312 nJ to $E_p \sim 224$ nJ. However, while the pulse energy decreases, the pulse peak power increases from $P_p \sim 70$ kW to $P_p \sim 127$ kW, due to the reduced pulse duration for broader spectra, and it has a dominant effect on the peak power compared to the aver-

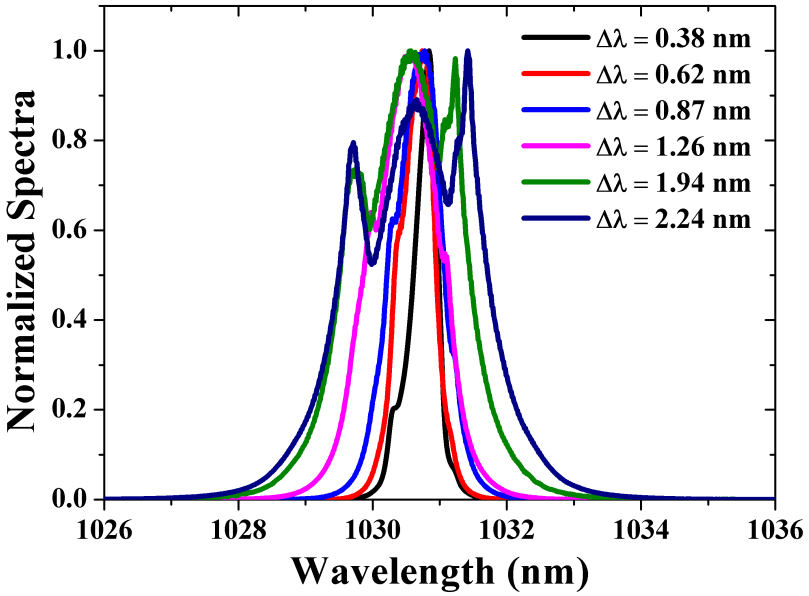

Figure 4.15: Evolution of the output pulse spectra while changing the slit width. The FWHM spectral width is varied from $\sim$ 0.38 nm to $\sim$ 2.24 nm. The pulses with broader spectral widths have sharp edges coming from the effect of the SPM.

age power. This increase in the peak power ultimately modifies the self-phase modulation (SPM) experienced by the laser pulse during its propagation in the ytterbium fiber and broadens its output pulse spectrum. Based on the data in Fig. 4.14 and Fig. 4.15, we computed the half-width time-bandwidth product (HWTBP) which is plotted in Fig. 4.16. It shows an increasing trend with the increase in spectral width. The HWTBP increased from 0.48 to 1.12, which shows that the duration of the pulses is not that far away from Fourier-limited pulse duration. Considering the envelope of the pulse is Gaussian in shape, the chirp parameter of the chirped pulse is computed as ($\Delta\tau_p = \Delta\tau_p^0\sqrt{1+C^2}$), where ($\Delta\tau_p$) and ($\Delta\tau_p^0$) are the pulse duration of the chirped and unchirped pulses, respectively. The latter is computed by taking the Fourier transform of the pulse spectra. The chirp parameter (C) increases from $\sim$ 0.43 to $\sim$ 2.35 as the width of the slit is enlarged. All the experimental results related to the spectral width tunability are summarized in Table 4.1.

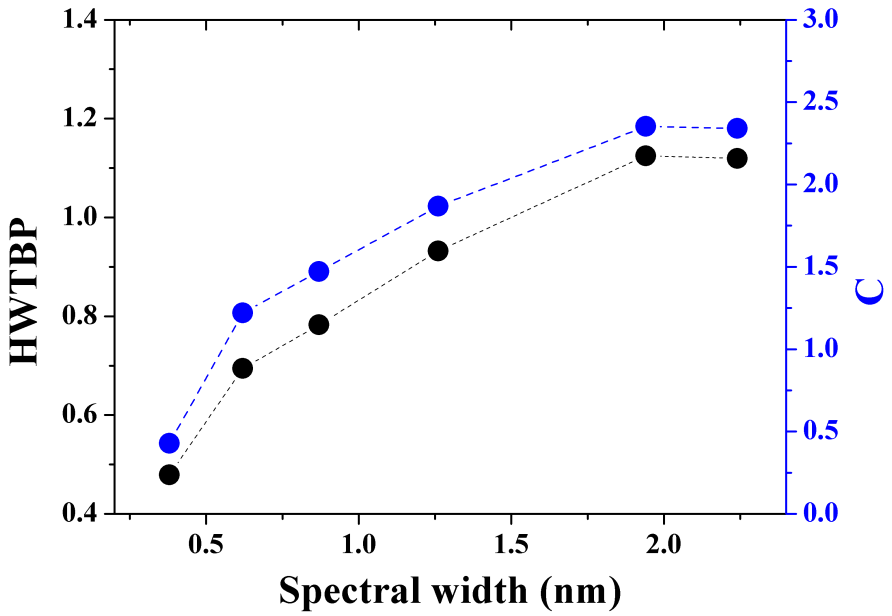

Figure 4.16: Evolution of the half-width time-bandwidth product (HWTBP) and the chirp parameter (C) versus the pulse spectral width.

Slit size (mm)	Spectral width (nm)	Autoco--width τ_{ac} (ps)	Pulse duration (ps)	Average power (W)	Peak power (kW)	Pulse energy (nJ)	HWTBP	C
0.26	0.38	6.3	4.46	24.28	69.83	311.48	0.48	0.43
0.43	0.62	5.6	3.96	23.10	74.83	296.34	0.69	1.22
0.52	0.87	4.5	3.18	21.65	87.34	277.74	0.78	1.47
0.57	1.26	3.7	2.62	19.96	97.73	256.06	0.93	1.86
0.66	1.94	2.9	2.05	18.12	113.40	232.46	1.12	2.35
0.70	2.24	2.5	1.77	17.46	126.56	223.99	1.12	2.34

Table 4.1: All the experimental data related to spectral width tunability. The spectral widths, autocorrelation widths, and pulse duration are considered at FWHM. HWTBP: Half-width time-bandwidth product, C: Chirp parameter.

4.2.1.2 Central wavelength tunability

The central wavelength of the generated pulses can also be changed, while ensuring the fiber laser is self-mode-locked, keeping the width of the slit constant and varying its position laterally. Figure 4.17 shows the recorded spectra by varying the position of the slit for

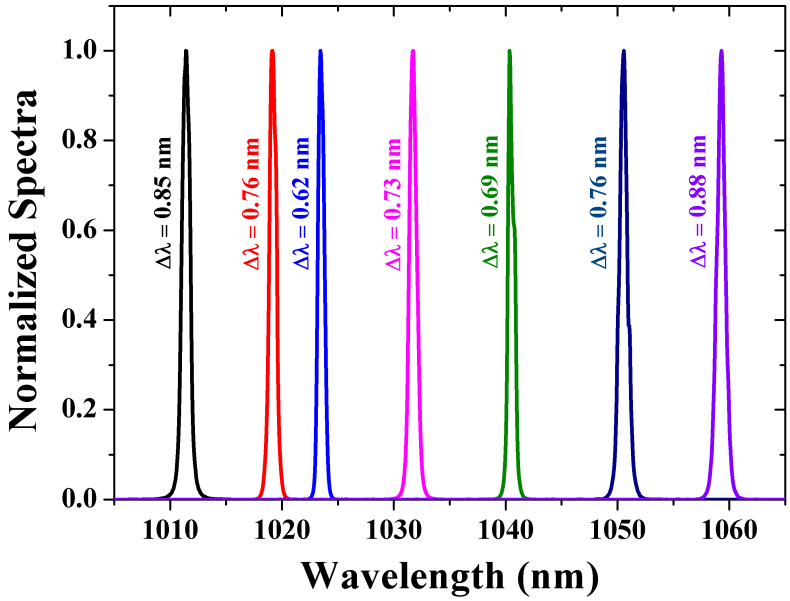

Figure 4.17: Tunability of the central wavelength achieved while keeping constant the slit width. The spectra at different wavelengths are plotted along with their spectral widths.

a pump power of 81 W, demonstrating a 50 nm tunability over the 1010 nm to 1060 nm spectral range. The minimum spectral width of 0.62 nm is recorded at 1024 nm and the maximum spectral width of 0.88 nm is recorded at 1059 nm, respectively.

The autocorrelation traces of the generated pulses are displayed in Fig. 4.18. The maximum and minimum durations of the autocorrelation at half-width $\tau_{ac}^{max} = 7.0 \pm 0.1$ ps and $\tau_{ac}^{min} = 3.8 \pm 0.1$ ps are recorded at 1024 nm and 1051 nm, respectively. According to the data displayed in Fig. 4.17 and Fig. 4.18, the half-width time-bandwidth product (HWTBP) is calculated and plotted in Fig. 4.19. The HWTBP is almost constant and around 0.90 for all spectra except for the spectrum at 1051 nm where the HWTBP is 0.55. The average output power for these spectra is also shown in the same figure. Its evolution is bell-shaped and it is in good agreement with the emission cross-section of ytterbium-doped optical fiber as shown in Fig. 1.5. A maximum of ~ 25 W of average power is achieved at ~ 1040 nm. Towards the edges (i.e., at 1010 nm and 1060 nm) the output average power is

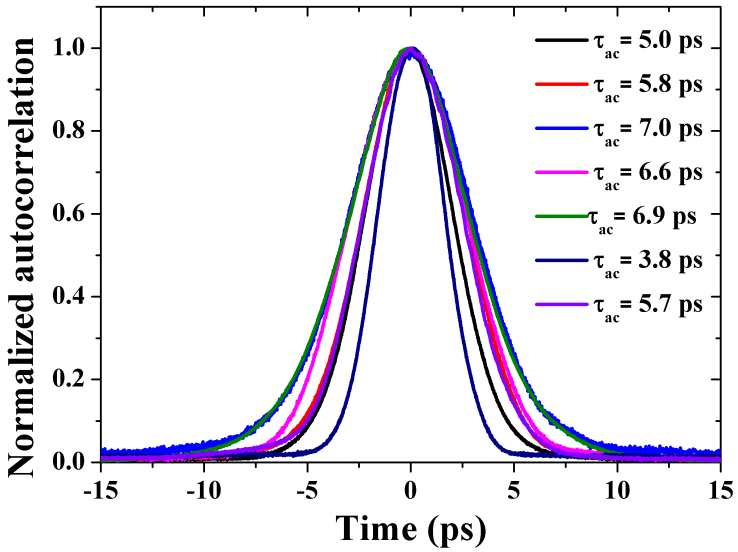

Figure 4.18: Autocorrelation traces measured at different wavelengths ranging from 1010 nm to 1060 nm.

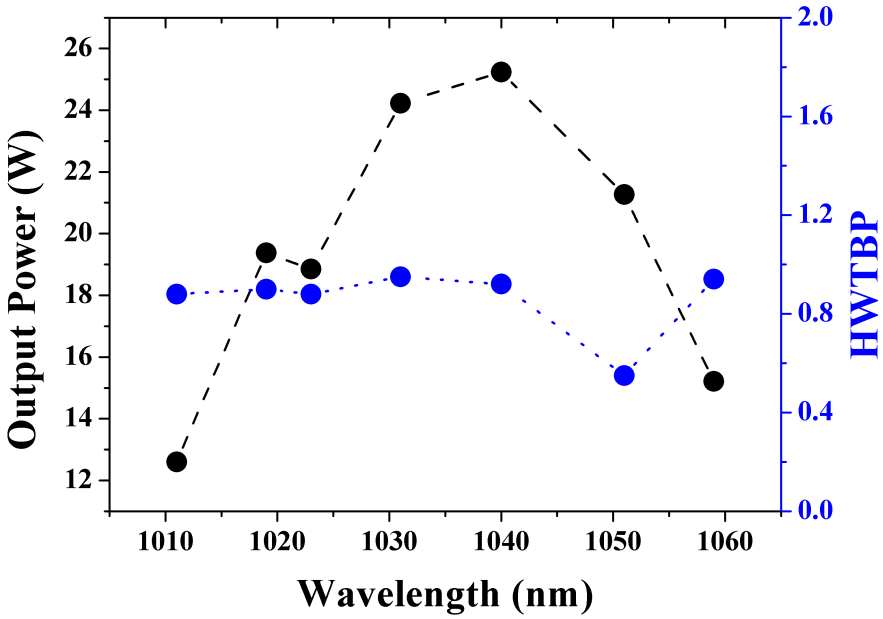

Figure 4.19: Average output power and half-width time-bandwidth product (HWTBP) plotted against the central wavelength.

decreased to $\sim 13\,\mathrm{W}$, and $\sim 15\,\mathrm{W}$, respectively. Based on the average power and the pulse duration, the minimum and maximum peak power, achieved at 1010 nm and 1051 nm, are $\sim 46\,\mathrm{kW}$ and $\sim 101\,\mathrm{kW}$, respectively. The data relating to central wavelength tunability is summarized in Table 4.2.

Central Wavelength **(nm)**	Spectral width **(nm)**	Autoco--width τ_{ac} **(ps)**	Pulse duration **(ps)**	Average power **(W)**	Peak power **(kW)**	Pulse energy **(nJ)**	HWTBP
1011.5	0.85	5.0	3.54	12.60	45.72	161.64	0.88
1019.1	0.76	5.8	4.10	19.37	60.59	248.49	0.90
1023.4	0.62	7.0	4.95	18.85	48.86	241.82	0.88
1031.7	0.73	6.6	4.67	24.23	66.61	310.84	0.95
1040.3	0.69	6.9	4.88	25.24	66.37	323.80	0.92
1050.6	0.76	3.8	2.69	21.26	101.50	272.74	0.55
1059.3	0.88	5.7	4.03	15.21	48.41	195.13	0.94

Table 4.2: All the experimental data related to central wavelength tunability. The spectral widths, autocorrelation widths, and pulse duration are considered at FWHM. HWTBP: Half-width time-bandwidth product.

4.2.2 Numerical simulations

To account for the above-reported behaviors of our ANDi fiber laser, we run a numerical model previously reported in [186]. The computations were performed using Julia programming, considering the laser is built around a 0.8 m long, single-mode ytterbium-doped fiber having mode field diameter $d_0 = 50\,\mu\mathrm{m}$. The pulse is then freely propagated in the air for a length of 2.67 m before being sent through a saturable absorber (SA) that mimics the role of the NPR in combination with the NLOP. The output mirror of the laser is set just after the SA with a 70% coupling ratio. Before being amplified again in the fiber, the pulse is transmitted through a super-Gaussian filter of order $n = 3$. This filter accounts for the role of the slit slightly displaced from the focal plane of the folded-4f dispersion line. As we already mentioned, in the presentation of the setup, this implies the slit is not sharply filtering the spectrum of the pulses. The propagation of the laser pulse within the am-

plifying fiber is simulated by solving the nonlinear Schrödinger equation (Eq. 2.34). The numerical model is solved with a standard split-step algorithm and the initial field is white noise. We run our simulations considering $\beta_2 = 230\,\mathrm{fs}^2/\mathrm{cm}$, $n_2 = 2.19 \times 10^{-20}\,\mathrm{m}^2/\mathrm{W}$, $g_0 = 3.45\,\mathrm{m}^{-1}$, $E_{sat} = 110\,\mathrm{nJ}$, $q_0 = 0.55$ and $P_{sat} = 7\,\mathrm{kW}$. The simulated arrangement matched the experimental setup except for the SA. Indeed, in the experiment, the NLOP takes the role of the SA. But the NLOP has a sinusoidal transfer function whereas the SA has a monotonically increasing transfer function. Therefore, in the experiment, the output coupling depends on the NLOP parameters while it is assumed to be constant in the simulations. Despite these differences, numerical simulations are able to retrieve the experimental trends.

4.2.2.1 Spectral width tunability

To run these simulations, we adjusted the filter bandwidth (FBW) of the super-Gaussian filter from 0.23 nm to 1.2 nm. The achieved spectral width at the output of the laser cavity corresponding to filter bandwidth ranges from 0.27 nm to 2.35 nm.

The evolutions of the output average power and the pulse duration versus the spectral width are plotted in Fig. 4.20. At constant gain saturation energy E_{sat}, as we increase the spectral width corresponding to an increase in FBW, the output power P_{out} and pulse duration τ_p decrease from 28.2 W to 13.3 W and from 12.9 ps to 2.2 ps, respectively. It is worth noticing that as the width of the spectral filter increases, while the energy of the pulse decreases from $\sim 362\,\mathrm{nJ}$ to $\sim 170\,\mathrm{nJ}$ (Fig. 4.21) because of decrease in output average power, the pulse peak power increases from $\sim 28\,\mathrm{kW}$ to $\sim 77\,\mathrm{kW}$. Accordingly, the nonlinear phase shift, experienced by the pulse during its propagation in the amplifying fiber, increases from 0.50π to 1.07π (Fig. 4.21).

We have also evaluated the HWTBP and chirp parameter (C) plotted in (Fig. 4.22) which increases from $\sim$ 0.98 to $\sim$ 1.45 and from $\sim$ 2.0 to $\sim$ 3.2, respectively, as the width of the slit is enlarged. Because of the increase in the nonlinear phase shift, self-

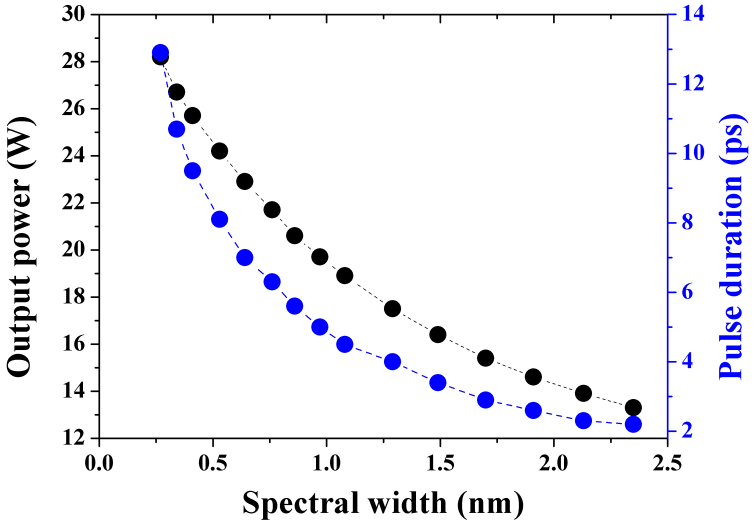

Figure 4.20: Average output power and pulse duration versus the spectral width of the super-Gaussian filter.

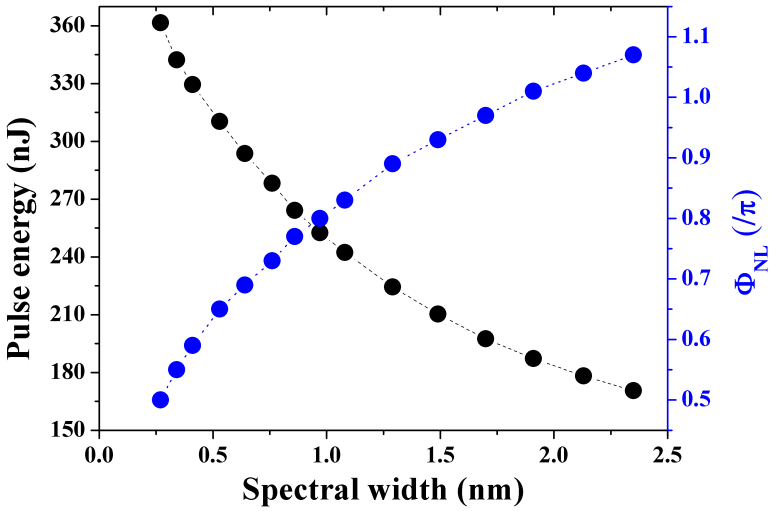

Figure 4.21: Pulse energy and nonlinear phase shift Φ_{NL} plotted against the spectral width of the output pulses.

phase modulation increases, and the edges of the pulse spectra grow substantially with a pronounced dip in the center (Fig. 4.23). In good agreement with the experimental data (Fig. 4.15), the half-width bandwidth ($\Delta\lambda$) of the pulse spectrum also increases from

0.27 nm to 2.35 nm. The autocorrelation traces corresponding to the pulse spectra are also graphed in Fig. 4.23.

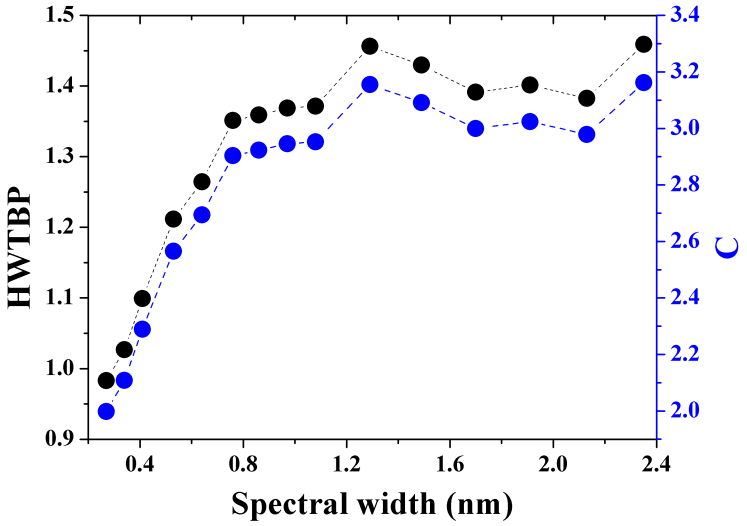

Figure 4.22: Evolution of the half-width time-bandwidth product and the chirp parameter C of the output pulses versus the spectral width of the output pulses.

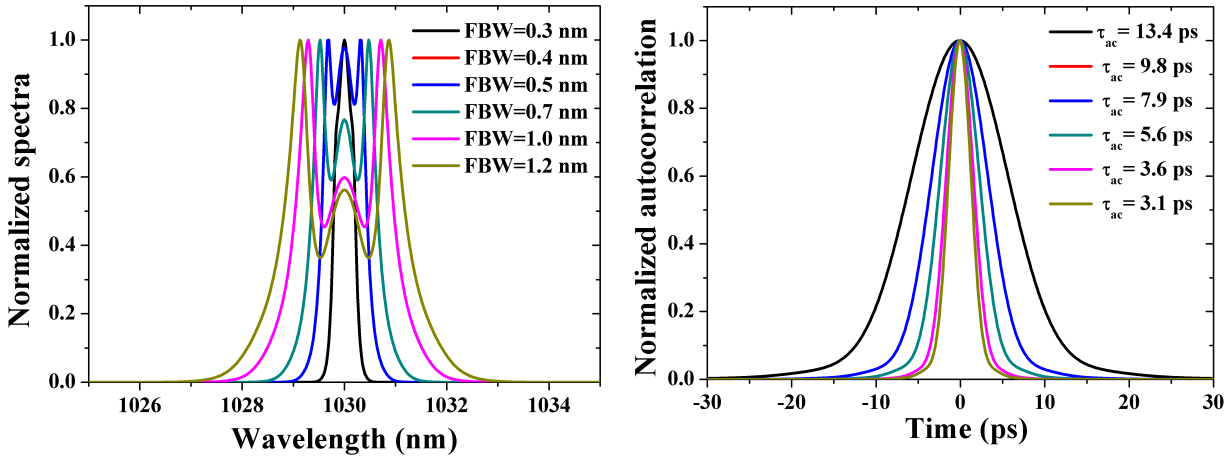

Figure 4.23: (**Left**) Evolution of the output pulse spectra while changing the slit width numerically. The FWHM spectral width is varied from $\sim$ 0.27 nm to $\sim$ 2.35 nm corresponding to filter bandwidths ranging from 0.3 nm to 1.2 nm. The pulses with broader spectral widths have sharp edges coming from the effect of the SPM. (**Right**) Autocorrelation traces corresponding to the output pulse spectra. The autocorrelation FWHM decreases from $\tau_{ac} = 13.4$ ps (corresponding to the spectral width of $\sim$ 0.27 nm) down to $\tau_{ac} = 3.1$ ps (corresponding to the spectral width of $\sim$ 2.35 nm).

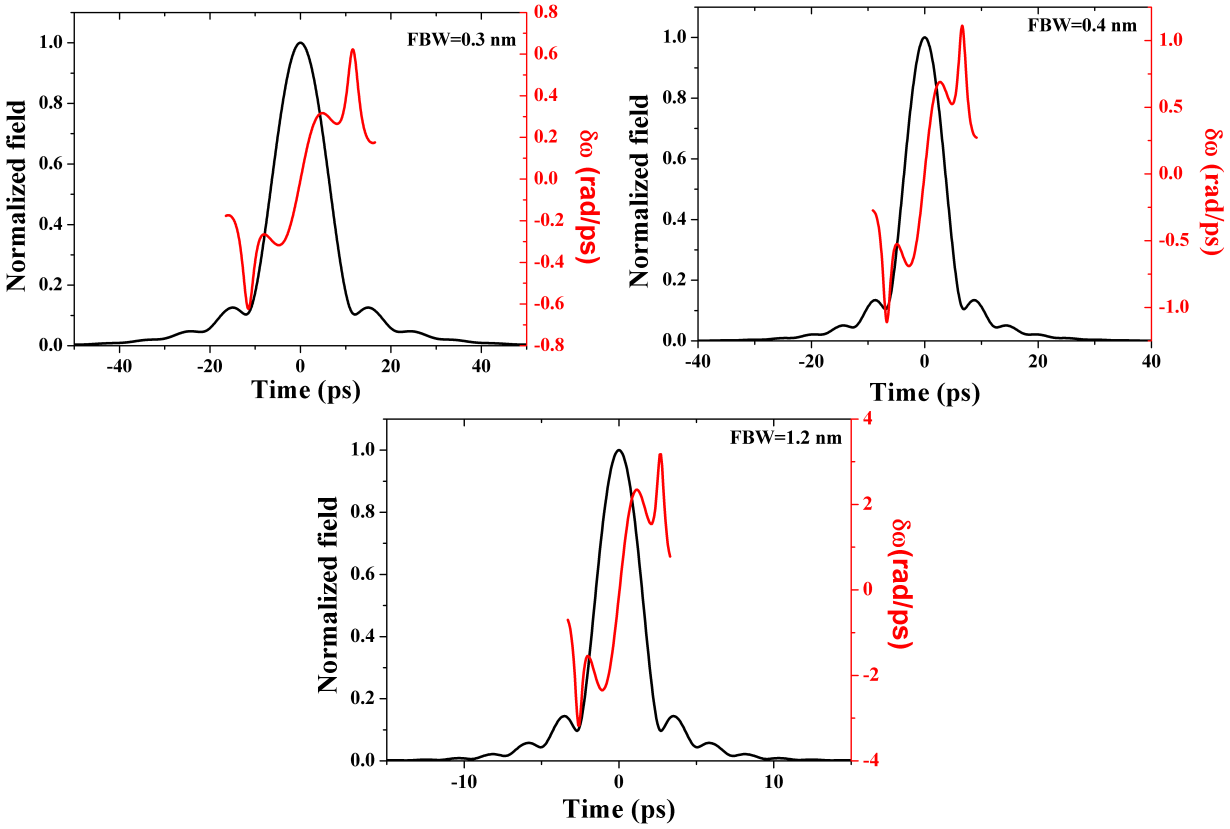

Figure 4.24: Normalized field envelope and frequency chirp ($\delta\omega$) for FBW of 0.3 nm, 0.4 nm, and 1.2 nm, respectively.

In Fig. 4.24, we have also plotted the normalized field envelope and the frequency chirp ($\delta\omega$) at filter bandwidth of 0.3 nm, 0.4 nm, and 1.2 nm, respectively. The pulse envelope exhibits oscillations that last for about twice the pulse duration. The frequency chirp evolves almost linearly across the central part of the pulse but exhibits high-frequency oscillations outside. As the spectral width of the super-Gaussian filter increases, the pulse duration at half-width decreases whereas $\delta\omega$ increases. The linear frequency chirp can be compensated outside the laser cavity when needed.

4.2.2.2 Central wavelength tunability

We have also simulated the evolution of the generated pulses for a given pump power considering a super-Gaussian filter of order n=3 having a width of 0.5 nm while tuning

its central frequency. To account for the evolution of the gain within the fiber versus the central wavelength of the super-Gaussian filter, the amplitude of the small signal gain g_0 was adjusted according to the evolution of the emission cross section of ytterbium [33]. The unsaturated gain $g_0(\lambda)$ at a given wavelength was computed considering $g_0(\lambda) = 3.45 \cdot \sigma(\lambda)/\sigma(\lambda = 1030\,\text{nm})$ where $\sigma(\lambda)$ is the emission cross section of ytterbium at the wavelength λ. To account for the increase of the pump power from 78 W to 81 W used to record the experimental data displayed in Table 4.2, we increased E_{sat} from 110 nJ to 120 nJ in the simulations. The other numerical parameters are the same. The pulse spectrum with their corresponding spectral widths at the different central wavelengths ranging from 1010 nm to 1060 nm are plotted in Fig. 4.25. The autocorrelation traces related to the spectra at different central wavelengths are graphed in Fig. 4.26 The autocorrelation duration τ_{ac} of the generated pulses slightly changes and it increases versus the wavelength. It is about 7.6 ps and 8.8 ps at 1010 nm and 1060 nm, respectively. This corresponds to a

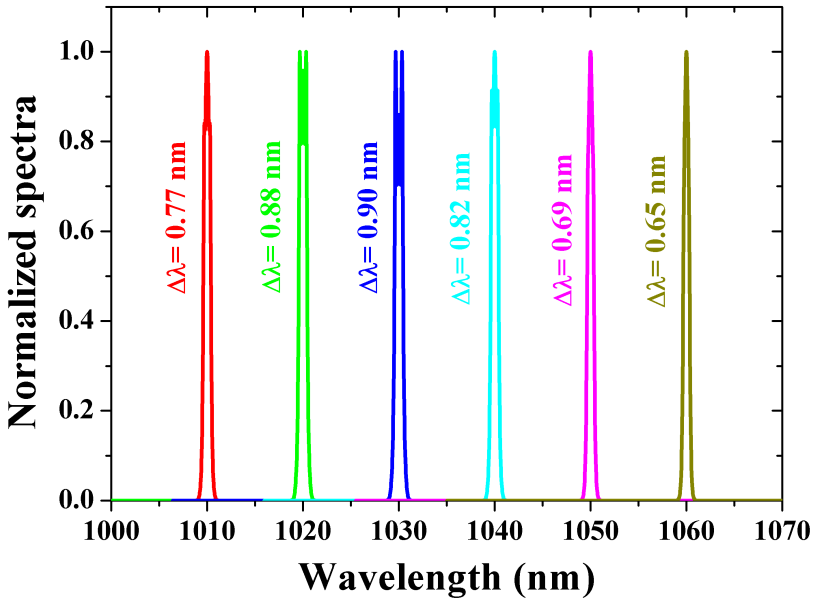

Figure 4.25: Tunability of the central wavelength achieved numerically while keeping constant the slit width. The spectra at different wavelengths are plotted along with their spectral widths.

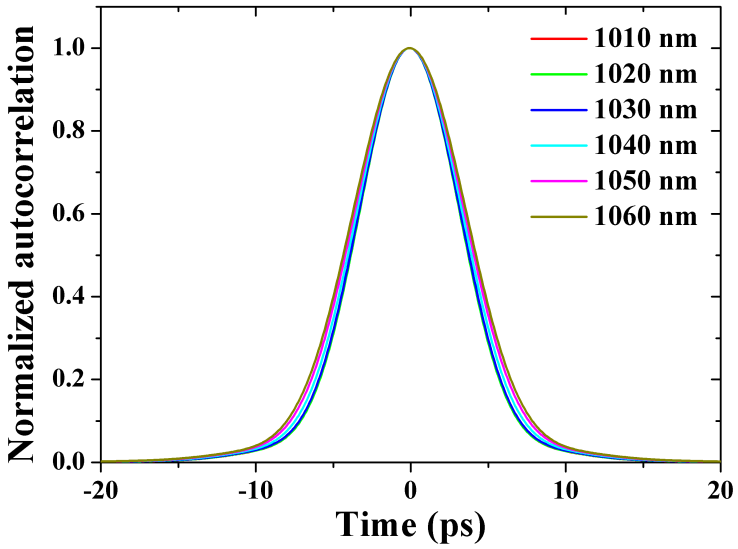

Figure 4.26: Autocorrelation traces calculated numerically at different wavelengths ranging from 1010 nm to 1060 nm.

Gaussian pulse duration ($\Delta\tau$) of 5.4 ps and 6.2 ps, respectively.

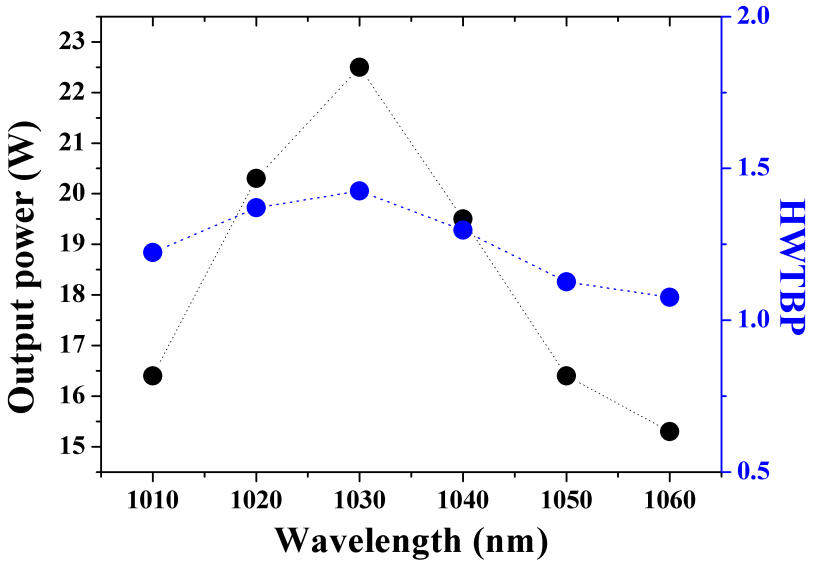

Figure 4.27: Average output power and half-width time-bandwidth product (HWTBP) obtained numerically and plotted against the central wavelength.

The output average power and the HWTBP are plotted against the tunable central wavelength in Fig. 4.27. The maximum averaged output power $P_{out} \sim 22.5\,\mathrm{W}$ is achieved around 1030 nm. Towards the edges of the scanned spectral range (i.e., at 1010 nm and 1055 nm) the output average power decreases to 16.4 W and 15.3 W, respectively. The pulse peak power P_p evolves smoothly and follows the same trend as the output power. It is $\sim$ 39 kW at 1010 nm, increases to $\sim$ 51 kW at 1030 nm, and then decreases to $\sim$ 32 kW at 1060 nm. The nonlinear phase shift Φ_{NL} experienced by the laser pulse during its propagation in the fiber evolves accordingly. It is $\Phi_{NL} \approx 0.66\pi, 0.83\pi, 0.54\pi$ at $\lambda = 1010\,\mathrm{nm}$, 1030 nm and 1060 nm, respectively. As Φ_{NL} increases, the spectra of the generated pulses exhibit more sharper peaks at their edges. The value of HWTBP slightly evolves and follows the same trend as Φ_{NL}. It is $\sim 1.22, 1.42, 1.07$ at $\lambda = 1010\,\mathrm{nm}$, 1030 nm and 1060 nm, respectively.

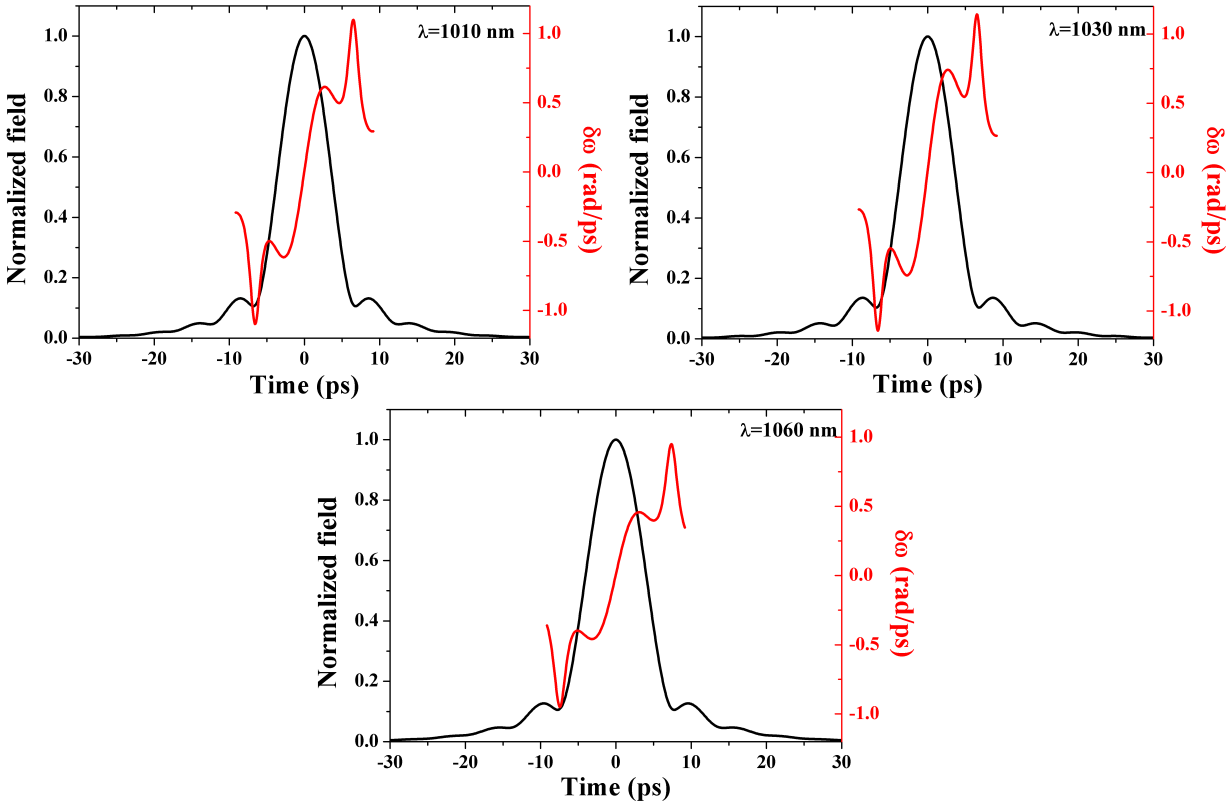

Figure 4.28: Normalized field envelope and frequency chirp ($\delta\omega$) at different central wavelengths, i.e., at 1010 nm, 1030 nm, and 1060 nm, respectively.

The normalized field envelope and $\delta\omega$ for three different central wavelengths (1010 nm, 1030 nm and 1060 nm) are also plotted in Fig. 4.28. For all the wavelengths, the envelope and the frequency chirp of the pulse are almost similar in shape. The frequency chirp slightly increases around 1030 nm where the nonlinear phase shift is higher.

4.3 Pulse evolution in Gaussian and super-Gaussian filters

ANDi pulse output parameters vary according to the spectral filtering, especially on the shape of the filter used in the laser cavity. In this section, simulations regarding the pulse evolution using the Gaussian filter and super-Gaussian filters of order $n = 2, 3, 5$, and 10, are presented. A detailed study in the article [203] has shown the impact of spectral filtering on pulse breaking up and noise-like pulse generation in all-normal-dispersion fiber lasers. Thanks to the moderate pump power we used, such phenomena are not evinced in our simulations. For all the simulations presented in this section, the filter bandwidth (FBW) was considered to be 0.3 nm, and all other laser parameters were kept similar to the ones we have presented in the experimental results. In the experimental setup, as discussed above, the filter is not exactly placed at the focal length of the lens, hence not sharply filtering the pulses. That is why, in the above numerical simulations, a super-Gaussian filter of order $n = 3$ is used. So it is necessary to draw a comparison regarding the pulse evolution using the Gaussian and super-Gaussian filters. The transmission function of the filter is written as

$$T_F = T_m \exp\left[-\frac{1}{2}\left(\frac{\lambda - \lambda_0}{FBW}\right)^{2n}\right] \tag{4.5}$$

where n represents the order of the filter, for instance $n = 1$ represent the Gaussian-shaped filter, while $n > 1$ represent the super-Gaussian-shaped filter. T_m is the maximum

transmission of the filter while λ_0 is the central wavelength. The main difference is that the pulse spectrum after the Gaussian-shaped filter is smooth, while the spectrum after the super-Gaussian-shaped filter has more steep edges and a flat top profile. The edges become more steeper as the order of the filter is increased and the top of the pulse becomes more flatter, resembling the rectangular top shape.

In Fig. 4.29, the average power and pulse duration for the Gaussian filter and super-Gaussian filters ($n = 2, 3, 5, 10$) are presented. The output power is increased as the order of the super-Gaussian filter is increased. The maximum output power of 27.6 W is recorded for the super-Gaussian filter of order $n = 10$. The pulse duration shows a slightly decreasing trend for the higher order super-Gaussian filters, and it decreases from 10.5 ps to 9.4 ps. This decrease in the pulse duration is associated with the increase of the nonlinear phase shift (correspondingly the increase in spectral width) for higher order super-Gaussian filter (Fig. 4.30). The transmission is higher because of the steep edges of the super-Gaussian filter, and that is why the increasing trend in the spectral bandwidth was observed with the

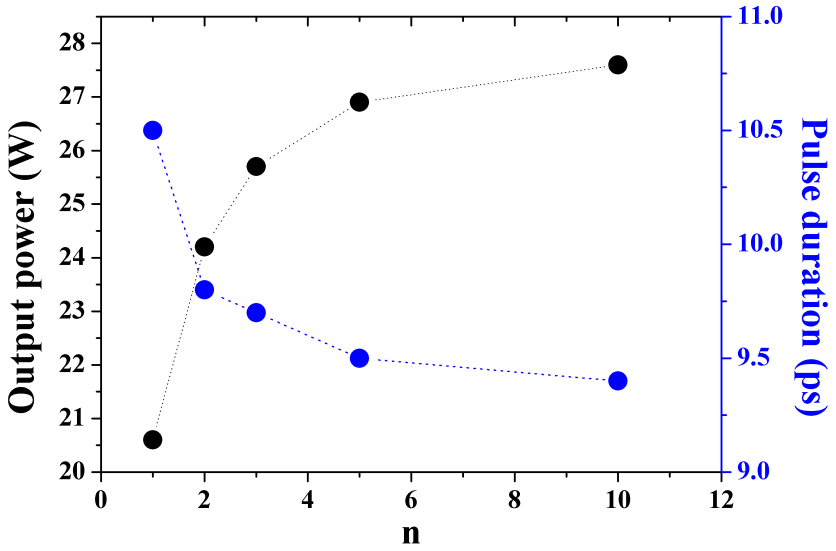

Figure 4.29: Evolution of the average power and pulse duration at the output for Gaussian filter ($n = 1$) and super-Gaussian filters ($n = 2, 3, 5, 10$), while filter bandwidth (FBW) is considered to be 0.3 nm.

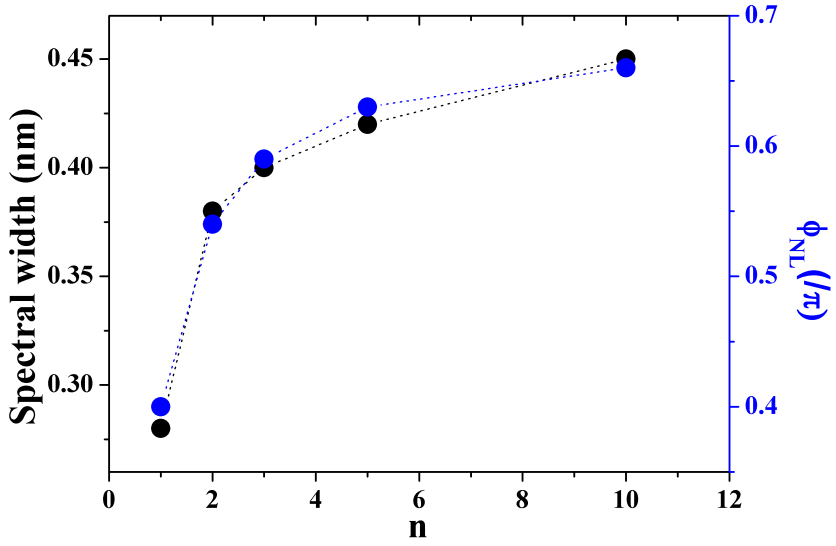

Figure 4.30: Spectral bandwidth and ϕ_{NL} for Gaussian filter ($n = 1$) and super-Gaussian filters ($n = 2, 3, 5, 10$).

increase of the order of the super-Gaussian filter. The normalized spectra around 1030 nm and the corresponding autocorrelation traces for the Gaussian and super-Gaussian filters are plotted in Fig. 4.31. The sharp peaks are visible for higher-order super-Gaussian filters.

The evolution of the pulse envelope and frequency chirp are plotted in Figs. 4.32 and

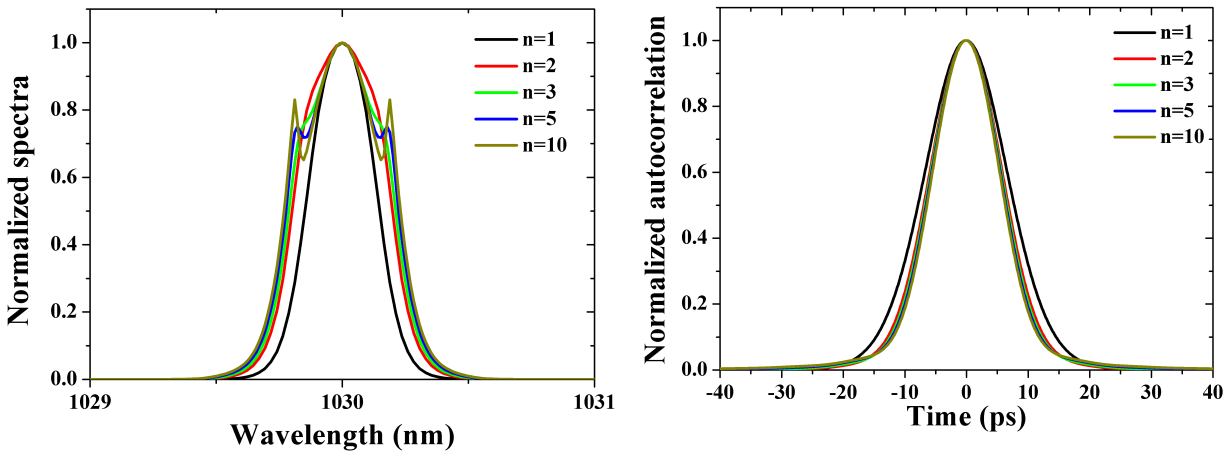

Figure 4.31: **(Left)** Normalized spectra plotted against the filter order ($n = 1, 2, 3, 5, 10$). **(Right)** Normalized autocorrelation plotted versus the filter order.

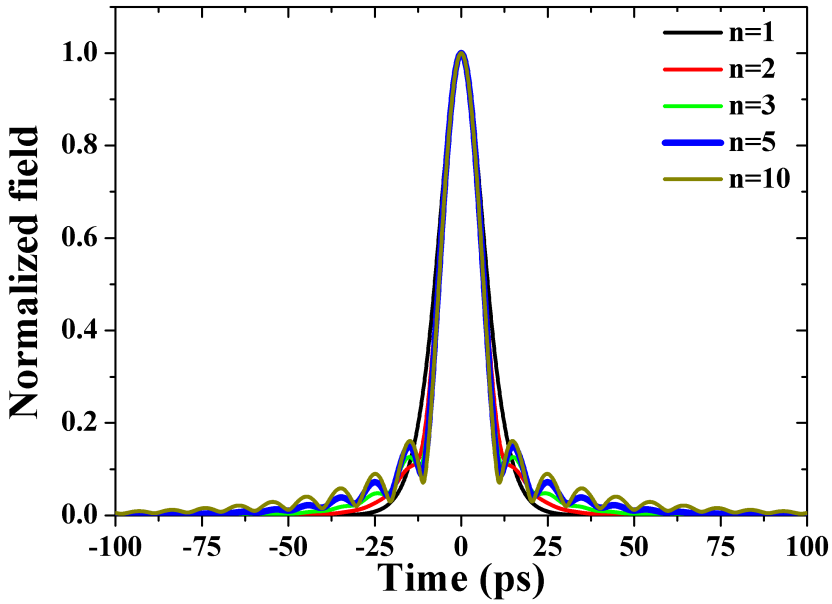

Figure 4.32: Normalized field envelope plotted for the Gaussian filter ($n = 1$) and super-Gaussian filters ($n = 2, 3, 5, 10$).

4.33, respectively. The pulse envelope exhibits oscillations for the super-Gaussian-shaped filters and the oscillations are more pronounced and last longer as the order of the filter is

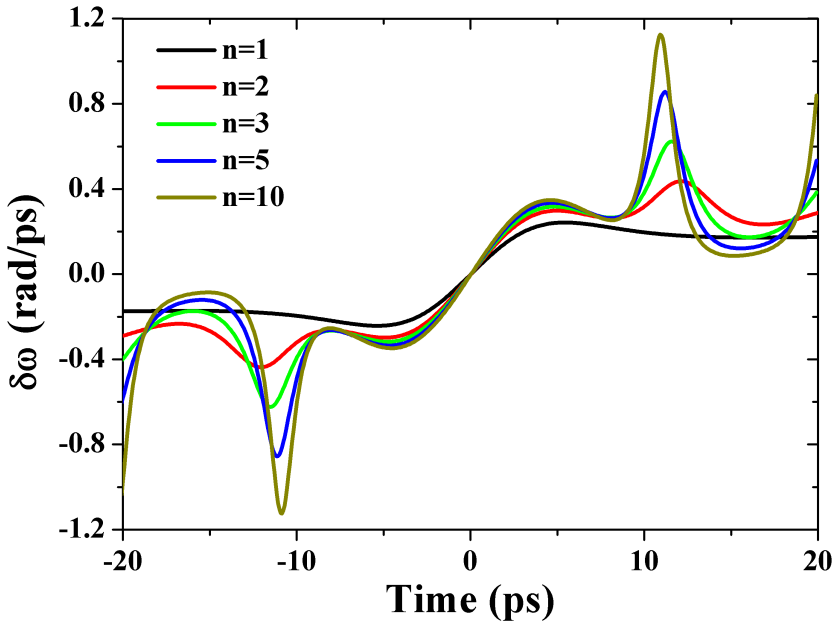

Figure 4.33: Frequency chirp $\delta\omega$ plotted for the Gaussian filter ($n = 1$) and super-Gaussian filters ($n = 2, 3, 5, 10$).

increased. It is the sharp edges of the super-Gaussian filter that induces the oscillations in the pulse envelope. Similarly, the chirp increases and exhibits high-frequency oscillations as the order of the super-Gaussian filter increases.

Overall the numerical simulations are able to retrieve the experimental behavior presented in Sect. 4.2.1. While the numerical and experimental spectra and energies of the pulses are in good agreement, the experimental HWTBP is shorter than that of the numerical ones. This can be associated with the difference in the transfer function of SA and NLOP. However, we also suspect the folded-4f dispersion line to partly compensate for the frequency chirp experienced by the laser pulse during its propagation within the laser cavity. However, based on our simulations the remaining nonlinear frequency chirp will not be compensated completely by conventional grating compressor setup.

Chapter 5

Fiber OPO setup and experimental results

Contents

This chapter will summarize the experimental setup, numerical simulations, and results associated with the fiber optical parametric oscillator (FOPO).

5.1 Experimental Setup

The fiber OPO cavity shown in Fig. 5.1 is built around photonic crystal fiber (SC-1040-5.0-PM). The PCF has a nonlinear coefficient of $11\,\mathrm{W^{-1}{\cdot}km^{-1}}$ and a mode-field diameter

of 4.3 µm ± 0.2 µm. The zero-dispersion wavelength of this fiber lies around 1040 nm ± 15 nm. The OPO cavity is pumped by a home-built tunable fiber laser (detailed discussion in chapter 4). For the OPO cavity, we have modified the tunable pump laser by inserting a reflection grating instead of the transmission grating. The grating period of the reflection grating is 610 nm while the optimized angle of incidence (AOI) is 51.4°. Secondly, we have also changed the folded-4f dispersion delay line so that the slit is now exactly at the focal length of the cylindrical lens. Due to these modifications, the fundamental repetition rate is changed to ∼ 61 MHz (Fig. 5.2). The pump wavelength is now readily tuned from 1020 nm to 1055 nm. The pump wavelength is propagated through the PCF and correspondingly signal and idler are generated. The long-pass dichroic mirror (DMLP1000-Thorlabs) has a cut-off wavelength around 1000 nm and allows the pump and idler wavelengths to be transmitted while the signal wavelength is reflected and propagated through the OPO cavity. The half-wave-plate (HW) is used before the dichroic mirror to match the polarization of the pump light with one of the PCF principal axes. The lenses, having focal lengths of 4.6 mm, are placed before and after the PCF to focus and collimate the light, respectively.

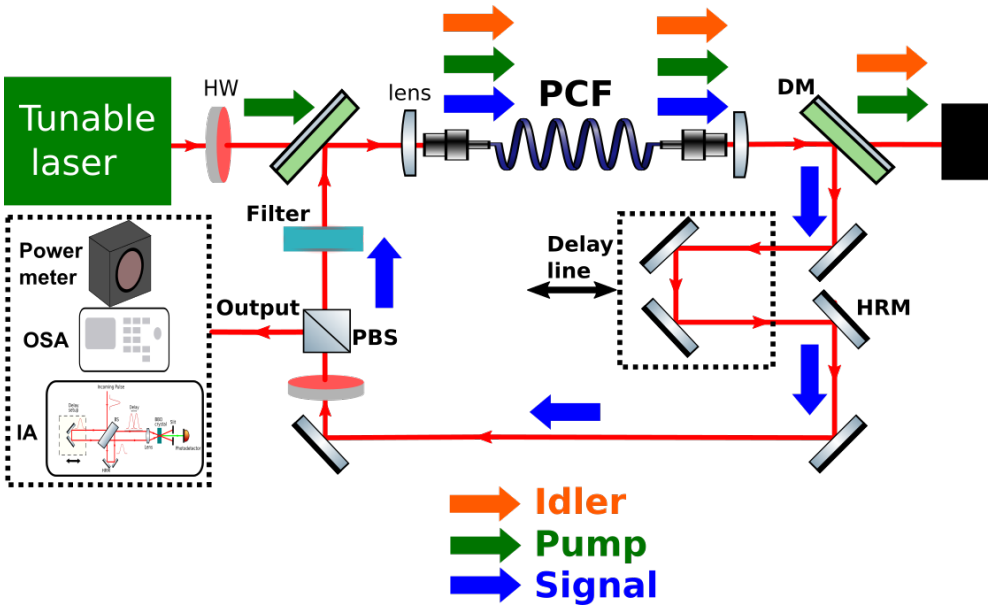

Figure 5.1: Schematic of fiber optical parametric oscillator. **HW**: half-wave-plate, **PCF**: photonic crystal fiber, **DM**: dichroic mirror, **HRM**: high reflecting mirror, **PBS**: polarizing beam splitter, **OSA**: optical spectrum analyzer, **IA**: intensity autocorrelator

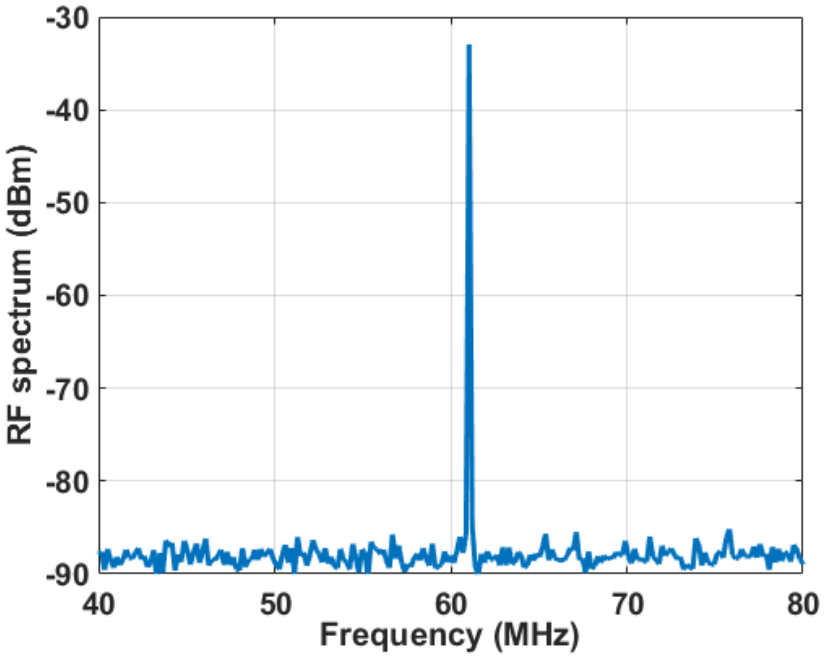

Figure 5.2: The RF spectrum, at a resolution bandwidth (RBW) of 1 kHz, shows the fundamental repetition rate around $\sim$ 61 MHz.

The focal length that optimizes the light coupling into the PCF is approximated by:

$$f = \frac{\pi(MFD)d}{4\lambda}, \tag{5.1}$$

where MFD is the mode-field diameter of the fiber, and d is the diameter of the input beam. Using the MFD and d values, the focal length of the lens comes out to be $\sim$4.3 mm for 1030 nm. The delay-line consisting of two high-reflecting mirrors (HRM) is used to harmonize the length of the OPO cavity according to the pump laser repetition rate ($\sim$61 MHz). The short-pass filter (DMSP1000-Thorlabs) is inserted just after the output port (PBS). Thanks to the two dichroic mirrors and a short-pass filter, only the signal wavelength is propagated through the OPO cavity which makes the laser cavity singly resonant. The output is taken through the polarizing beam-splitter (PBS) cube and characterized using a power meter, an optical spectrum analyzer (OSA), and a home-built intensity autocorrelator (IA).

5.2 Numerical simulations

In this section, the simulation regarding FWM in the photonic crystal fiber is discussed. The photonic crystal fiber used in the simulation is SC-1040-5.0-PM. For the simulation, a nonlinear coefficient of $11\,\mathrm{W^{-1}{\cdot}km^{-1}}$ and a mode-field diameter of $4.5\,\mu\mathrm{m}$ are considered. The zero-dispersion wavelength of this fiber is around 1040 nm. The β_2 curve was calculated from the dispersion trace provided by NKT photonics. The dispersion and β_2 curves of this fiber are plotted in Fig. 5.3.

To fulfill the phase matching equations of four-wave mixing, there is a need for higher order even $\beta(\omega)$ terms for instance, $\beta_2(\omega), \beta_4(\omega)$, and so on.

For the tunable pump wavelength range, the β_4 curve is plotted in Fig. 5.4. To simulate phase-matching curves, the injected pump average power was considered to be 230 mW, while the pulse duration was kept around 3.7 ps. The repetition rate was set to be 61 MHz.

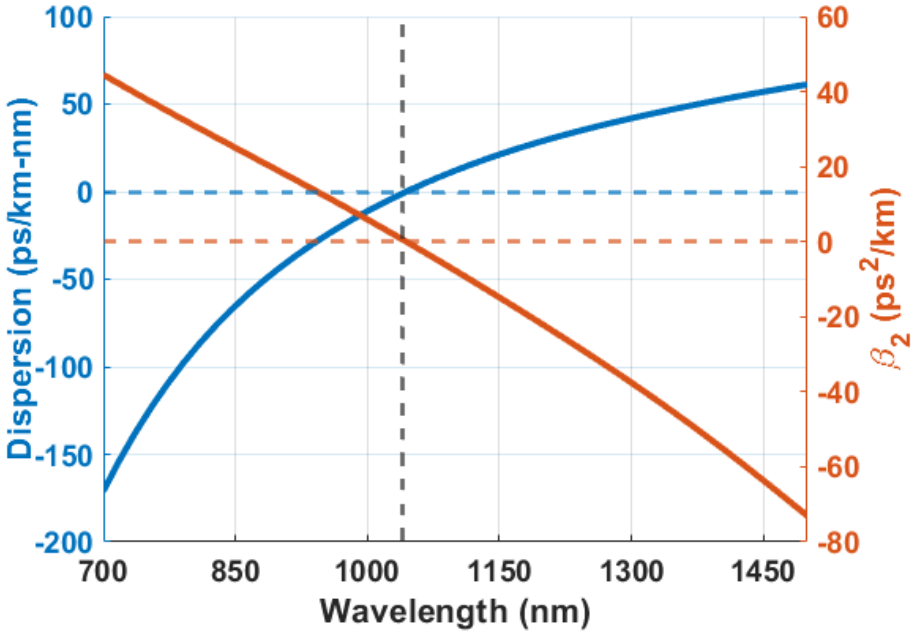

Figure 5.3: The dispersion and β_2 curves are plotted against the wavelength range from 700 nm to 1500 nm. The ZDW of this fiber is 1040 nm.

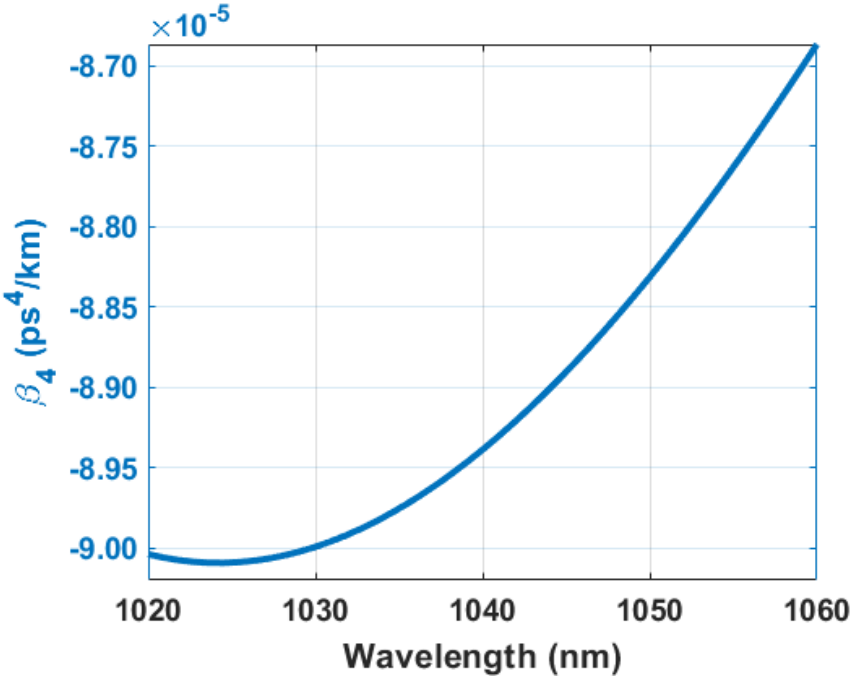

Figure 5.4: The values of β_4 for the tuning range of the central wavelength used in the experiment, ranging from 1020 nm to 1060 nm.

This corresponds to a peak power of 1.01 kW.

The result of the phase-matching equation (Eq. 3.19) is plotted against the frequency shift in Fig. 5.5. It is evident from the figure that, when the pump wavelength lies in the normal dispersion regime, the offset frequency shift is large which means that the generated parametric wavelength separation is large [113, 197, 204], while when the pump wavelength lies near ZDW or in the anomalous dispersion range, the offset frequency shift is close to the pump frequency [113, 197, 205]. The zero frequency shift in Fig. 5.5 corresponds to the pump wavelength.

The phase-matching frequency offsets are converted to wavelengths and plotted against the pump wavelength in Fig. 5.6. The signal wavelengths can be tuned from 760 nm to 1000 nm for the pump wavelengths from 1020 nm to 1060 nm, respectively. Similarly, for the same pump wavelength range, the idler wavelengths can be adjusted from 1125 nm to 1595 nm.

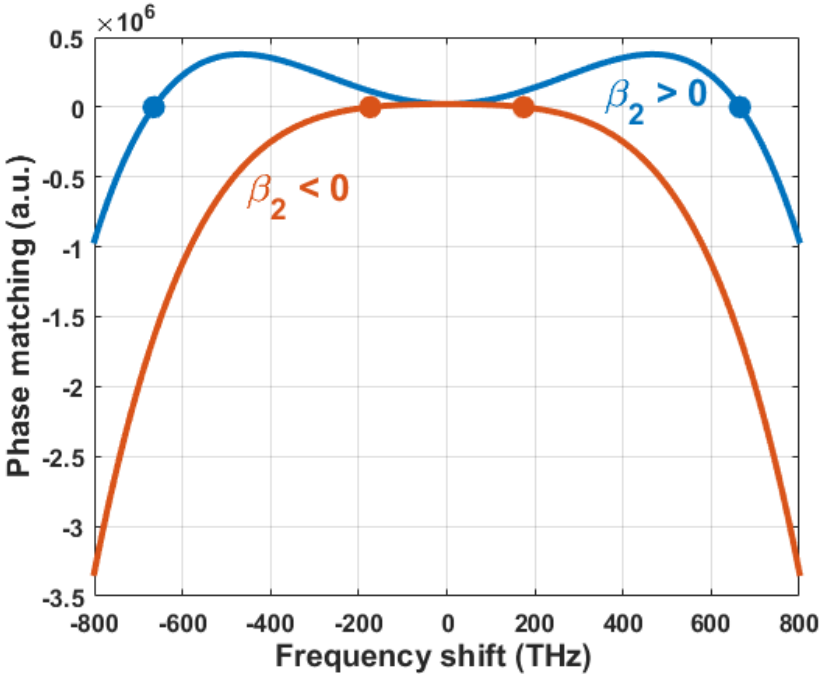

Figure 5.5: Phase matching curves for positive and negative group velocity dispersion, i.e. at **normal** and **anomalous** dispersion, respectively. The perfect phase matching occurs at the marked points shown in the figure.

The gain bandwidth at different pump wavelengths and the corresponding frequency shifts are plotted in Fig. 5.7. It is obvious from the figure, that in the normal dispersion, the phase matching occurs at widely separated frequency shifts having a very narrow bandwidth [204, 206]. Conversely, in the anomalous dispersion regime, the gain bandwidth is large but near the pump spectral regions [207–209]. The parametric gain is plotted in Fig. 5.8 for three different pump wavelengths, i.e. $\lambda_p = 1030\,\text{nm}$ (lies in normal dispersion), $\lambda_p = 1040\,\text{nm}$ (ZDW), and $\lambda_p = 1050\,\text{nm}$ (anomalous dispersion regime), respectively. The maximum value of the gain (peak) for a perfect phase matching can be approximated using Eq. 3.16 which comes out to be $1/4\exp(2\gamma P_p L)$ [210]. Similarly, parametric gain near pump wavelengths are estimated to be $(\gamma P_p L)^2$ [210] (Calculation given in Appendix A). As discussed before, the signal gain bandwidth is higher (and parametric generated wavelengths are widely separated) when the pump wavelength is in the normal dispersion region, and vice versa.

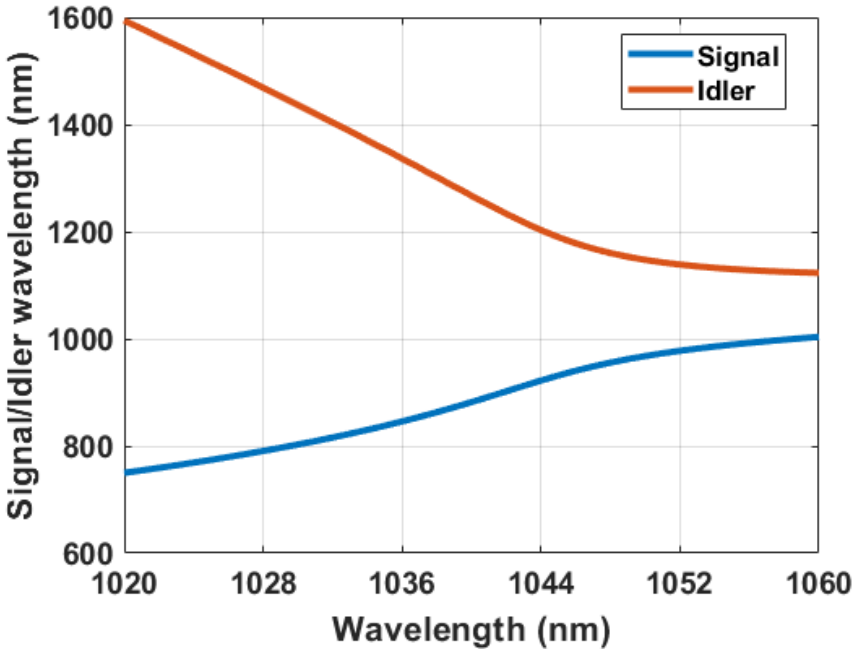

Figure 5.6: Signal and idler wavelength range corresponding to the pump wavelength range from 1020 nm to 1060 nm.

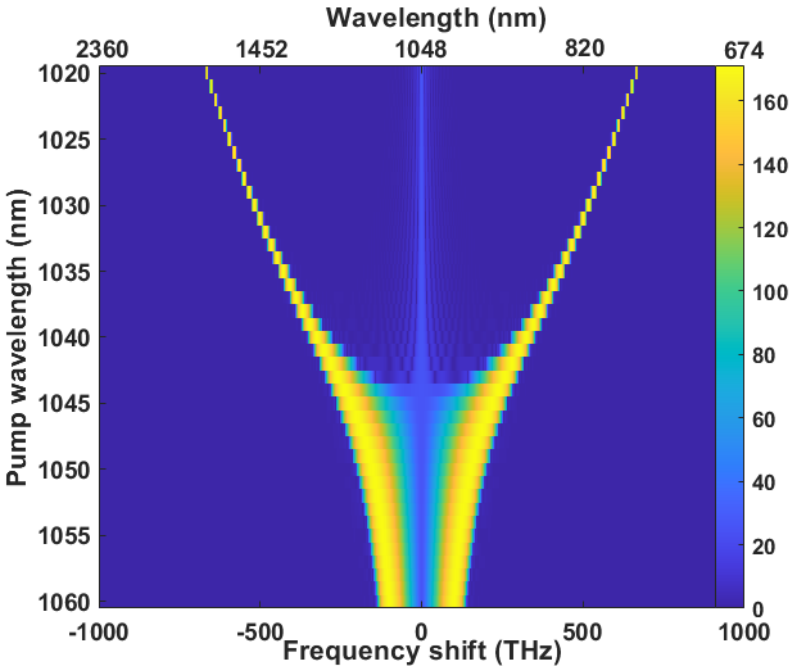

Figure 5.7: Parametric gain plotted against the pump wavelength and the corresponding frequency shift.

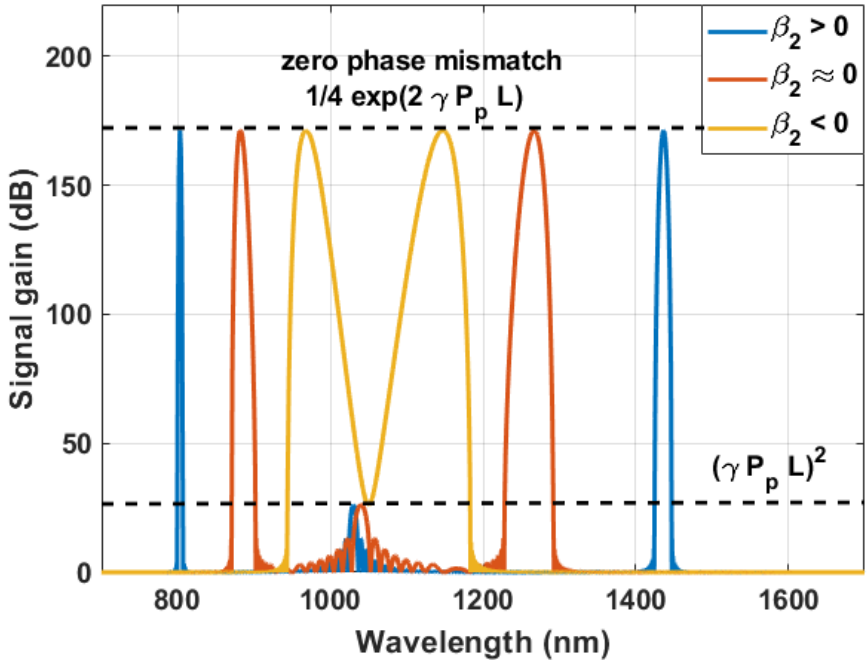

Figure 5.8: Parametric gain plotted against the pump wavelengths in the normal, near to ZDW, and anomalous regions. The maximum peak value of the parametric gain $(1/4\exp(2\gamma P_p L))$ is calculated from the parametric amplification equation.

Another important parameter to consider regarding four-wave mixing is the group velocity mismatch (GVM) of the different interacting wavelengths propagating inside the fiber. When the group velocity mismatch is different for the different interacting wavelengths, they will propagate with different velocities inside the fiber and eventually get separated from each other after a certain propagation distance. The larger the mismatch, the shorter the interaction length between the interacting wavelengths. The GVM writes:

$$GVM = \left| \frac{1}{v_{g_s}} - \frac{1}{v_{g_p}} \right| \tag{5.2}$$

where v_{g_s} and v_{g_p} are the group velocities at the signal and pump wavelengths, respectively.

These pulses will interact efficiently inside the fiber over an effective length L_{eff} given by:

$$L_{eff} = \frac{\Delta\tau}{\left|\frac{1}{v_{gs}} - \frac{1}{v_{gp}}\right|}, \tag{5.3}$$

5.3 Experimental results

For the experiments, the fiber OPO built around photonic crystal fiber having the length of $\sim$ 35 cm and $\sim$ 184 cm were considered. Here, in this section, results obtained from both PCFs are presented and compared. It is worth noting that, initially, we employed PCFs without attaching connectors, but this resulted in unstable performance. Even minor environmental and thermal fluctuations caused significant variations in the output power. Subsequently, we attempted to connecterize the PCF with an FC-APC connector, but this proved to be a challenging task, demanding a high level of expertise to prepare the nonlinear PCF for proper connecterization.

5.3.1 Fiber OPO results for 184 cm PCF

The pump wavelength from the tunable laser was coupled into the PCF and the output average power measured just after the PCF for different input average power is plotted in Fig. 5.9. The average power measured at the output of the PCF shows an increasing linear trend with the input pump average power while the coupling efficiency remains constant at around 70%. The threshold average pump power for the fiber OPO is around 100 mW near 1048 nm. As discussed above, the optical components in the OPO cavity are suited for signal propagation in the cavity, so the following discussion will be mainly related to the signal characterization. The signal average power and conversion efficiency at different pump powers are plotted in Fig. 5.10. The signal average power and the conversion efficiency show an increasing trend as the pump power is increased. In contrast, the conversion efficiency reaches a plateau of 20.4 % beyond a pump power of 250 mW. A

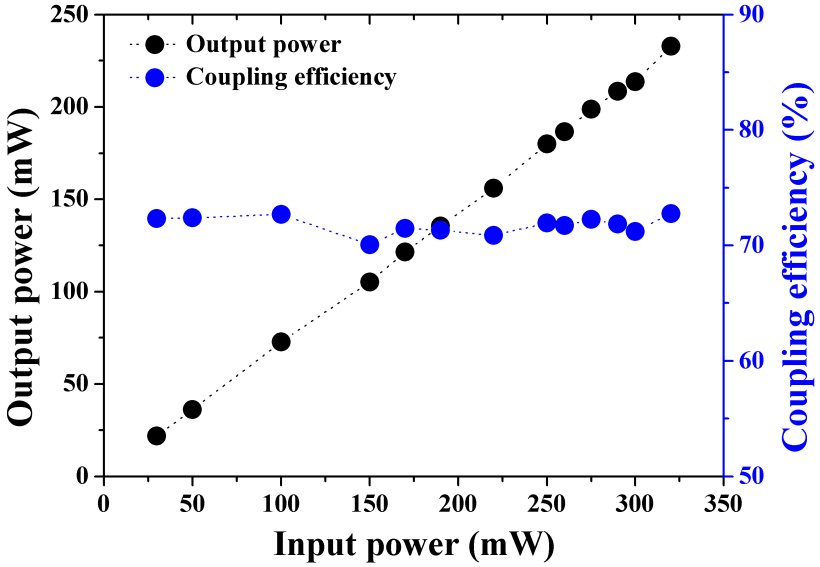

Figure 5.9: The average power measured at the output of PCF and the coupling efficiency are plotted against the input pump average power.

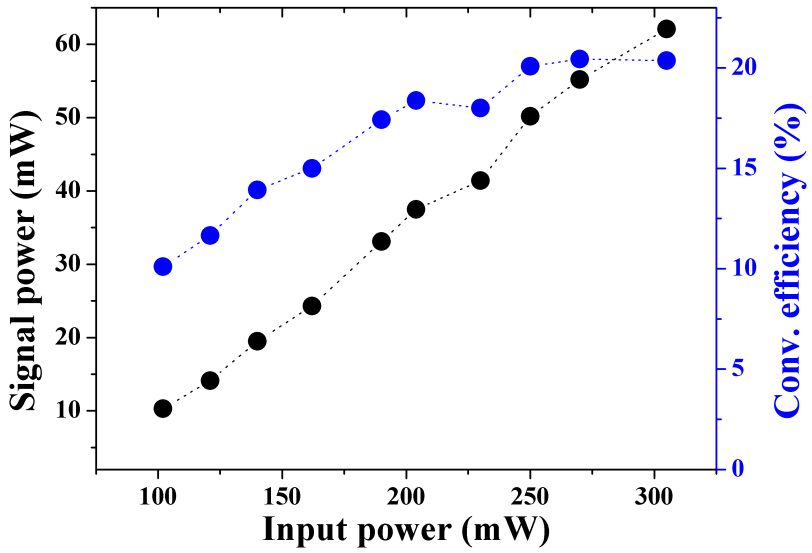

Figure 5.10: Measured signal average power and conversion efficiency at different pump powers.

maximum signal average power of ∼62 mW was recorded for an input power of ∼300 mW. The pump pulse at 1048 nm with an average power of 230 mW, propagates through the PCF OPO cavity. The spectra measured before and after the PCF are plotted in Fig. 5.11. The spectrum at the output of the PCF is broadened due to the self-phase modulation while propagating inside the fiber. The spectral width ($\Delta\lambda$) at the input of the PCF is about 0.73 nm, while the spectral width at the PCF output is around 5.87 nm. Similarly, the pump autocorrelation traces at the PCF input and output are plotted in Fig. 5.12. The autocorrelation widths at the input and output of the PCF are ∼ 5.29 ps and ∼ 5.43 ps, respectively. Considering a Gaussian pulse, the pulse durations corresponding to the autocorrelation widths are around 3.74 ps and 3.84 ps, respectively. The signal wavelength range can be tuned from ∼ 800 nm to ∼ 1000 nm for a pump wavelength ranging from ∼ 1030 nm to ∼ 1060 nm. The tunable pump spectra for the FOPO are plotted in Fig. 5.13. The corresponding autocorrelation traces are graphed in Fig. 5.14.

The aim is to make all the experiments at the same pulse duration at different central

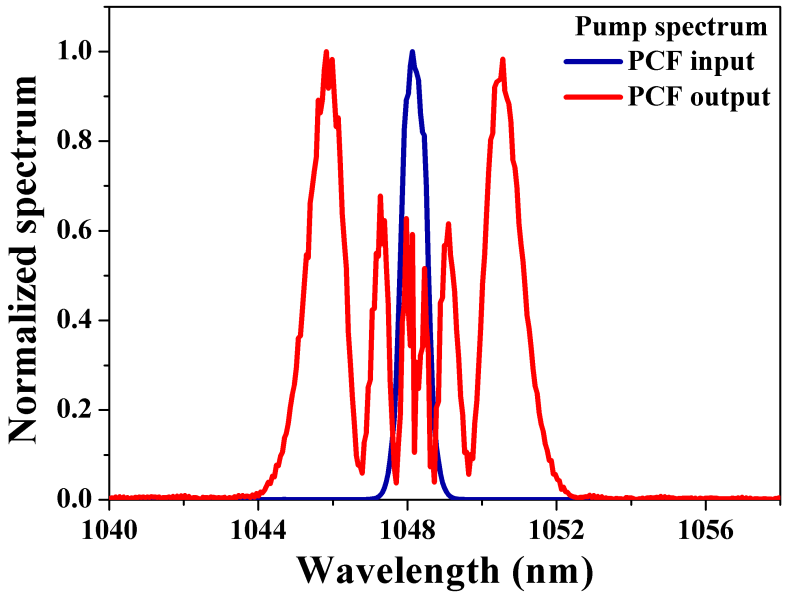

Figure 5.11: Injected pump spectrum (blue), the pump spectrum after propagating through PCF (red).

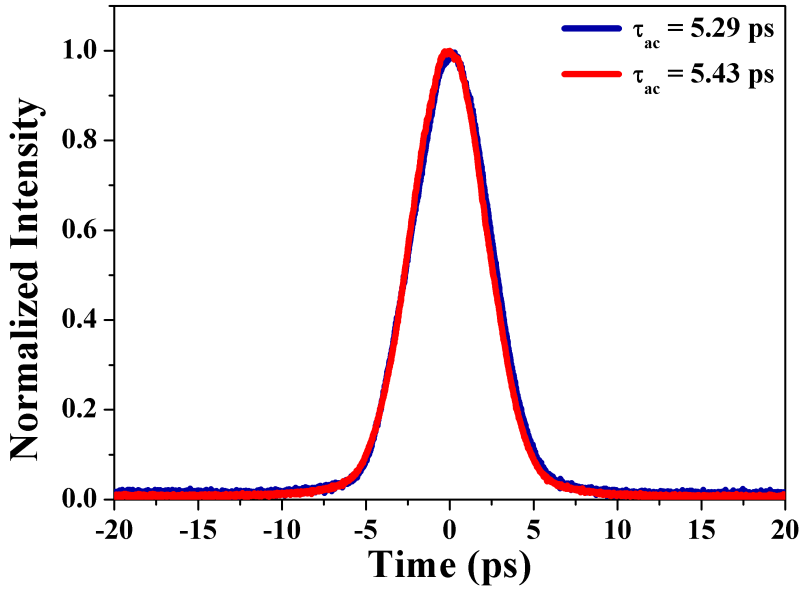

Figure 5.12: Autocorrelation traces of the pump at the input (blue), and after single-pass propagation through the PCF (red).

.

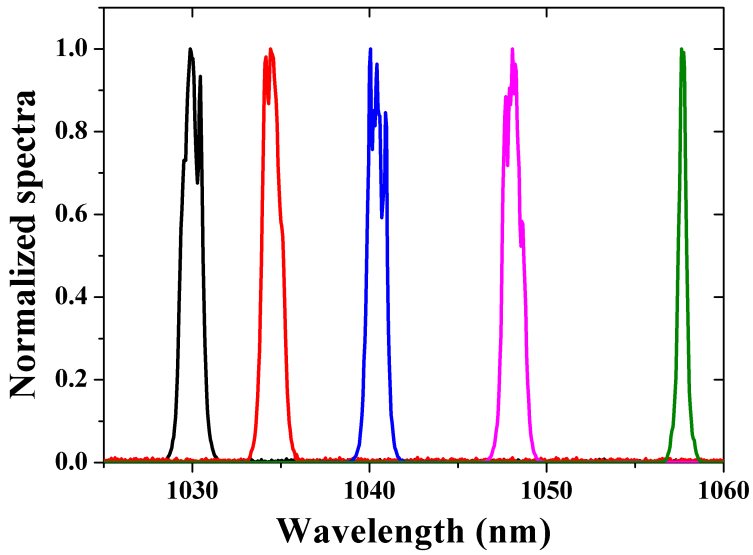

Figure 5.13: Injected pump spectra for tunable FOPO operation. The wavelength range is from $\sim$ 1030 nm to $\sim$ 1060 nm.

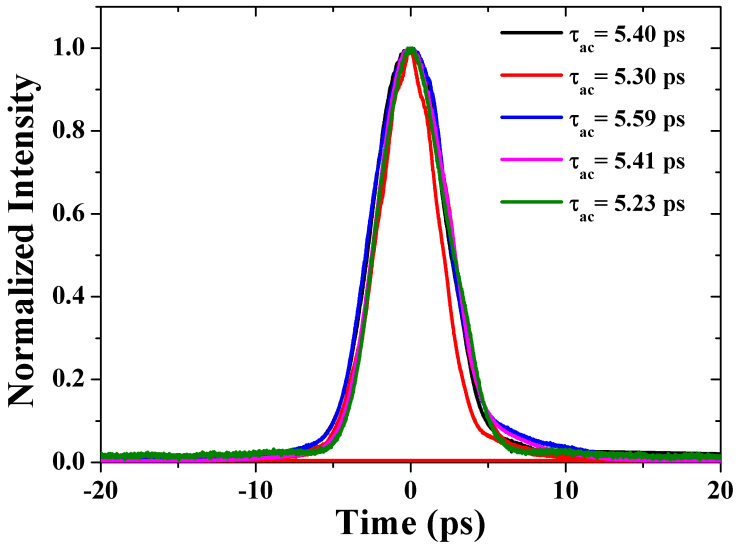

Figure 5.14: Injected autocorrelation traces at the input of the PCF of all the pump pulses at different central wavelengths (Fig. 5.13). The autocorrelation width of the pump pulse is made constant around ∼5.40 ps.

.

wavelengths. But, as discussed in chapter 4, at a constant slit width, the pulse duration is not the same at different central wavelengths. To keep the pulse duration constant, we need to slightly adjust the slit width. This is why the spectral width is slightly different at different central wavelengths. The autocorrelation width for the pump is kept around ∼ 5.40 ps. Considering a Gaussian pulse, the pulse duration is around ∼ 3.8 ps.

The normalized spectra for the tunable signal (corresponding to the pump wavelengths) are plotted in Fig. 5.15. Noteworthy is that the threshold pump power is higher when the pump wavelength lies away from the zero-dispersion wavelength. As discussed in chapter 3, to achieve notable four-wave mixing (FWM) effects, it is necessary to ensure phase matching. This involves pumping the fiber OPO in the vicinity of the zero-dispersion wavelength of the optical fiber. Since the phase matching condition also depends on the peak power, the peak power required to generate efficient four-wave mixing is higher when the pump wavelength lies away from the zero-dispersion wavelength (Eq. 3.20). For instance, the

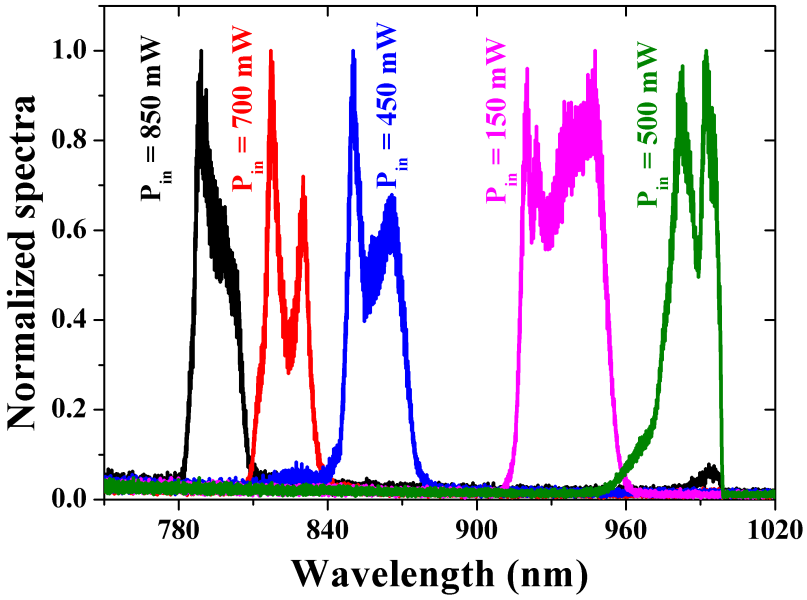

Figure 5.15: Signal wavelength tunable from the ∼ 800 nm to ∼ 1000 nm for the corresponding pump wavelength range plotted in Fig. 5.13.

.

average pump power to generate a stable signal around ∼ 800 nm is ∼ 850 mW, while it is ∼ 150 mW when the pump wavelength is at ∼ 1048 nm. Additionally, the spectral width of the generated signal is higher when the pump wavelength lies near the zero-dispersion wavelength range and vice versa. It is evident in Fig. 5.15 that the spectral widths are around 34 nm and 16 nm when the pump wavelengths are ∼ 1048 nm and ∼ 1030 nm, respectively. Although the FOPO cavity is singly resonant for the signal wave, but in order to show experimentally that the signal we obtained mainly resulted from a phase-matched four-wave-mixing process and not from other nonlinear processes, we also measured the idler spectra at the output of the PCF after the second dichroic mirror in Fig. 5.1, with the use of a long-pass filter (FELH-1200, Thorlabs). The idler spectra for the pump wavelengths at 1030 nm, 1048 nm and 1059 nm are plotted in Fig. 5.16. The idler spectrum for the pump wavelength of 1030 nm has a dominant peak around 1450 nm and a broad but weak peak around 1160 nm, a similar small peak is also observed for the signal in Fig.

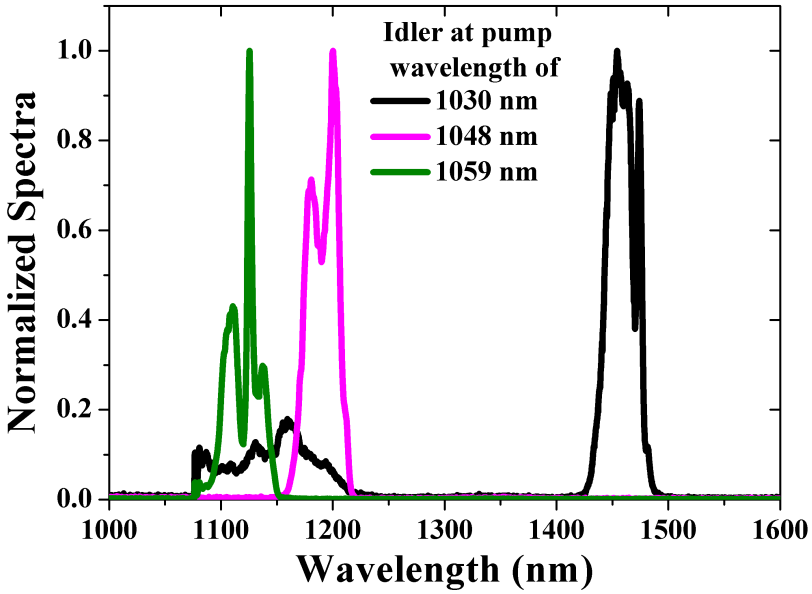

Figure 5.16: Idler spectra for the corresponding pump wavelengths plotted in Fig. 5.13.

.

5.15. We believe that these small peaks in signal and idler spectra come from the fact that the peak power is quite high for the parametric generation around 1030 nm, and consequently due to SPM the pump spectrum is quite broadened and it has dominant spectral components near 1060 nm which correspondingly generate signal and idler, as well.

5.3.1.1 Signal evolution vs delay positions

The delay line in the fiber OPO setup is mainly used to harmonize the cavity length according to the pump laser's repetition rate. Once the delay line is adjusted for the optimal fiber OPO output power, this delay line in our setup can be used to select a narrow or broad bandwidth signal. Contrary to the conventional FOPOs, in which a long dispersion fiber is used to achieve a narrow bandwidth amplification [74], the delay line in our setup makes it possible to delay (or advance) the signal pulse with respect to the pump at the entrance of the PCF fiber. This allows us to switch from broad to narrow

bandwidth signal, at the expense of a loss in conversion efficiency. The signal power and the corresponding conversion efficiency evolutions versus the delay are plotted in Fig. 5.17 for a constant pump power of 230 mW. The delay of 0 ps does not necessarily mean that the signal and the pump pulses reach the input of the photonic crystal fiber at the same time, but it is related to the maximum interaction of the signal and pump while propagating inside the fiber so that the output power is maximum. The signal average power at 0 ps delay is maximum, i.e. ∼40 mW, while the achieved conversion efficiency is around 17.4 %. As evinced from the figure, when the signal is delayed or advanced corresponding to the pump the interaction is not optimal and the output power is decreased. For instance, the measured signal average powers are ∼11.2 mW and ∼10.7 mW for −2.4 ps and 2.2 ps delay positions, respectively. The corresponding signal conversion efficiencies at these delay positions are 4.86 % and 4.65 %, respectively. Fig. 5.18 shows the spectra at different delay positions. The spectrum when the delay is 0.0 ps is quite broad and spans over ∼ 46 nm. Once the signal is advanced or delayed, the spectra are narrowed, and the spectral widths ($\Delta\lambda$) are ∼ 6 nm and ∼ 0.8 nm, respectively. The beam shape of the fiber OPO

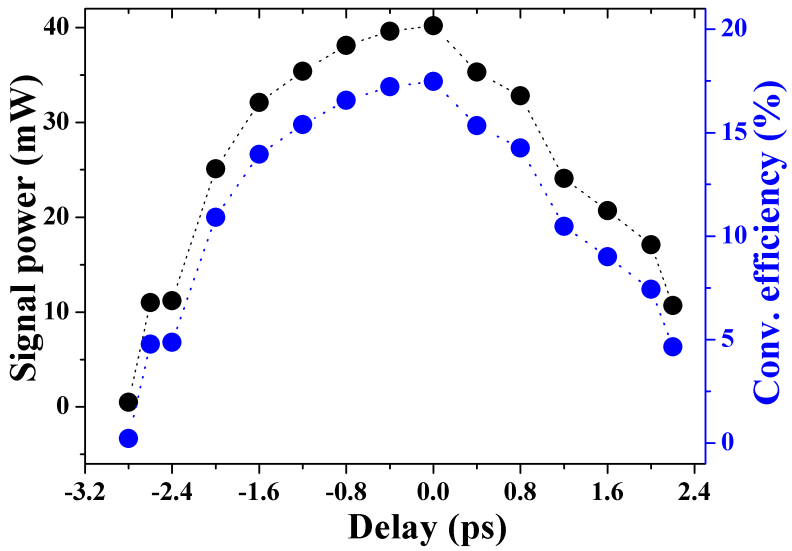

Figure 5.17: Measured signal power and conversion efficiency at different delay positions.

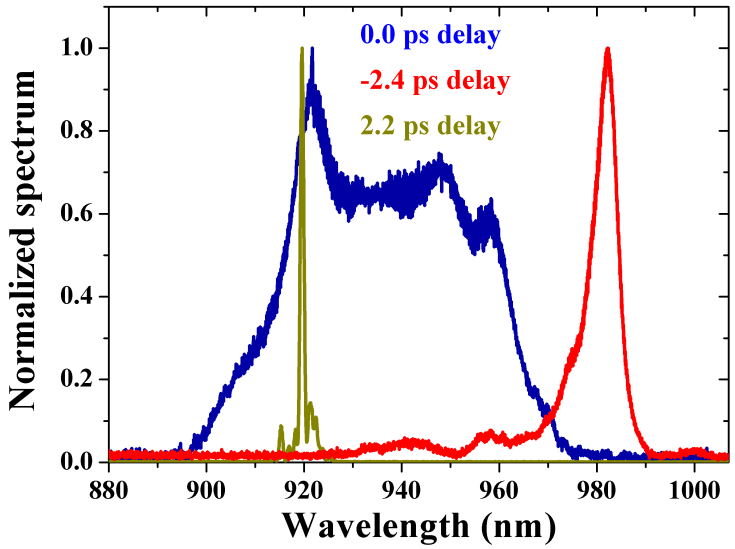

Figure 5.18: The spectra plotted at −2.4 ps, 0.0 ps, and 2.2 ps, respectively.

for a broadband signal is plotted in Fig. 5.19. The beam shape remains the same for different power levels and also for the narrowband signal. Corresponding to the broadband signal spectrum and considering Gaussian pulse, the Fourier limited pulse duration was calculated by taking the Fourier transform of the spectrum and is plotted in Fig. 5.20. The transform-limited pulse duration comes out to be ∼46 fs. The autocorrelation trace

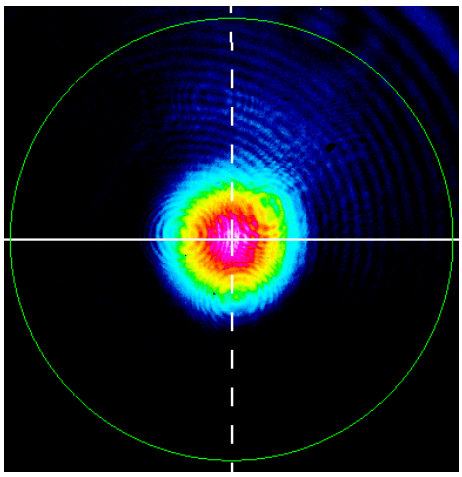

Figure 5.19: Beam shape of the signal at the output of the fiber OPO at 230 mW. The beam shape remains the same at different power levels.

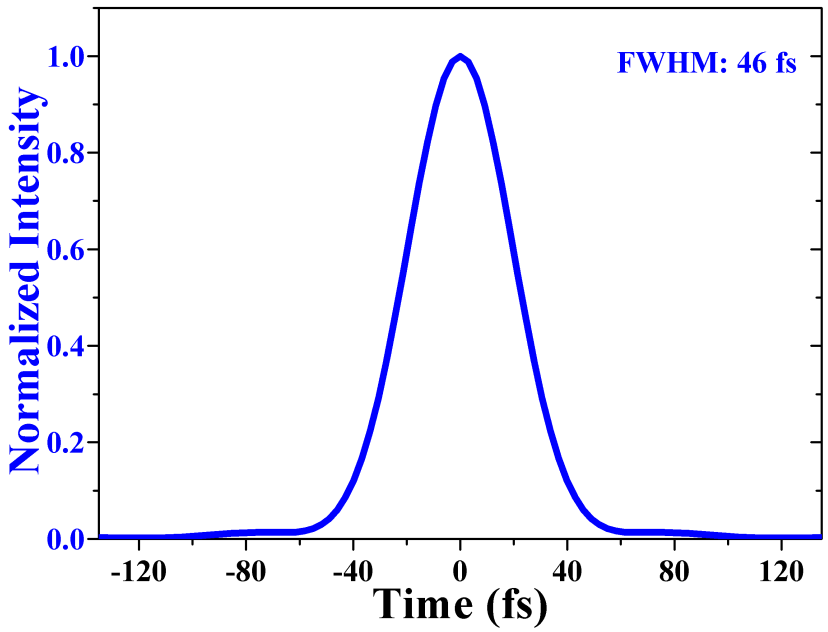

Figure 5.20: Considering the Gaussian pulse, the Fourier limited pulse duration is calculated by taking the Fourier transform of the broadband spectrum plotted in Fig. 5.18. The transform-limited pulse duration is around 46 fs.

was measured for the broadband spectrum and is plotted in Fig. 5.21. The autocorrelation width is around 4.66 ps. Considering a Gaussian pulse, the pulse duration is around 3.3 ps. This means that the signal pulse is heavily chirped. Noteworthy is that there is a narrow sharp peak (coherence spike) in the center of the autocorrelation trace, and the width of this peak is $\sim$ 170 fs. The autocorrelation trace has a similarity to the trace produced by a noise-like pulse (NLP) [211–215] or having a complex temporal profile. One of the reasons for this kind of autocorrelation trace is that the pulse is highly structured in the temporal domain. The pronounced central peak indicates variations in the spectrum of the pulse, while the pedestal quantifies the pulse's overall intensity envelope.

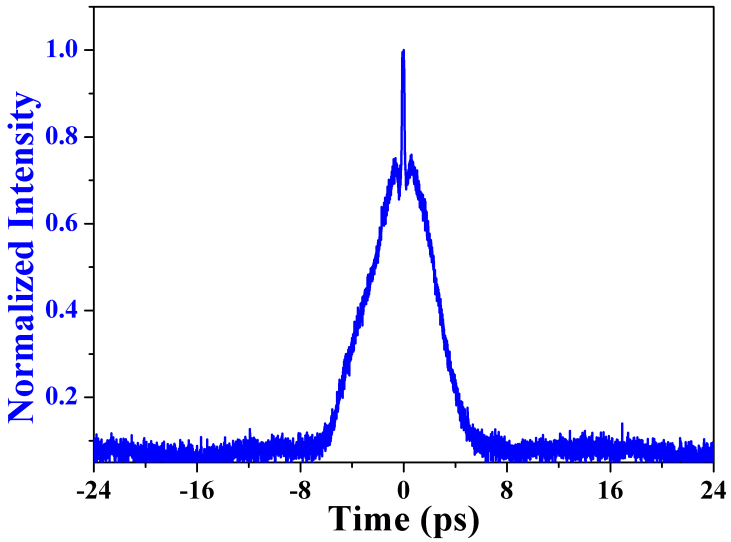

Figure 5.21: The autocorrelation trace measured corresponding to the broadband signal spectrum plotted in Fig. 5.18.

5.3.2 Fiber OPO results for 35 cm PCF

In this section, the results regarding the 35 cm PCF are discussed. The reason behind changing the length of the fiber is to cover the whole tuning range of the pump wavelengths and to obtain the corresponding parametric generated wavelengths. Because of the group velocity mismatch, the interaction length is quite small for the wavelengths less than 1030 nm, which is why there is no effective phase matching in the long fiber for these wavelengths. Similar to the previous setup, the achieved coupling efficiency was around 70% (Fig. 5.22). But now the threshold power for the parametric generation is increased to 350 mW as the length of the fiber is lowered. For a pump wavelength around 1048 nm, the average power measured at the output of the PCF shows an increasing linear trend with the input pump average power while the coupling efficiency remains constant at around 70%. The signal spectra at pump powers of 350 mW, 550 mW, 750 mW, 950 mW and 1100 mW are plotted in Fig. 5.23. It can be seen from the figure that, as the pump power is increased, the spectral widths of the generated signal are increased. The spectral width

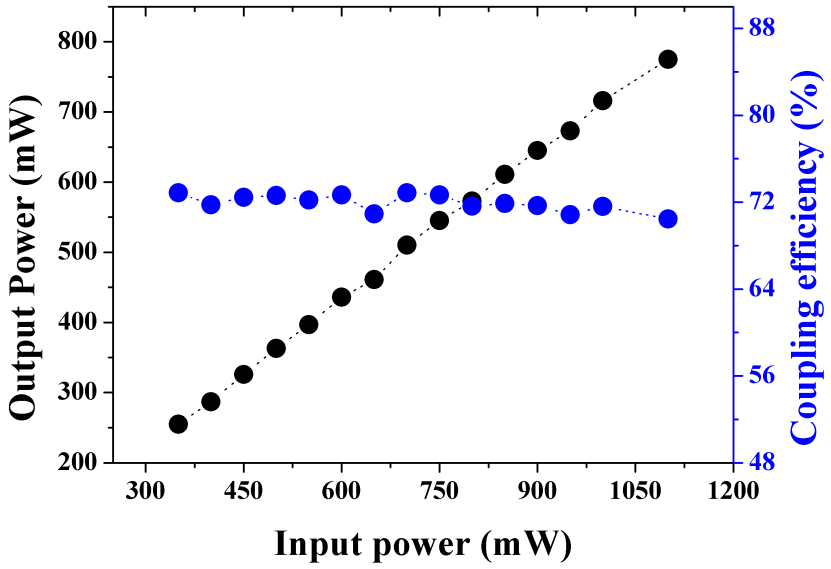

Figure 5.22: The average power measured at the PCF output and the coupling efficiency are plotted against the input pump average powers at a central wavelength of 1048 nm.

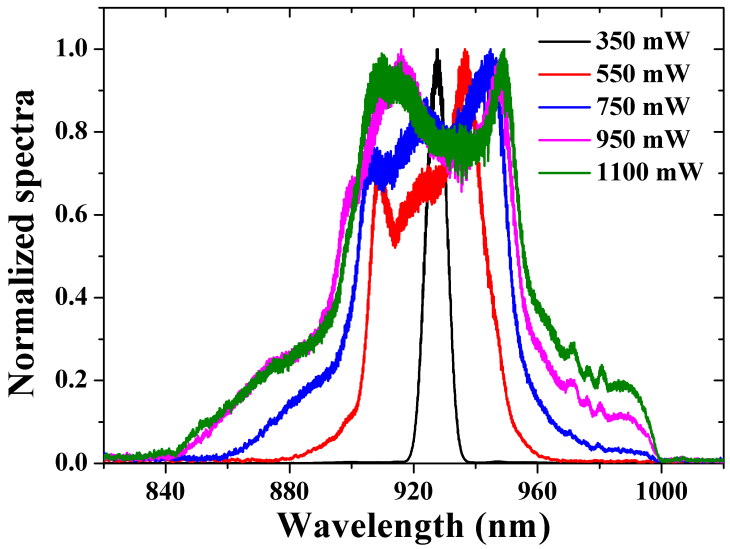

Figure 5.23: Signal spectrum measured at different pump power levels when the pump wavelength is at 1048 nm.

(FWHM) for 350 mW is around 8 nm, while the spectral width for 1100 mW is $\sim$ 60 nm, but it is worth noticing that the pedestal of the spectrum spans over a broad range from

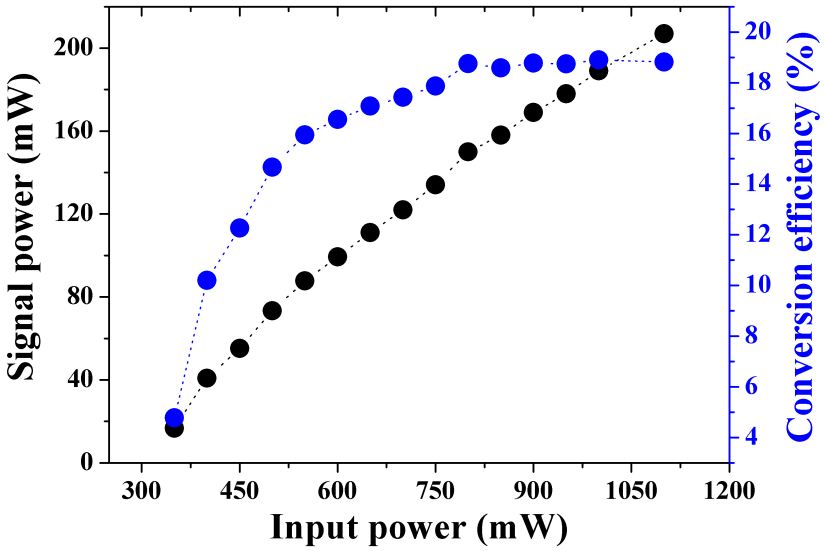

Figure 5.24: Measured signal power and conversion efficiency for different pump power levels at a central wavelength of 1048 nm.

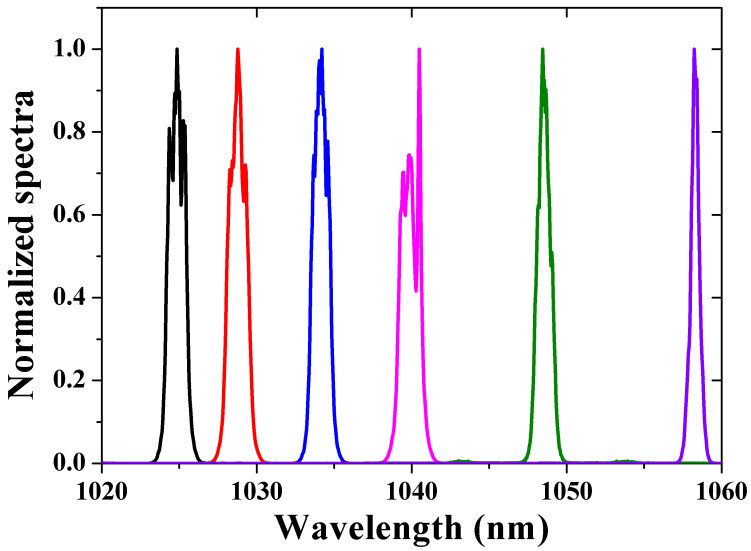

Figure 5.25: Injected pump spectra for tunable FOPO operation. The pump wavelength range is from ∼ 1024 nm to ∼ 1060 nm.

∼ 850 nm to ∼ 990 nm. The signal average power and conversion efficiency for different pump powers at a central wavelength around 1048 nm are plotted in Fig. 5.24. The signal

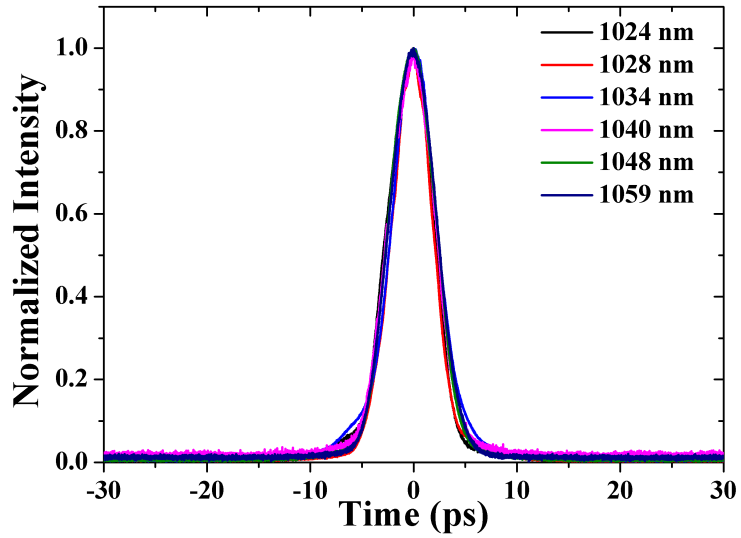

Figure 5.26: Injected autocorrelation traces of the pump pulses at the input of the PCF at different central wavelengths (Fig. 5.25). The autocorrelation width of the pump pulse is made constant around ∼5.40 ps.

.

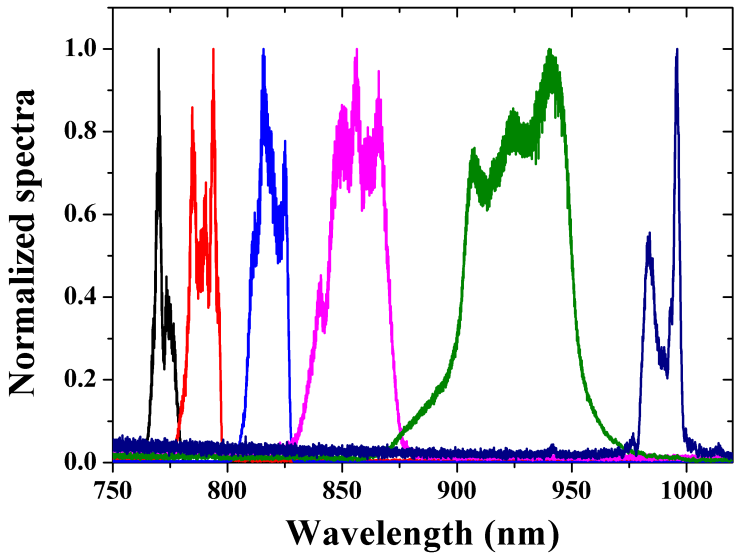

Figure 5.27: Signal wavelength tunable from the ∼ 770 nm to ∼ 1000 nm for the corresponding pump wavelength range plotted in Fig. 5.25.

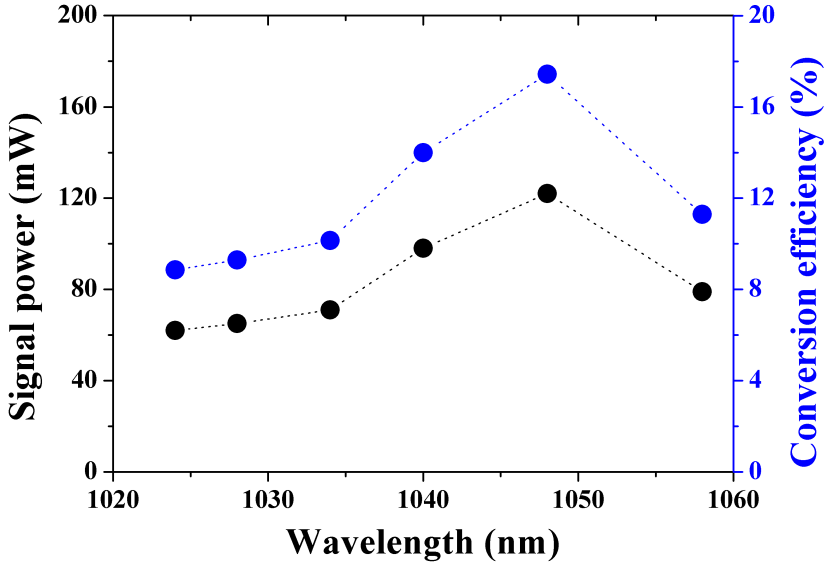

Figure 5.28: Signal output average power measured at different central wavelengths and the corresponding conversion efficiency.

power shows an increasing trend as the pump power is increased. Similarly, the conversion efficiency also shows an increasing trend at the start and reaches a plateau of 18 % after a pump power of 750 mW. A maximum average output signal power of $\sim$ 207 mW was recorded for an input power of $\sim$ 1.1 W. The signal wavelength range can be tuned from $\sim$ 770 nm to $\sim$ 1000 nm for the pump wavelength ranging from $\sim$ 1024 nm to $\sim$ 1060 nm. The tunable pump spectra for the FOPO are plotted in Fig. 5.25 at a constant pump power of 700 mW. The corresponding autocorrelation traces are graphed in Fig. 5.26. As mentioned previously, to keep the pulse duration constant, we need to slightly adjust the slit width. This is why the spectral widths are slightly different at different central wavelengths. The autocorrelation widths are kept around $\sim$5.40 ps and correspondingly, the pulse durations around $\sim$3.8 ps. The normalized spectra for the tunable signal from $\sim$ 770 nm to $\sim$ 1000 nm (corresponding to the pump wavelengths of Fig. 5.25) are plotted in Fig. 5.27. Additionally, as discussed above, the spectral width of the generated signal is higher when the pump wavelength lies near the zero-dispersion wavelength or in the anomalous dispersion range. It is evident in Fig. 5.27 that the spectral widths of

the signal are around 47 nm and 13 nm when the pump wavelengths are ∼ 1048 nm and ∼ 1029 nm, respectively. Fig. 5.28 shows that for the same injected pump power, the conversion efficiency decreases as the FOPO is pumped far away from the ZDW because the phase mismatch and group velocity mismatch becomes significant, resulting in reduced efficiency.

5.3.2.1 Signal evolution vs delay positions

The signal power and the corresponding conversion efficiency evolutions versus the delay are plotted in Fig. 5.29 for a constant pump power of 600 mW. The signal average power at

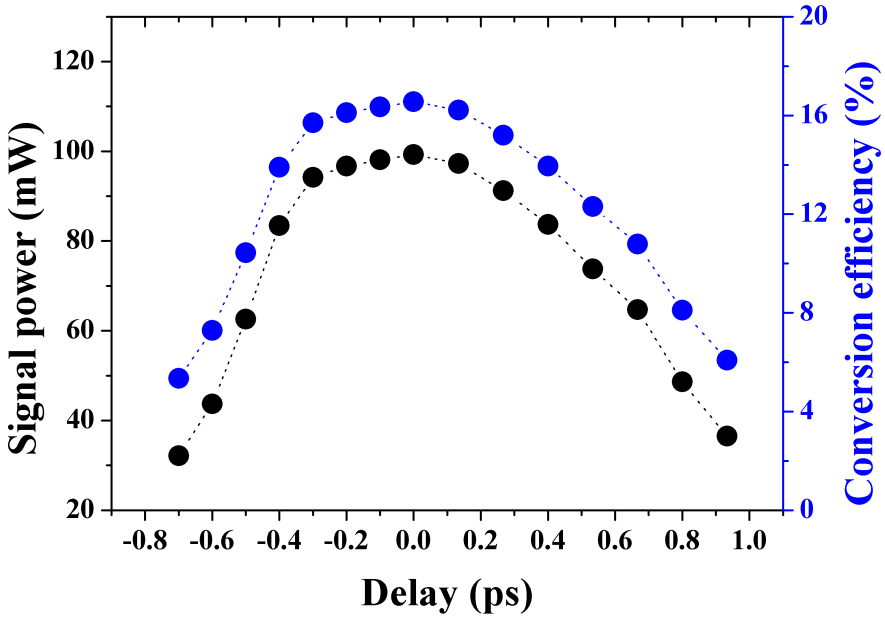

Figure 5.29: Measured signal power and conversion efficiency at different delay positions.

a 0 ps delay is maximum, i.e. ∼ 99.3 mW, while the achieved conversion efficiency is around 16.6%. As shown from the figure, when the signal is delayed or advanced corresponding to the pump, the interaction is not optimal, and the output power is decreased. For instance, the measured signal average powers are ∼32.1 mW and ∼36.5 mW for −0.7 ps and 0.9 ps delay positions, respectively. The corresponding signal conversion efficiencies at these

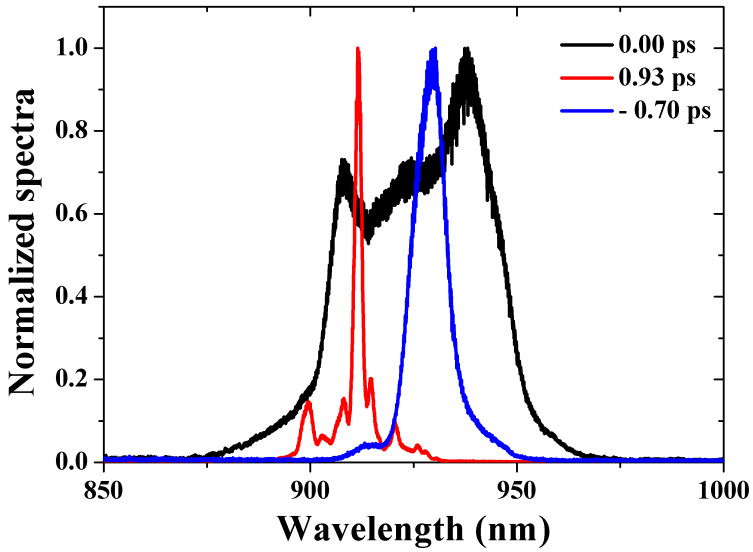

Figure 5.30: The spectra plotted at -0.7 ps, 0.0 ps, and 0.93 ps, respectively.

delay positions are 5.4% and 6.1%, respectively. The spectra at different delay positions are plotted in Fig. 5.30. The spectral width, when the delay is 0.0 ps is quite broad ($\Delta\lambda \sim$

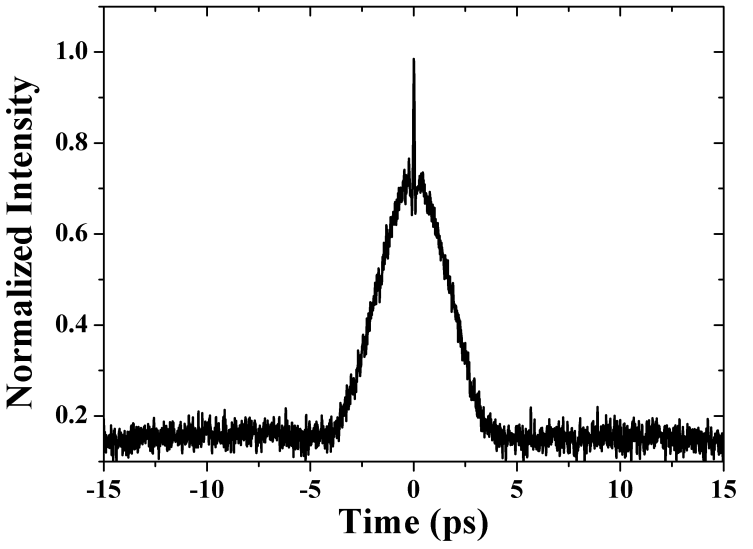

Figure 5.31: The autocorrelation trace corresponding to the broadband signal spectrum plotted in Fig. 5.30.

48 nm). Once the signal is advanced or delayed, the spectra are narrowed, and the spectral widths are $\sim$ 9 nm and $\sim$ 2 nm, respectively. The autocorrelation trace was measured for the broadband spectrum and is plotted in Fig. 5.31. The autocorrelation width is $\sim$ 3.7 ps. Considering a Gaussian pulse, the pulse duration is around 2.45 ps. Similar to the previous autocorrelation trace, there is a narrow sharp peak (coherence spike) in the center of the autocorrelation trace, and the width of this peak is $\sim$ 65 fs.

5.4 Continuum generation

Supercontinuum generation based on microstructured fiber has many applications, for instance, but not limited to, nonlinear imaging [216], telecommunication [217], spectroscopy [218], and optical frequency metrology [219], etc. The starting evolution of the supercontinuum generation was observed in bulk material [220], but greatly developed with the use of microstructured fiber [106, 109, 221]. The underlying phenomena behind the SC generation are the nonlinear effects occurring in the fiber when an ultrashort pulse is propagated through it. These phenomena include SPM, SRS, FWM, and self-steepening [89], etc. The complete description of SC generation can be numerically explained using the generalized nonlinear Schrodinger equation (GNLSE) but it is outside the scope of this manuscript. The fiber (SC-5.0-1040-PM) we have used for our experiments has been utilized for continuum generation in the recent past [75, 222, 223]. In this section, we are presenting the findings regarding the generation of a broad spectrum in our experiments at a high pump power.

The pump pulse (described above) around 1048 nm is injected in a 184 cm photonic crystal fiber at an average power of $\sim$ 1 W. This corresponds to a peak power of around 4.4 kW. The signal average power measured at the output of the FOPO was $\sim$ 198 mW. The signal spectrum recorded at the output of the FOPO is plotted in Fig. 5.32. The spectrum is quite broad, ranging from $\sim$ 750 nm to $\sim$ 1000 nm. The spectrum is broadened

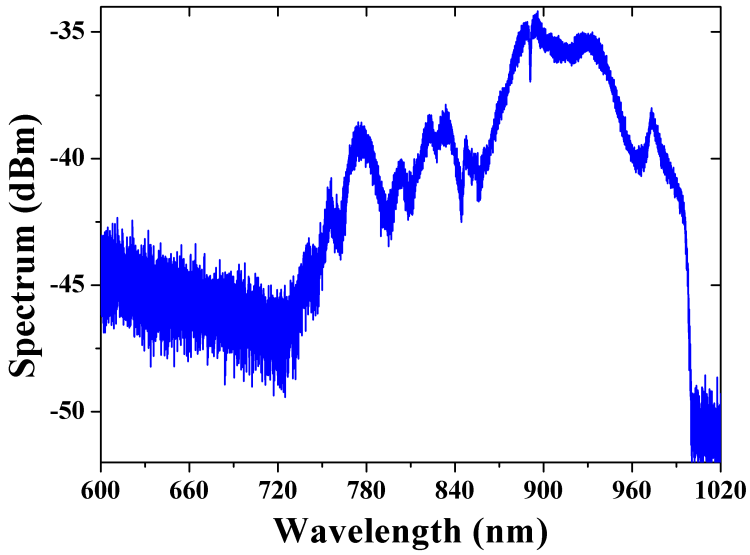

Figure 5.32: Broad signal spectrum ($\sim$ 750 nm to $\sim$ 1000 nm) measured at the output of the FOPO for the pump wavelength around 1048 nm at a pump average power of 1 W.

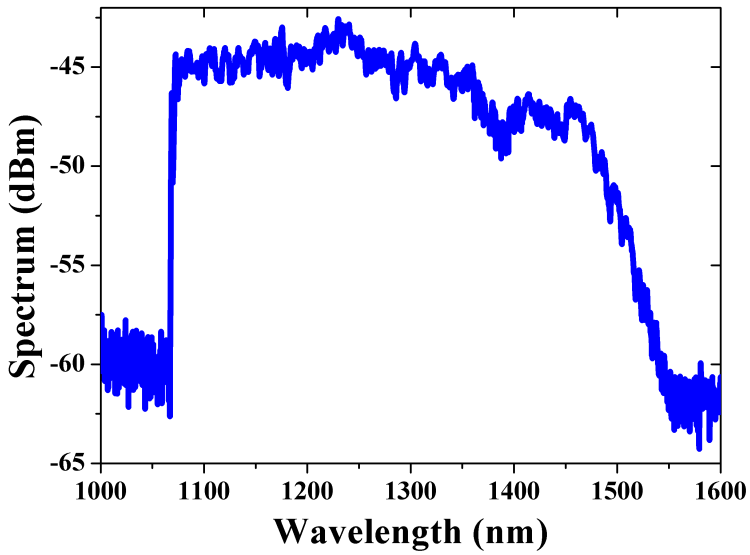

Figure 5.33: Broad idler spectrum measured at the output of the PCF after the second dichroic mirror in Fig. 5.1 for a pump wavelength around 1048 nm at a pump average power of 1 W.

to the green wavelength range on the left and to almost the pump wavelength range on the right, but the optical components and short pass filter in the FOPO cavity only allow the transmission of the spectrum from $\sim 750\,\text{nm}$ to $\sim 1000\,\text{nm}$. Correspondingly, the idler spectrum is analyzed at the output of the PCF after the second dichroic mirror, and, as expected, the spectrum is quite broadened and spans over $>450\,\text{nm}$ (Fig. 5.33). This experimental setup can be used to generate a broad continuum ranging from $\sim 750\,\text{nm}$ to $\sim 1550\,\text{nm}$ when the output is taken just after the photonic crystal fiber.

Chapter 6

Discussion and conclusion

In this work, a detailed study has been done to investigate picosecond fiber laser working in an all-normal-dispersion regime for the application of parametric generation in photonic crystal fiber. In conclusion, we have developed a high-power laser source delivering picosecond pulses with tunability both in central wavelength and spectral width. It incorporates a combination of a large-mode-area rod-type ytterbium fiber, a slit, and a transmission grating inside the ring laser cavity configuration. At the central wavelength of $\sim 1030\,\text{nm}$ and with a repetition of 78 MHz, this laser delivers picosecond pulses up to 25 W of average power, with pulse duration τ_p which can be continuously adjusted from $\sim 1.8\,\text{ps}$ to $\sim 4.5\,\text{ps}$ and pulse energy from $\sim 320\,\text{nJ}$ and $\sim 225\,\text{nJ}$, respectively. The pulses with the longer pulse duration are almost Fourier-limited (HWTBP~ 0.48) whereas for the shorter ones, the HWTBP is at most about 1.2. We have also demonstrated the central wavelength of the laser pulse can be continuously tuned from $\sim 1010\,\text{nm}$ to $\sim 1060\,\text{nm}$ while keeping the pulse energy above $\sim 150\,\text{nJ}$. Contrary to conventional femtosecond ANDi laser, to control the spectral width of the generated pulse while achieving an almost Fourier-limited picosecond pulse, our ANDi laser is running without adding any passive optical fiber in the laser cavity [186]. We have also adapted a previously proposed numerical model to account for the ensemble of our experimental data [186]. Our numerical simulations capture well the experimental trends. While the numerical and experimental spectra and energies of the pulses are in good agreement, the experimental HWTBPs are shorter than the numerical ones. As we already mentioned, this phenomenon can be associated with the difference in the transfer function of SA and NLOP. However, we also suspect the folded-4f dispersion

line to partly compensate for the frequency chirp experienced by the laser pulse during its propagation within the laser cavity. However, based on our simulations, the remaining nonlinear frequency chirp will be difficult to compensate by a conventional grating compressor.

The output of this fiber oscillator is propagated through the photonic crystal fiber for the parametric generation of the signal and idler. The fiber OPO singly-resonant cavity was built in such a way that only signal wavelengths are allowed to propagate through it. Based on numerical simulations, when the pump wavelength lies in the normal dispersion region, the frequency shift for the signal is large with a narrow gain bandwidth. The frequency shift is small when the pump lies in the anomalous region having a broader signal gain bandwidth. The two different FOPO cavities were built and characterized. Firstly, the output of the FOPO cavity with a 184 cm PCF was studied, and then the PCF length was changed to 35 cm. The latter cavity was used to obtain parametric generation for the whole tuning range of the pump wavelengths because the parametric generation is strictly dependent on the fiber length due to the group velocity mismatch factor. The conversion efficiency for the signal was close to 20% in both FOPO cavities. The FOPO with 35 cm PCF, the signal was tuned from $\sim$ 770 nm to $\sim$ 1000 nm for the corresponding pump wavelengths of $\sim$ 1024 nm to $\sim$ 1059 nm. In both FOPOs, the signal evolution versus the delay line was studied for the pump wavelength of 1048 nm at a constant pump power level. Both broad and narrow signal bandwidths were observed. Contrary to the conventional fiber OPOs, in which a long dispersion fiber is used to obtain a narrow bandwidth signal [17], the delay line in our fiber OPO setup makes it possible to delay the signal pulse with respect to the pump at the entrance of the PCF fiber. This allows us to switch from broadband to narrowband signal, at the expense of a loss in conversion efficiency. The obtained pulse durations in all results were in the picosecond regime and highly chirped. In addition to parametric generation, we have also briefly investigated continuum generation in a longer photonic crystal fiber (184 cm) at high pump powers even for a picosecond pulse duration pump. For a pump power of 1 W at 1048 nm, the

signal spans from ∼750 nm to 1000 nm, while the idler ranges from 1070 nm to ∼1550 nm.

Future prospects

Coherent Raman imaging

The fiber OPO seeded by the rod-type ytterbium fiber laser can be used for biomedical applications, especially for the physiology of the tissue and protein [**?**]. The basic principle behind this is the stimulated Raman scattering technique which is illustrated in Fig. 6.1. The two laser beams at the pump frequency (ω_p) and idler frequency (ω_I) are focused onto the biomedical sample, and when the frequency difference between them resonates with a molecular vibration, it triggers the stimulated emission at $\omega_{res} = \omega_p - \omega_I$.

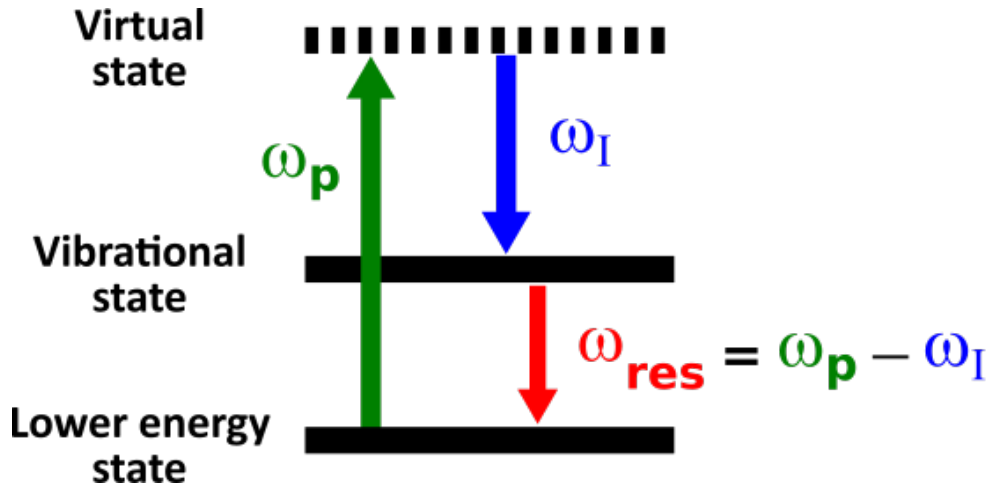

Figure 6.1: Simple energy diagram of stimulated Raman scattering (SRS). In the process of SRS, a pair of laser beams at pump frequency (ω_p) and idler frequency (ω_I) are directed at the sample. When the difference in their frequencies aligns with a molecular vibration within the sample, it triggers stimulated emission at the corresponding frequency (ω_{res}).

Based on our widely tunable OPO, molecular vibrations from $\sim 560\,\mathrm{cm}^{-1}$ to $\sim 3220\,\mathrm{cm}^{-1}$ can be excited. Within this range, many different molecular excitation frequencies can be excited, for instance, benzene-ring-breathing vibration near $1000\,\mathrm{cm}^{-1}$, C-N stretch and N-

H bend near 1300 cm^{-1}, C-N bend and N-H stretch around 1550 cm^{-1} C$\equiv\equiv$0 stretch near 1650 cm^{-1}, C–H vibration of methylene groups around 2850 cm^{-1} and Fermi-resonance of methyl groups near 2930 cm^{-1} [**?**, 224]. When engaging in nonlinear imaging, one needs to consider several factors. For instance, penetration depth, for which longer wavelengths are suited and the cavity should be resonant for idler instead of signal. Another crucial aspect is evaluating the potential damage to the sample caused by light (phototoxicity) and its tolerance to damage, which depends on both the peak power of the laser pulses and factors like repetition rate and pulse duration. These parameters require careful adjustment. Typically, lower repetition rate laser systems are preferred for such applications [**?**]. However, this preference for lower repetition rates does reduce the speed of imaging. Another vital factor is the spectral resolution, which is influenced by the width of the laser's spectrum. A narrower spectrum leads to enhanced resolution. In our setup, operating within a narrow bandwidth is optimal for achieving high-resolution imaging while a high repetition rate will ensure fast imaging.

Supercontinuum generation

As discussed in the previous chapter, the fiber optical parametric oscillator (FOPO) has the capability to generate a supercontinuum, even employing picosecond pulses. However, to achieve an effective supercontinuum generation, it is essential to increase the fiber's length and employ femtosecond (fs) pulses close to the zero dispersion wavelength of the photonic crystal fiber [89]. While our seed fiber laser can be extended to operate in the fs regime, this extension necessitates externally compressing the pulses, adding further complexities to the laser system.

Possible improvements in the fiber laser and the fiber OPO

This section will briefly explain the possible improvements in both the ANDi fiber laser and the fiber OPO. Currently, a primary drawback of the ANDi fiber laser is its bulky size, which needs to be reduced. Achieving this reduction in size can be accomplished through the utilization of LMA fiber within round tubing with passive cooling, resulting in a reduction of the overall laser cavity. Another crucial enhancement for the ANDi fiber laser involves the fast tuning of the central wavelength and the spectral width. Currently, both the central wavelength and spectral width are manually adjusted, but there is a potential for improvement through electronic adjustments.

In the context of upgrading fiber OPO, potential improvements include transitioning to a watt-level system, achievable through using LMA photonic crystal fiber. Another possible advancement involves creating a more compact fiber OPO cavity, which can be realized by minimizing the free space within the cavity through the incorporation of hollow-core fiber. However, it is important to note that when utilizing hollow-core fiber, managing the polarization of light during propagation presents additional challenges. Moreover, a significant enhancement can be attained by implementing an electronic system for swiftly adjusting the delay line.

Appendix A

Equations for parametric amplification

Maximum parametric amplification

The amplification factor of the signal is given as,

$$G_s = \frac{P_s(L)}{P_s(0)} = \left[1 + \left(1 + \frac{\kappa^2}{4g^2}\right)\sinh^2(gL)\right], \tag{A.1}$$

where g is the parametric gain and κ is the phase mismatch term. The parametric gain g for the degenerate pump case can be written as

$$g = \sqrt{(\gamma P_p)^2 - \left(\frac{\kappa}{2}\right)^2}. \tag{A.2}$$

For perfect phase matching ($\kappa \approx 0$), where the amplification is maximum, the parametric gain $g = \gamma P_p$ and Eq. A.1 becomes,

$$G_s = 1 + \sinh^2(gL) \approx \sinh^2(gL). \tag{A.3}$$

This Equation can be written as,

$$G_s = \frac{1}{4}[\exp(\gamma P_p L) - \exp(-\gamma P_p L)]^2. \tag{A.4}$$

Then expanding the above equation, we get:

$$G_s = \frac{1}{4}[\exp(2\gamma P_p L) + \exp(-2\gamma P_p L) - 2]. \tag{A.5}$$

The last two terms of the above equation are comparatively negligible so this can be written as,

$$G_s \approx \frac{1}{4}[\exp(2\gamma P_p L)]. \tag{A.6}$$

Parametric amplification near pump wavelength

For the amplification factor near the pump wavelength ($\Delta\beta \approx 0$ which means $\kappa \approx 2\gamma P_p$),

$$G_s \approx \left[1 + \left(1 + \frac{\kappa^2}{4g^2}\right)\sinh^2(gL)\right], \tag{A.7}$$

which becomes

$$G_s \approx 1 + \left[1 + \left(\frac{\gamma P_p}{g}\right)^2\right]\sinh^2(gL). \tag{A.8}$$

The above equation can be expanded in Taylor form as,

$$G_s \approx 1 + \left[1 + \left(\frac{\gamma P_p}{g}\right)^2\right]\left[gL + \frac{(gL)^3}{3!} + \frac{(gL)^5}{5!} + ...\right]^2. \tag{A.9}$$

This can be written as,

$$G_s \approx 1 + \left(1 + (\gamma P_p L)^2\right) \left[1 + \frac{(gL)^2}{6} + \frac{(gL)^4}{120} + ...\right]^2 . \tag{A.10}$$

As $\kappa \approx 2\gamma P_p$, which means that $g \approx 0$, this equation simplifies further and taking into account that $\gamma P_p L >> 1$, we obtain:

$$G_s \approx (\gamma P_p L)^2. \tag{A.11}$$

Bibliography

[1] H.A. Haus. Mode-locking of lasers. *IEEE Journal of Selected Topics in Quantum Electronics*, 6(6):1173–1185, November 2000.

[2] Martin E. Fermann and Ingmar Hartl. Ultrafast fibre lasers. *Nature Photonics*, 7(11):868–874, November 2013.

[3] A. B. Grudinin, D. J. Richardson, and D. N. Payne. Energy quantisation in figure eight fibre laser. *Electronics Letters*, 28:67, January 1992.

[4] H.A. Haus, K. Tamura, L.E. Nelson, and E.P. Ippen. Stretched-pulse additive pulse mode-locking in fiber ring lasers: Theory and experiment. *IEEE Journal of Quantum Electronics*, 31(3):591–598, March 1995.

[5] F. Ö. Ilday, J. R. Buckley, W. G. Clark, and F. W. Wise. Self-Similar Evolution of Parabolic Pulses in a Laser. *Physical Review Letters*, 92(21):213902, May 2004.

[6] Andy Chong, Joel Buckley, Will Renninger, and Frank Wise. All-normal-dispersion femtosecond fiber laser. *Optics Express*, 14(21):10095–10100, October 2006.

[7] Andy Chong, William H. Renninger, and Frank W. Wise. All-normal-dispersion femtosecond fiber laser with pulse energy above 20nJ. *Optics Letters*, 32(16):2408–2410, August 2007.

[8] Bülend Ortaç, Jens Limpert, and Andreas Tünnermann. High-energy femtosecond Yb-doped fiber laser operating in the anomalous dispersion regime. *Optics Letters*, 32(15):2149–2151, August 2007.

[9] B. Ortaç, O. Schmidt, T. Schreiber, J. Limpert, A. Tünnermann, and Ammar Hideur. High-energy femtosecond Yb-doped dispersion compensation free fiber laser. *Optics Express*, 15(17):10725–10732, August 2007.

[10] Caroline Lecaplain, Clovis Chédot, Ammar Hideur, Bülend Ortaç, and Jens Limpert. High-power all-normal-dispersion femtosecond pulse generation from a Yb-doped large-mode-area microstructure fiber laser. *Optics Letters*, 32(18):2738–2740, September 2007.

[11] You-Jian Song, Ming-Lie Hu, Chang-Lei Wang, Zhen Tian, Qi-Rong Xing, Lu Chai, and Ching-Yue Wang. Environmentally Stable, High Pulse Energy Yb-Doped Large-Mode-Area Photonic Crystal Fiber Laser Operating in the Soliton-Like Regime. *IEEE Photonics Technology Letters*, 20(13):1088–1090, July 2008.

[12] Bülend Ortaç, Martin Baumgartl, Jens Limpert, and Andreas Tünnermann. Approaching microjoule-level pulse energy with mode-locked femtosecond fiber lasers. *Optics Letters*, 34(10):1585–1587, May 2009.

[13] Albert Schliesser, Nathalie Picqué, and Theodor W. Hänsch. Mid-infrared frequency combs. *Nature Photonics*, 6(7):440–449, July 2012.

[14] Yasuyuki Ozeki, Wataru Umemura, Yoichi Otsuka, Shuya Satoh, Hiroyuki Hashimoto, Kazuhiko Sumimura, Norihiko Nishizawa, Kiichi Fukui, and Kazuyoshi Itoh. High-speed molecular spectral imaging of tissue with stimulated Raman scattering. *Nature Photonics*, 6(12):845–851, December 2012.

[15] Mario Chemnitz, Martin Baumgartl, Tobias Meyer, Cesar Jauregui, Benjamin Dietzek, Jürgen Popp, Jens Limpert, and Andreas Tünnermann. Widely tuneable fiber optical parametric amplifier for coherent anti-Stokes Raman scattering microscopy. *Optics Express*, 20(24):26583–26595, November 2012.

[16] Thomas Gottschall, Tobias Meyer, Martin Baumgartl, Benjamin Dietzek, Jürgen Popp, Jens Limpert, and Andreas Tünnermann. Fiber-based optical parametric oscillator for high resolution coherent anti-Stokes Raman scattering (CARS) microscopy. *Optics Express*, 22(18):21921–21928, September 2014.

[17] Thomas Gottschall, Tobias Meyer, Martin Baumgartl, Cesar Jauregui, Michael Schmitt, Jürgen Popp, Jens Limpert, and Andreas Tünnermann. Fiber-based light sources for biomedical applications of coherent anti-Stokes Raman scattering microscopy. *Laser & Photonics Reviews*, 9(5):435–451, 2015.

[18] Cihang Kong, Christian Pilger, Henning Hachmeister, Xiaoming Wei, Tom H. Cheung, Cora S. W. Lai, Nikki P. Lee, Kevin K. Tsia, Kenneth K. Y. Wong, and Thomas Huser. High-contrast, fast chemical imaging by coherent Raman scattering using a self-synchronized two-colour fibre laser. *Light: Science & Applications*, 9(1):25, February 2020.

[19] Iñaki Aporta, Maria Ángeles Quintela, and Jose Miguel López-Higuera. Broadband Continuously Tunable All-Fiber Laser Based on OPG for CARS Imaging. *Journal of Lightwave Technology*, 39(8):2489–2496, April 2021.

[20] Hongwei Chen, Shengping Chen, Jianhua Wang, Zilun Chen, and Jing Hou. 35W high power all fiber supercontinuum generation in PCF with picosecond MOPA laser. *Optics Communications*, 284(23):5484–5487, November 2011.

[21] Gys Van der Westhuizen and Johan Nilsson. Fiber Optical Parametric Oscillator for Large Frequency-Shift Wavelength Conversion. *IEEE Journal of Quantum Electronics*, 47(11):1396–1403, November 2011.

[22] John Clowes. Next Generation Light Sources for Biomedical Applications. *Optik & Photonik*, 3(1):36–38, 2008.

[23] Haohua Tu and Stephen A. Boppart. Coherent fiber supercontinuum for biophotonics. *Laser & Photonics Reviews*, 7(5):628–645, 2013.

[24] C. Xu and F. W. Wise. Recent advances in fibre lasers for nonlinear microscopy. *Nature Photonics*, 7(11):875–882, November 2013.

[25] James R. Taylor. Tutorial on fiber-based sources for biophotonic applications. *Journal of Biomedical Optics*, 21(6):061010, June 2016.

[26] Claire Lefort. A review of biomedical multiphoton microscopy and its laser sources*. *Journal of Physics D: Applied Physics*, 50(42):423001, September 2017.

[27] Han Liu, Sijia Sun, Li Zheng, Geyang Wang, Wenlong Tian, Dacheng Zhang, Hainian Han, Jiangfeng Zhu, and Zhiyi Wei. Review of laser-diode pumped Ti:sapphire laser. *Microwave and Optical Technology Letters*, 63(8):2135–2144, 2021.

[28] Norihiko Nishizawa. Ultrashort pulse fiber lasers and their applications. *Japanese Journal of Applied Physics*, 53(9):090101, July 2014.

[29] Chunyang Ma, Ankita Khanolkar, and Andy Chong. High-performance tunable, self-similar fiber laser. *Optics Letters*, 44(5):1234–1236, March 2019.

[30] Christian W. Freudiger, Wenlong Yang, Gary R. Holtom, Nasser Peyghambarian, X. Sunney Xie, and Khanh Q. Kieu. Stimulated Raman scattering microscopy with a robust fibre laser source. *Nature Photonics*, 8(2):153–159, February 2014.

[31] Muhammad Ghawas, Valerian Freysz, Lukas Müller, Sébastien Cassagnère, and Eric Freysz. High power ytterbium rod-type fiber laser delivering tunable picosecond pulses. *Optics Express*, 30(25):44569–44579, December 2022.

[32] H. M. Pask, David C. Hanna, Anne C. Tropper, Colin J. Mackechnie, Paul R. Barber, Judith M. Dawes, and Robert J. Carman. Ytterbium-doped silica fiber lasers: Versatile sources for the 1–1.2 Mm region. *IEEE Journal of Selected Topics in Quantum Electronics*, 1(1):2–13, April 1995.

[33] R. Paschotta, J. Nilsson, A.C. Tropper, and D.C. Hanna. Ytterbium-doped fiber amplifiers. *IEEE Journal of Quantum Electronics*, 33(7):1049–1056, July 1997.

[34] Paola Taroni, Andrea Bassi, Daniela Comelli, Andrea Farina, Rinaldo Cubeddu, and Antonio Pifferi. Diffuse optical spectroscopy of breast tissue extended to 1100 nm. *Journal of Biomedical Optics*, 14(5):054030, September 2009.

[35] Yuan Liu, Haohua Tu, Wladimir A. Benalcazar, Eric J. Chaney, and Stephen A. Boppart. Multimodal Nonlinear Microscopy by Shaping a Fiber Supercontinuum From 900 to 1160 nm. *IEEE Journal of Selected Topics in Quantum Electronics*, 18(3):1209–1214, May 2012.

[36] Wei Liu, Shih-Hsuan Chia, Hsiang-Yu Chung, Rüdiger Greinert, Franz X. Kärtner, and Guoqing Chang. Energetic ultrafast fiber laser sources tunable in 1030–1215 nm for deep tissue multi-photon microscopy. *Optics Express*, 25(6):6822–6831, March 2017.

[37] O. G. Okhotnikov, L. Gomes, N. Xiang, T. Jouhti, and A. B. Grudinin. Mode-locked ytterbium fiber laser tunable in the 980–1070-nm spectral range. *Optics Letters*, 28(17):1522–1524, September 2003.

[38] M. Schultz, H. Karow, D. Wandt, U. Morgner, and D. Kracht. Ytterbium femtosecond fiber laser without dispersion compensation tunable from 1015nm to 1050nm. *Optics Communications*, 282(13):2567–2570, July 2009.

[39] L. J. Kong, X. S. Xiao, and C. X. Yang. Tunable all-normal-dispersion Yb-doped mode-locked fiber lasers. *Laser Physics*, 20(4):834–837, April 2010.

[40] Chunmei Ouyang, Ping Shum, Honghai Wang, Songnian Fu, Xueping Cheng, Jia Haur Wong, and Xiaolong Tian. Wavelength-Tunable High-Energy All-Normal-Dispersion Yb-Doped Mode-Locked All-Fiber Laser With a HiBi Fiber Sagnac Loop Filter. *IEEE Journal of Quantum Electronics*, 47(2):198–203, February 2011.

[41] Lei Hou, Mengmeng Li, Xin He, Qimeng Lin, Hongyu Guo, Baole Lu, Xinyuan Qi, Haowei Chen, and Jintao Bai. Wavelength-tunable dissipative pulses from Yb-doped fiber laser with Sagnac filter. *Laser Physics Letters*, 13(12):125302, November 2016.

[42] Feng Zou, Zhaokun Wang, Ziwei Wang, Yang Bai, Qiurui Li, and Jun Zhou. Widely tunable all-fiber SESAM mode-locked Ytterbium laser with a linear cavity. *Optics & Laser Technology*, 92:133–137, July 2017.

[43] Hongyu Guo, Lei Hou, Yonggang Wang, Jiang Sun, Qimeng Lin, Yang Bai, and Jintao Bai. Tunable Ytterbium-Doped Mode-Locked Fiber Laser Based on Single-Walled Carbon Nanotubes. *Journal of Lightwave Technology*, 37(10):2370–2374, May 2019.

[44] Zhicheng Zhang, Sha Wang, Yongjie Pu, Shaoqian Wang, Huinan Li, and Jun Wang. Improving the formation probability and stability of noise-like pulse by weakening the spectrum filtering effect. *Optics Express*, 30(18):31998–32009, August 2022.

[45] Yangyang Li, Man Jiang, Lei Hou, Jianing Tao, Pengye Song, Baole Lu, and Jintao Bai. Wavelength-tunable dissipative soliton from Yb-doped fiber laser with nonlinear amplifying loop mirror. *Chinese Optics Letters*, 21(6):061402, June 2023.

[46] Guanguang Gao, Shang Wang, Qikai Zhao, Zhenhua Cong, Zhaojun Liu, and Zhigang Zhao. Consecutive 1015–1105-nm wavelength tunable "figure-of-9" mode-locked Yb:fiber oscillator. *Optics Letters*, 47(22):5869–5872, November 2022.

[47] Wu Liu, Jintao Fan, Chen Xie, Youjian Song, Chenlin Gu, Lu Chai, Chingyue Wang, and Minglie Hu. Programmable controlled mode-locked fiber laser using a digital micromirror device. *Optics Letters*, 42(10):1923–1926, May 2017.

[48] Kenneth Underwood and Juliet T. Gopinath. Control of the state of a mode-locked fiber laser using an intracavity Martinez compressor. *Optics Letters*, 41(22):5393–5396, November 2016.

[49] Y. S. Fedotov, S. M. Kobtsev, R. N. Arif, A. G. Rozhin, C. Mou, and S. K. Turitsyn. Spectrum-, pulsewidth-, and wavelength-switchable all-fiber mode-locked Yb laser with fiber based birefringent filter. *Optics Express*, 20(16):17797–17805, July 2012.

[50] Masanori Nishiura and Tatsutoshi Shioda. Wavelength and pulse width programmable mode-locked Yb fiber laser. *Optics Express*, 31(4):5347–5362, February 2023.

[51] Arno Klenke, Cesar Jauregui, Albrecht Steinkopff, Christopher Aleshire, and Jens Limpert. High-power multicore fiber laser systems. *Progress in Quantum Electronics*, 84:100412, June 2022.

[52] Arno Klenke, Albrecht Steinkopff, Christopher Aleshire, Cesar Jauregui, Stefan Kuhn, Johannes Nold, Christian Hupel, Sigrun Hein, Steffen Schulze, Nicoletta Haarlammert, Thomas Schreiber, Andreas Tünnermann, and Jens Limpert. 500 W rod-type 4 × 4 multicore ultrafast fiber laser. *Optics Letters*, 47(2):345–348, January 2022.

[53] A. Klenke, A. Steinkopff, M. Bahri, C. Jauregui, J. Nold, N. Haarlammert, T. Schreiber, A. Tünnermann, and J. Limpert. Rod-type Multicore Fiber with 49 Cores for Coherent Beam Combination of Femtosecond Pulses. In *Laser Congress 2023 (ASSL, LAC) (2023), Paper ATh3A.6*, page ATh3A.6. Optica Publishing Group, October 2023.

[54] H. Lim, J. Buckley, A. Chong, and F. W. Wise. Fibre-based source of femtosecond pulses tunable from 1.0 to 1.3 Mm. *Electronics Letters*, 40(24):1523–1525, November 2004.

[55] Jun Takayanagi, Toshiharu Sugiura, Makoto Yoshida, and Norihiko Nishizawa. 1.0–1.7-μ m Wavelength-Tunable Ultrashort-Pulse Generation Using Femtosecond Yb-Doped Fiber Laser and Photonic Crystal Fiber. *IEEE Photonics Technology Letters*, 18(21):2284–2286, November 2006.

[56] James van Howe, Jennifer H. Lee, Shian Zhou, Frank Wise, Chris Xu, Siddharth Ramachandran, Samir Ghalmi, and Man F. Yan. Demonstration of soliton self-frequency shift below 1300nm in higher-order mode, solid silica-based fiber. *Optics Letters*, 32(4):340–342, February 2007.

[57] Xiao-Hui Fang, Ming-Lie Hu, Bo-Wen Liu, Lu Chai, Ching-Yue Wang, Hui-Feng Wei, Wei-Jun Tong, Jie Luo, Chi-Kuang Sun, Alexander A. Voronin, and Aleksei M.

Zheltikov. An all-photonic-crystal-fiber wavelength-tunable source of high-energy sub-100fs pulses. *Optics Communications*, 289:123–126, February 2013.

[58] Jinkang Lim, Hung-Wen Chen, Shanhui Xu, Zhongmin Yang, Guoqing Chang, and Franz X. Kärtner. 3 GHz, watt-level femtosecond Raman soliton source. *Optics Letters*, 39(7):2060–2063, April 2014.

[59] Yuhong Yao, Govind P. Agrawal, and Wayne H. Knox. Yb:fiber laser-based, spectrally coherent and efficient generation of femtosecond 1.3-Mm pulses from a fiber with two zero-dispersion wavelengths. *Optics Letters*, 40(15):3631–3634, August 2015.

[60] Dinghuan Deng, Tonglei Cheng, Xiaojie Xue, Hoang Tuan Tong, Takenobu Suzuki, and Yasutake Ohishi. Widely tunable soliton self-frequency shift and dispersive wave generation in a highly nonlinear fiber. In *Optical Components and Materials XII*, volume 9359, pages 10–15. SPIE, March 2015.

[61] P. Cadroas, L. Abdeladim, L. Kotov, M. Likhachev, D. Lipatov, D. Gaponov, A. Hideur, M. Tang, J. Livet, W. Supatto, E. Beaurepaire, and S. Février. All-fiber femtosecond laser providing 9 nJ, 50 MHz pulses at 1650 nm for three-photon microscopy. *Journal of Optics*, 19(6):065506, May 2017.

[62] Bo Li, Mengran Wang, Kriti Charan, Ming-jun Li, and Chris Xu. Investigation of the long wavelength limit of soliton self-frequency shift in a silica fiber. *Optics Express*, 26(15):19637–19647, July 2018.

[63] L. Rishøj, B. Tai, P. Kristensen, and S. Ramachandran. Soliton self-mode conversion: Revisiting Raman scattering of ultrashort pulses. *Optica*, 6(3):304–308, March 2019.

[64] Yue Zhou, Kim K. Y. Cheung, Sigang Yang, P. C. Chui, and Kenneth K. Y. Wong. Widely tunable picosecond optical parametric oscillator using highly nonlinear fiber. *Optics Letters*, 34(7):989–991, April 2009.

[65] Maximilian Brinkmann, Alexander Fast, Tim Hellwig, Isaac Pence, Conor L. Evans, and Carsten Fallnich. Portable all-fiber dual-output widely tunable light source for coherent Raman imaging. *Biomedical Optics Express*, 10(9):4437–4449, September 2019.

[66] Kangwen Yang, Jieshi Jiang, Zhengru Guo, Qiang Hao, and Heping Zeng. Tunable Femtosecond Laser From 965 to 1025 nm in Fiber Optical Parametric Oscillator. *IEEE Photonics Technology Letters*, 30(7):607–610, April 2018.

[67] F. M. Mitschke and L. F. Mollenauer. Discovery of the soliton self-frequency shift. *Optics Letters*, 11(10):659–661, October 1986.

[68] N. Nishizawa and T. Goto. Widely wavelength-tunable ultrashort pulse generation using polarization maintaining optical fibers. *IEEE Journal of Selected Topics in Quantum Electronics*, 7(4):518–524, July 2001.

[69] D. A. Sidorov-Biryukov, K. A. Kudinov, A. A. Podshivalov, and A. M. Zheltikov. Widely tunable 70-MHz near-infrared source of ultrashort pulses based on a mode-locked ytterbium laser and a photonic-crystal fiber. *Laser Physics Letters*, 7(5):355, March 2010.

[70] R. Stolen and J. Bjorkholm. Parametric amplification and frequency conversion in optical fibers. *IEEE Journal of Quantum Electronics*, 18(7):1062–1072, July 1982.

[71] D. Nodop, C. Jauregui, D. Schimpf, J. Limpert, and A. Tünnermann. Efficient high-power generation of visible and mid-infrared light by degenerate four-wave-mixing in a large-mode-area photonic-crystal fiber. *Optics Letters*, 34(22):3499–3501, November 2009.

[72] John M. Dudley and J. Roy Taylor. Ten years of nonlinear optics in photonic crystal fibre. *Nature Photonics*, 3(2):85–90, February 2009.

[73] Martin Baumgartl, Thomas Gottschall, Javier Abreu-Afonso, Antonio Díez, Tobias Meyer, Benjamin Dietzek, Manfred Rothhardt, Jürgen Popp, Jens Limpert, and

Andreas Tünnermann. Alignment-free, all-spliced fiber laser source for CARS microscopy based on four-wave-mixing. *Optics Express*, 20(19):21010–21018, September 2012.

[74] Thomas Gottschall, Tobias Meyer, Michael Schmitt, Jürgen Popp, Jens Limpert, and Andreas Tünnermann. Four-wave-mixing-based optical parametric oscillator delivering energetic, tunable, chirped femtosecond pulses for non-linear biomedical applications. *Optics Express*, 23(18):23968–23977, September 2015.

[75] Hideharu Mikami, Manabu Shiozawa, Masataka Shirai, and Koichi Watanabe. Compact light source for ultrabroadband coherent anti-Stoke Raman scattering (CARS) microscopy. *Optics Express*, 23(3):2872–2878, February 2015.

[76] Thomas Gottschall, Tobias Meyer, Cesar Jauregui, Florian Just, Tino Eidam, Michael Schmitt, Jürgen Popp, Jens Limpert, and Andreas Tünnermann. All-fiber optical parametric oscillator for bio-medical imaging applications. In *Fiber Lasers XIV: Technology and Systems*, volume 10083, pages 252–255. SPIE, February 2017.

[77] Kangwen Yang, Yuxing Wu, Jieshi Jiang, Pengbo Ye, Kun Huang, Qiang Hao, and Heping Zeng. Fiber Optical Parametric Oscillator and Amplifier for CARS Spectroscopy. *IEEE Photonics Technology Letters*, 30(10):967–970, May 2018.

[78] Govind P. Agrawal. *Nonlinear Fiber Optics*. Academic Press, 5th edition, 2013.

[79] Jay E. Sharping, Mark A. Foster, Alexander L. Gaeta, Jacob Lasri, Ove Lyngnes, and Kurt Vogel. Octave-spanning, high-power microstructure-fiber-based optical parametric oscillators. *Optics Express*, 15(4):1474–1479, February 2007.

[80] Florian Tauser, Florian Adler, and Alfred Leitenstorfer. Widely tunable sub-30-fs pulses from a compact erbium-doped fiber source. *Optics Letters*, 29(5):516–518, March 2004.

[81] Hung-Wen Chen, Zia Haider, JinKang Lim, Shanhui Xu, Zhongmin Yang, Franz X. Kärtner, and Guoqing Chang. 3 GHz, Yb-fiber laser-based, few-cycle ultrafast source

at the Ti:sapphire laser wavelength. *Optics Letters*, 38(22):4927–4930, November 2013.

[82] Haohua Tu, Jesper Lægsgaard, Rui Zhang, Shi Tong, Yuan Liu, and Stephen A. Boppart. Bright broadband coherent fiber sources emitting strongly blue-shifted resonant dispersive wave pulses. *Optics Express*, 21(20):23188–23196, October 2013.

[83] Ming-Che Chan, Chi-Hsiang Lien, Jyan-Yo Lu, and Bo-Han Lyu. High power NIR fiber-optic femtosecond Cherenkov radiation and its application on nonlinear light microscopy. *Optics Express*, 22(8):9498–9507, April 2014.

[84] Kuen-Che Li, Lynn L. H. Huang, Jhih-Hao Liang, and Ming-Che Chan. Simple approach to three-color two-photon microscopy by a fiber-optic wavelength convertor. *Biomedical Optics Express*, 7(11):4803–4815, November 2016.

[85] Wei Liu, Chen Li, Zhigang Zhang, Franz X. Kärtner, and Guoqing Chang. Self-phase modulation enabled, wavelength-tunable ultrafast fiber laser sources: An energy scalable approach. *Optics Express*, 24(14):15328–15340, July 2016.

[86] Hsiang-Yu Chung, Wei Liu, Qian Cao, Franz X. Kärtner, and Guoqing Chang. Er-fiber laser enabled, energy scalable femtosecond source tunable from 1.3 to 1.7 Mm. *Optics Express*, 25(14):15760–15771, July 2017.

[87] Hsiang-Yu Chung, Wei Liu, Qian Cao, Liwei Song, Franz X. Kärtner, and Guoqing Chang. Megawatt peak power tunable femtosecond source based on self-phase modulation enabled spectral selection. *Optics Express*, 26(3):3684–3695, February 2018.

[88] Fuzeng Niu, Jiayin Li, Wan Yang, Zhigang Zhang, and Aimin Wang. Fiber-Based High-Energy Femtosecond Pulses Tunable From 920 to 1030 nm for Two-Photon Microscopy. *IEEE Photonics Technology Letters*, 30(16):1479–1482, August 2018.

[89] John M. Dudley, Goëry Genty, and Stéphane Coen. Supercontinuum generation in photonic crystal fiber. *Reviews of Modern Physics*, 78(4):1135–1184, October 2006.

[90] Jacek Swiderski. High-power mid-infrared supercontinuum sources: Current status and future perspectives. *Progress in Quantum Electronics*, 38(5):189–235, September 2014.

[91] A. E. Siegman. *Lasers*. University Science Books, 1986.

[92] Orazio Svelto. Introductory Concepts. In Orazio Svelto, editor, *Principles of Lasers*, pages 1–15. Springer US, Boston, MA, 2010.

[93] Albert Einstein. Zur Quantentheorie der Strahlung. *Physikalische Zeitschrift*, 18:121–128, January 1917.

[94] J. P. Gordon, H. J. Zeiger, and C. H. Townes. Molecular Microwave Oscillator and New Hyperfine Structure in the Microwave Spectrum of NH3. *Physical Review*, 95(1):282–284, July 1954.

[95] A. L. Schawlow and C. H. Townes. Infrared and Optical Masers. *Physical Review*, 112(6):1940–1949, December 1958.

[96] T. H. Maiman. Stimulated Optical Radiation in Ruby. *Nature*, 187:493–494, August 1960.

[97] Rodica M. Martin. *Reciprocity between Emission and Absorption for Rare Earth Ions in Glass*. Worcester Polytechnic Institute, 2006.

[98] M. Weber, J. Lynch, D. Blackburn, and D. Cronin. Dependence of the stimulated emission cross section of Yb3+ on host glass composition. *IEEE Journal of Quantum Electronics*, 19(10):1600–1608, October 1983.

[99] Hiromichi Takebe, Takahiro Murata, and Kenji Morinaga. Compositional Dependence of Absorption and Fluorescence of Yb3+ in Oxide Glasses. *Journal of the American Ceramic Society*, 79(3):681–687, 1996.

[100] D. E. McCumber. Einstein Relations Connecting Broadband Emission and Absorption Spectra. *Physical Review*, 136(4A):A954–A957, November 1964.

[101] V. V. Ter-Mikirtychev. Optical Spectroscopy of Rare-Earth Ions in the Solid State. In John C. Lindon, George E. Tranter, and David W. Koppenaal, editors, *Encyclopedia of Spectroscopy and Spectrometry (Third Edition)*, pages 481–491. Academic Press, Oxford, January 2017.

[102] Van Heel and A. C. S. A New Method of transporting Optical Images without Aberrations. *Nature*, 173(4392):39–39, January 1954.

[103] Lawrence E. Curtiss. Glass fiber optical devices, June 1971.

[104] D. Keck and P. Schultz. Method of producing optical waveguide fibers, January 1973.

[105] W. G. French, J. B. MacChesney, P. B. O'Connor, and G. W. Tasker. Optical Waveguides With Very Low Losses. *Bell System Technical Journal*, 53(5):951–954, 1974.

[106] Jonathan C. Knight. Photonic crystal fibres. *Nature*, 424(6950):847–851, August 2003.

[107] A. Ortigosa-Blanch, J. C. Knight, W. J. Wadsworth, J. Arriaga, B. J. Mangan, T. A. Birks, and P. St J. Russell. Highly birefringent photonic crystal fibers. *Optics Letters*, 25(18):1325–1327, September 2000.

[108] T. A. Birks, J. C. Knight, and P. St J. Russell. Endlessly single-mode photonic crystal fiber. *Optics Letters*, 22(13):961–963, July 1997.

[109] Philip Russell. Photonic Crystal Fibers. *Science*, 299(5605):358–362, January 2003.

[110] Philip St J. Russell. Photonic-Crystal Fibers. *Journal of Lightwave Technology*, 24(12):4729–4749, December 2006.

[111] J.C. Knight, J. Arriaga, T.A. Birks, A. Ortigosa-Blanch, W.J. Wadsworth, and P.St.J. Russell. Anomalous dispersion in photonic crystal fiber. *IEEE Photonics Technology Letters*, 12(7):807–809, July 2000.

[112] Jinendra K. Ranka, Robert S. Windeler, and Andrew J. Stentz. Optical properties of high-delta air–silica microstructure optical fibers. *Optics Letters*, 25(11):796–798, June 2000.

[113] W. H. Reeves, D. V. Skryabin, F. Biancalana, J. C. Knight, P. St J. Russell, F. G. Omenetto, A. Efimov, and A. J. Taylor. Transformation and control of ultra-short pulses in dispersion-engineered photonic crystal fibres. *Nature*, 424(6948):511–515, July 2003.

[114] Colin S. Willett. *Introduction to Gas Lasers: Population Inversion Mechanisms: With Emphasis on Selective Excitation Processes*. Elsevier, May 2014.

[115] Fritz P. Schäfer. Principles of Dye Laser Operation. In Fritz Peter Schäfer, editor, *Dye Lasers*, Topics in Applied Physics, pages 1–85. Springer, Berlin, Heidelberg, 1973.

[116] Weng W. Chow and Stephan W. Koch. Applications. In Weng W. Chow and Stephan W. Koch, editors, *Semiconductor-Laser Fundamentals: Physics of the Gain Materials*, pages 196–233. Springer, Berlin, Heidelberg, 1999.

[117] Jerome Moloney, Jorg Hader, and Stephan Koch. Quantum design of semiconductor active materials: Laser and amplifier applications. *Laser & Photonics Reviews*, 1:24–43, February 2007.

[118] D. S. Funk, J. W. Carlson, and J. G. Eden. Ultraviolet (381 nm), room temperature laser in neodymium-doped fluorozirconate fibre. *Electronics Letters*, 30(22):1859–1860, October 1994.

[119] R. G. Smart, D. C. Hanna, A. C. Tropper, S. T. Davey, S. F. Carter, and D. Szebesta. Cw room temperature upconversion lasing at blue, green and red wavelengths in infrared-pumped Pr3+-doped fluoride fibre. *Electronics Letters*, 27(14):1307–1309, July 1991.

[120] J. Y. Allain, M. Monerie, and H. Poignant. Tunable CW lasing around 610, 635, 695, 715, 885 and 910 nm in praseodymium-doped fluorozirconate fibre. *Electronics Letters*, 27(2):189–191, January 1991.

[121] J. Nilsson, W. A. Clarkson, R. Selvas, J. K. Sahu, P. W. Turner, S. U. Alam, and A. B. Grudinin. High-power wavelength-tunable cladding-pumped rare-earth-doped silica fiber lasers. *Optical Fiber Technology*, 10(1):5–30, January 2004.

[122] Peter F. Moulton, Glen A. Rines, Evgueni V. Slobodtchikov, Kevin F. Wall, Gavin Frith, Bryce Samson, and Adrian L. G. Carter. Tm-Doped Fiber Lasers: Fundamentals and Power Scaling. *IEEE Journal of Selected Topics in Quantum Electronics*, 15(1):85–92, January 2009.

[123] Xiushan Zhu and N. Peyghambarian. High-Power ZBLAN Glass Fiber Lasers: Review and Prospect. *Advances in OptoElectronics*, 2010:e501956, March 2010.

[124] Jean-Claude Diels and Wolfgang Rudolph. *Ultrashort Laser Pulse Phenomena: Fundamentals, Techniques, and Applications on a Femtosecond Time Scale*. Academic Press, 1996.

[125] L. E. Hargrove, R. L. Fork, and M. A. Pollack. Locking of He–Ne laser modes induced by synchronous intracavity modulation. *Applied Physics Letters*, 5(1):4–5, July 1964.

[126] Amnon Yariv. Internal Modulation in Multimode Laser Oscillators. *Journal of Applied Physics*, 36(2):388–391, February 1965.

[127] D. Kuizenga and A. Siegman. FM and AM mode locking of the homogeneous laser - Part I: Theory. *IEEE Journal of Quantum Electronics*, 6(11):694–708, November 1970.

[128] M. Crowell. Characteristics of mode-coupled lasers. *IEEE Journal of Quantum Electronics*, 1(1):12–20, April 1965.

[129] A. J. DeMaria, D. A. Stetser, and H. Heynau. Self mode-locking of lasers with saturable absorbers. *Applied Physics Letters*, 8(7):174–176, April 1966.

[130] E.p. Ippen, C.v. Shank, and A. Dienes. Passive mode locking of the cw dye laser. *Applied Physics Letters*, 21(8):348–350, October 1972.

[131] Hermann A. Haus. Theory of mode locking with a fast saturable absorber. *Journal of Applied Physics*, 46(7):3049–3058, July 1975.

[132] H. Haus. Parameter ranges for CW passive mode locking. *IEEE Journal of Quantum Electronics*, 12(3):169–176, March 1976.

[133] K. Sala, M. Richardson, and N. Isenor. Passive mode locking of lasers with the optical Kerr effect modulator. *IEEE Journal of Quantum Electronics*, 13(11):915–924, November 1977.

[134] E. P. Ippen, D. J. Eilenberger, and R. W. Dixon. Picosecond pulse generation by passive mode locking of diode lasers. *Applied Physics Letters*, 37(3):267–269, August 1980.

[135] O. E. Martinez, R. L. Fork, and J. P. Gordon. Theory of passively mode-locked lasers including self-phase modulation and group-velocity dispersion. *Optics Letters*, 9(5):156–158, May 1984.

[136] H. A. Haus, J. G. Fujimoto, and E. P. Ippen. Structures for additive pulse mode locking. *JOSA B*, 8(10):2068–2076, October 1991.

[137] E. P. Ippen. Principles of passive mode locking. *Applied Physics B*, 58(3):159–170, March 1994.

[138] F. X. Kärtner and U. Keller. Stabilization of solitonlike pulses with a slow saturable absorber. *Optics Letters*, 20(1):16–18, January 1995.

[139] R. Paschotta and U. Keller. Passive mode locking with slow saturable absorbers. *Applied Physics B*, 73(7):653–662, November 2001.

[140] U. Keller, K.J. Weingarten, F.X. Kartner, D. Kopf, B. Braun, I.D. Jung, R. Fluck, C. Honninger, N. Matuschek, and J. Aus der Au. Semiconductor saturable absorber mirrors (SESAM's) for femtosecond to nanosecond pulse generation in solid-state lasers. *IEEE Journal of Selected Topics in Quantum Electronics*, 2(3):435–453, September 1996.

[141] P. T. Guerreiro, S. Ten, N. F. Borrelli, J. Butty, G. E. Jabbour, and N. Peyghambarian. PbS quantum-dot doped glasses as saturable absorbers for mode locking of a Cr:forsterite laser. *Applied Physics Letters*, 71(12):1595–1597, September 1997.

[142] S.Y. Set, H. Yaguchi, Y. Tanaka, and M. Jablonski. Laser mode locking using a saturable absorber incorporating carbon nanotubes. *Journal of Lightwave Technology*, 22(1):51–56, January 2004.

[143] Andreas Schmidt, Simon Rivier, Günter Steinmeyer, Jong Hyuk Yim, Won Bae Cho, Soonil Lee, Fabian Rotermund, Maria C. Pujol, Xavier Mateos, Magdalena Aguiló, Francesc Díaz, Valentin Petrov, and Uwe Griebner. Passive mode locking of Yb:KLuW using a single-walled carbon nanotube saturable absorber. *Optics Letters*, 33(7):729–731, April 2008.

[144] Fumio Shohda, Takafumi Shirato, Masataka Nakazawa, Junji Mata, and Jun Tsukamoto. 147 fs, 51 MHz soliton fiber laser at 1.56 Mm with a fiber-connector-type SWNT/P3HT saturable absorber. *Optics Express*, 16(25):20943–20948, December 2008.

[145] V. V. Dvoyrin, V. M. Mashinsky, and E. M. Dianov. Yb-Bi pulsed fiber lasers. *Optics Letters*, 32(5):451–453, March 2007.

[146] T. Brabec, Ch Spielmann, P. F. Curley, and F. Krausz. Kerr lens mode locking. *Optics Letters*, 17(18):1292–1294, September 1992.

[147] J. Mark, L. Y. Liu, K. L. Hall, H. A. Haus, and E. P. Ippen. Femtosecond pulse generation in a laser with a nonlinear external resonator. *Optics Letters*, 14(1):48–50, January 1989.

[148] N. J. Doran and David Wood. Nonlinear-optical loop mirror. *Optics Letters*, 13(1):56–58, January 1988.

[149] Jan Szczepanek, Tomasz M. Kardaś, Maria Michalska, Czesław Radzewicz, and Yuriy Stepanenko. Simple all-PM-fiber laser mode-locked with a nonlinear loop mirror. *Optics Letters*, 40(15):3500–3503, August 2015.

[150] M. J. Guy, D. U. Noske, and J. R. Taylor. Generation of femtosecond soliton pulses by passive mode locking of an ytterbium-erbium figure-of-eight fiber laser. *Optics Letters*, 18(17):1447–1449, September 1993.

[151] Miro Erkintalo, Claude Aguergaray, Antoine Runge, and Neil G. R. Broderick. Environmentally stable all-PM all-fiber giant chirp oscillator. *Optics Express*, 20(20):22669–22674, September 2012.

[152] M. E. Fermann, M. J. Andrejco, Y. Silberberg, and M. L. Stock. Passive mode locking by using nonlinear polarization evolution in a polarization-maintaining erbium-doped fiber. *Optics Letters*, 18(11):894–896, June 1993.

[153] V. J. Matsas, T. P. Newson, D. J. Richardson, and D. N. Payne. Selfstarting passively mode-locked fibre ring soliton laser exploiting nonlinear polarisation rotation. *Electronics Letters*, 28(15):1391–1393, July 1992.

[154] K. Tamura, H. A. Haus, and E. P. Ippen. Self-starting additive pulse mode-locked erbium fibre ring laser. *Electronics Letters*, 28(24):2226–2228, November 1992.

[155] M. Hofer, M.H. Ober, F. Haberl, and M.E. Fermann. Characterization of ultrashort pulse formation in passively mode-locked fiber lasers. *IEEE Journal of Quantum Electronics*, 28(3):720–728, March 1992.

[156] L. E. Nelson, E. P. Ippen, and H. A. Haus. Broadly tunable sub-500 fs pulses from an additive-pulse mode-locked thulium-doped fiber ring laser. *Applied Physics Letters*, 67(1):19–21, July 1995.

[157] L.E. Nelson, D.J. Jones, K. Tamura, H.A. Haus, and E.P. Ippen. Ultrashort-pulse fiber ring lasers. *Applied Physics B*, 65(2):277–294, August 1997.

[158] A.D. Kim, J.N. Kutz, and D.J. Muraki. Pulse-train uniformity in optical fiber lasers passively mode-locked by nonlinear polarization rotation. *IEEE Journal of Quantum Electronics*, 36(4):465–471, April 2000.

[159] Chin Yu Chong. Femtosecond fiber lasers and amplifiers based on the pulse propagation at normal dispersion. May 2008.

[160] T. Miya, Y. Terunuma, T. Hosaka, and T. Miyashita. Ultimate low-loss single-mode fibre at 1.55 micron. *Electronics Letters*, 15:106–108, February 1979.

[161] Fujio Shimizu. Frequency Broadening in Liquids by a Short Light Pulse. *Physical Review Letters*, 19(19):1097–1100, November 1967.

[162] T. K. Gustafson, J. P. Taran, H. A. Haus, J. R. Lifsitz, and P. L. Kelley. Self-Modulation, Self-Steepening, and Spectral Development of Light in Small-Scale Trapped Filaments. *Physical Review*, 177(1):306–313, January 1969.

[163] R. R. Alfano and S. L. Shapiro. Direct Distortion of Electronic Clouds of Rare-Gas Atoms in Intense Electric Fields. *Physical Review Letters*, 24(22):1217–1220, June 1970.

[164] E. P. Ippen, C. V. Shank, and T. K. Gustafson. Self-phase modulation of picosecond pulses in optical fibers. *Applied Physics Letters*, 24(4):190–192, February 1974.

[165] Robert A. Fisher and William K. Bischel. Numerical studies of the interplay between self-phase modulation and dispersion for intense plane-wave laser pulses. *Journal of Applied Physics*, 46(11):4921–4934, November 1975.

[166] R. H. Stolen and Chinlon Lin. Self-phase-modulation in silica optical fibers. *Physical Review A*, 17(4):1448–1453, April 1978.

[167] Huai Wei, Bin Li, Wei Shi, Xiushan Zhu, Robert A. Norwood, Nasser Peyghambarian, and Shuisheng Jian. General description and understanding of the nonlinear dynamics of mode-locked fiber lasers. *Scientific Reports*, 7(1):1292, May 2017.

[168] A. Hasegawa and F. Tappert. Transmission of stationary nonlinear optical pulses in dispersive dielectric fibers. I. Anomalous dispersion. *Applied Physics Letters*, 23(3):142–144, 1973.

[169] L. F. Mollenauer, R. H. Stolen, and J. P. Gordon. Experimental Observation of Picosecond Pulse Narrowing and Solitons in Optical Fibers. *Physical Review Letters*, 45(13):1095–1098, September 1980.

[170] Yuji Kodama. Optical solitons in a monomode fiber. *Journal of Statistical Physics*, 39(5):597–614, June 1985.

[171] J. P. Gordon. Theory of the soliton self-frequency shift. *Optics Letters*, 11(10):662–664, October 1986.

[172] Y. Kodama and A. Hasegawa. Nonlinear pulse propagation in a monomode dielectric guide. *IEEE Journal of Quantum Electronics*, 23(5):510–524, May 1987.

[173] Curtis R. Menyuk. Stability of solitons in birefringent optical fibers. I: Equal propagation amplitudes. *Optics Letters*, 12(8):614–616, August 1987.

[174] J. P. Gordon. Dispersive perturbations of solitons of the nonlinear Schrödinger equation. *JOSA B*, 9(1):91–97, January 1992.

[175] J. N. Elgin. Soliton propagation in an optical fiber with third-order dispersion. *Optics Letters*, 17(20):1409–1410, October 1992.

[176] D. Anderson, M. Desaix, M. Lisak, and M. L. Quiroga–Teixeiro. Wave breaking in nonlinear-optical fibers. *JOSA B*, 9(8):1358–1361, August 1992.

[177] K. Tamura, E. P. Ippen, H. A. Haus, and L. E. Nelson. 77-fs pulse generation from a stretched-pulse mode-locked all-fiber ring laser. *Optics Letters*, 18(13):1080, July 1993.

[178] S. Wabnitz. Stabilization of sliding-filtered soliton wavelength division multiplexing transmissions by dispersion-compensating fibers. *Optics Letters*, 21(9):638–640, May 1996.

[179] N.J. Smith, N.J. Doran, W. Forysiak, and F.M. Knox. Soliton transmission using periodic dispersion compensation. *Journal of Lightwave Technology*, 15(10):1808–1822, October 1997.

[180] William H. Renninger, Andy Chong, and Frank W. Wise. Pulse Shaping and Evolution in Normal-Dispersion Mode-Locked Fiber Lasers. *IEEE journal of selected topics in quantum electronics : a publication of the IEEE Lasers and Electro-optics Society*, 18(1):389–398, 2012.

[181] S. Boscolo, S. K. Turitsyn, V. Yu. Novokshenov, and J. H. B. Nijhof. Self-Similar Parabolic Optical Solitary Waves. *Theoretical and Mathematical Physics*, 133(3):1647–1656, December 2002.

[182] D. Anderson, M. Desaix, M. Karlsson, M. Lisak, and M. L. Quiroga-Teixeiro. Wave-breaking-free pulses in nonlinear-optical fibers. *JOSA B*, 10(7):1185–1190, July 1993.

[183] N. Akhmediev and A. Ankiewicz. Dissipative Solitons in the Complex Ginzburg-Landau and Swift-Hohenberg Equations. In Nail Akhmediev and Adrian Ankiewicz, editors, *Dissipative Solitons*, Lecture Notes in Physics, pages 1–17. Springer, Berlin, Heidelberg, 2005.

[184] Sergei K. Turitsyn, Brandon G. Bale, and Mikhail P. Fedoruk. Dispersion-managed solitons in fibre systems and lasers. *Physics Reports*, 521(4):135–203, December 2012.

[185] V. I. Kruglov, A. C. Peacock, J. M. Dudley, and J. D. Harvey. Self-similar propagation of high-power parabolic pulses in optical fiber amplifiers. *Optics Letters*, 25(24):1753–1755, December 2000.

[186] Andy Chong, William H. Renninger, and Frank W. Wise. Properties of normal-dispersion femtosecond fiber lasers. *JOSA B*, 25(2):140–148, February 2008.

[187] A. Fernandez, T. Fuji, A. Poppe, A. Fürbach, F. Krausz, and A. Apolonski. Chirped-pulse oscillators: A route to high-power femtosecond pulses without external amplification. *Optics Letters*, 29(12):1366–1368, June 2004.

[188] N. Akhmediev, J. M. Soto-Crespo, and Ph. Grelu. Roadmap to ultra-short record high-energy pulses out of laser oscillators. *Physics Letters A*, 372(17):3124–3128, April 2008.

[189] F.w. Wise, A. Chong, and W.h. Renninger. High-energy femtosecond fiber lasers based on pulse propagation at normal dispersion. *Laser & Photonics Reviews*, 2(1-2):58–73, 2008.

[190] Nicolaas Bloembergen. Nonlinear Optics and Spectroscopy. *Science*, 216(4550):1057–1064, June 1982.

[191] R.W. Tkach, A.R. Chraplyvy, F. Forghieri, A.H. Gnauck, and R.M. Derosier. Four-photon mixing and high-speed WDM systems. *Journal of Lightwave Technology*, 13(5):841–849, May 1995.

[192] K. O. Hill, D. C. Johnson, B. S. Kawasaki, and R. I. MacDonald. Cw three-wave mixing in single-mode optical fibers. *Journal of Applied Physics*, 49(10):5098–5106, October 1978.

[193] N. Bloembergen. Conservation laws in nonlinear optics*. *JOSA*, 70(12):1429–1436, December 1980.

[194] Robert W. Boyd. *Nonlinear Optics*. Academic Press, March 2020.

[195] F. Biancalana, D. V. Skryabin, and P. St. J. Russell. Four-wave mixing instabilities in photonic-crystal and tapered fibers. *Physical Review E*, 68(4):046603, October 2003.

[196] John D. Harvey, Rainer Leonhardt, Stéphane Coen, Gordon K. L. Wong, JonathanC Knight, William J. Wadsworth, and Philip St J. Russell. Scalar modulation instability in the normal dispersion regime by use of a photonic crystal fiber. *Optics Letters*, 28(22):2225–2227, November 2003.

[197] W. J. Wadsworth, N. Joly, J. C. Knight, T. A. Birks, F. Biancalana, and P. St J. Russell. Supercontinuum and four-wave mixing with Q-switched pulses in endlessly single-mode photonic crystal fibres. *Optics Express*, 12(2):299–309, January 2004.

[198] C.L. Tang, W.R. Bosenberg, T. Ukachi, R.J. Lane, and L.K. Cheng. Optical parametric oscillators. *Proceedings of the IEEE*, 80(3):365–374, March 1992.

[199] H. M. van Driel. Synchronously pumped optical parametric oscillators. *Applied Physics B*, 60(5):411–420, May 1995.

[200] Malcolm H. Dunn and Majid Ebrahimzadeh. Parametric Generation of Tunable Light from Continuous-Wave to Femtosecond Pulses. *Science*, 286(5444):1513–1517, November 1999.

[201] Erin S. Lamb, Simon Lefrancois, Minbiao Ji, William J. Wadsworth, X. Sunney Xie, and Frank W. Wise. Fiber optical parametric oscillator for coherent anti-Stokes Raman scattering microscopy. *Optics letters*, 38(20):4154–4157, October 2013.

[202] E. Treacy. Optical pulse compression with diffraction gratings. *IEEE Journal of Quantum Electronics*, 5(9):454–458, September 1969.

[203] Runqin Xu, Fanjiang Xu, Yangrong Song, Lei Duan, Yunbo Song, Shudan Tan, and Zhaohui Liu. Impact of spectral filtering on pulse breaking-up and noise-like pulse generation in all-normal dispersion fiber lasers. *Optics Express*, 28, April 2020.

[204] Stéphane Pitois and Guy Millot. Experimental observation of a new modulational instability spectral window induced by fourth-order dispersion in a normally dispersive single-mode optical fiber. *Optics Communications*, 226(1):415–422, October 2003.

[205] Walter Fu, Robert Herda, and Frank W. Wise. Design guidelines for normal-dispersion fiber optical parametric chirped-pulse amplifiers. *JOSA B*, 37(6):1790–1805, June 2020.

[206] M.E. Marhic, K.K.-Y. Wong, and L.G. Kazovsky. Wide-band tuning of the gain spectra of one-pump fiber optical parametric amplifiers. *IEEE Journal of Selected Topics in Quantum Electronics*, 10(5):1133–1141, September 2004.

[207] M. E. Marhic, N. Kagi, T.-K. Chiang, and L. G. Kazovsky. Broadband fiber optical parametric amplifiers. *Optics Letters*, 21(8):573–575, April 1996.

[208] Coralie Fourcade-Dutin, Olivier Vanvincq, Arnaud Mussot, Emmanuel Hugonnot, and Damien Bigourd. Ultrabroadband fiber optical parametric amplifier pumped by chirped pulses. Part 2: Sub-30-fs pulse amplification at high gain. *JOSA B*, 32(7):1488–1493, July 2015.

[209] Xiaoming Wei, Sisi Tan, Arnaud Mussot, Alexandre Kudlinski, Kevin K. Tsia, and Kenneth K. Y. Wong. 110 nm versatile fiber optical parametric amplifier at 1.0 Mm. *Optics Letters*, 40(17):4090–4093, September 2015.

[210] J. Hansryd, P.A. Andrekson, M. Westlund, Jie Li, and P.-O. Hedekvist. Fiber-based optical parametric amplifiers and their applications. *IEEE Journal of Selected Topics in Quantum Electronics*, 8(3):506–520, May 2002.

[211] M. Horowitz, Y. Barad, and Y. Silberberg. Noiselike pulses with a broadband spectrum generated from an erbium-doped fiber laser. *Optics Letters*, 22(11):799–801, June 1997.

[212] M. Horowitz and Y. Silberberg. Control of noiselike pulse generation in erbium-doped fiber lasers. *IEEE Photonics Technology Letters*, 10(10):1389–1391, October 1998.

[213] D. Y. Tang, L. M. Zhao, and B. Zhao. Soliton collapse and bunched noise-like pulse generation in a passively mode-locked fiber ring laser. *Optics Express*, 13(7):2289–2294, April 2005.

[214] Yueqing Du and Xuewen Shu. Pulse dynamics in all-normal dispersion ultrafast fiber lasers. *JOSA B*, 34(3):553–558, March 2017.

[215] Yuntao Zhou, Xinyu Chu, Yimiu Qian, Chenhao Liang, Andrey Komarov, Xiahui Tang, Ming Tang, Haiyong Zhu, and Luming Zhao. Investigation of noise-like pulse evolution in normal dispersion fiber lasers mode-locked by nonlinear polarization rotation. *Optics Express*, 30(19):35041–35049, September 2022.

[216] I. Hartl, X. D. Li, C. Chudoba, R. K. Ghanta, T. H. Ko, J. G. Fujimoto, J. K. Ranka, and R. S. Windeler. Ultrahigh-resolution optical coherence tomography using continuum generation in an air–silica microstructure optical fiber. *Optics Letters*, 26(9):608–610, May 2001.

[217] S. V. Smirnov, J. D. Ania-Castanon, T. J. Ellingham, S. M. Kobtsev, S. Kukarin, and S. K. Turitsyn. Optical spectral broadening and supercontinuum generation in telecom applications. *Optical Fiber Technology*, 12(2):122–147, April 2006.

[218] Dmitrii A. Sidorov-Biryukov, Evgenii E. Serebryannikov, and Aleksei M. Zheltikov. Time-resolved coherent anti-Stokes Raman scattering with a femtosecond soliton output of a photonic-crystal fiber. *Optics Letters*, 31(15):2323–2325, August 2006.

[219] Th Udem, R. Holzwarth, and T. W. Hänsch. Optical frequency metrology. *Nature*, 416(6877):233–237, March 2002.

[220] R. R. Alfano and S. L. Shapiro. Emission in the Region 4000 to 7000 \AA{} Via Four-Photon Coupling in Glass. *Physical Review Letters*, 24(11):584–587, March 1970.

[221] Jinendra K. Ranka, Robert S. Windeler, and Andrew J. Stentz. Visible continuum generation in air–silica microstructure optical fibers with anomalous dispersion at 800 nm. *Optics Letters*, 25(1):25–27, January 2000.

[222] Xiaobao Liang and Ling Fu. Enhanced Self-Phase Modulation Enables a 700–900 nm Linear Compressible Continuum for Multicolor Two-Photon Microscopy. *IEEE Journal of Selected Topics in Quantum Electronics*, 20(2):42–49, March 2014.

[223] Kun Chen, Tao Wu, Haoyun Wei, and Yan Li. Dual-soliton Stokes-based background-free coherent anti-Stokes Raman scattering spectroscopy and microscopy. *Optics Letters*, 41(11):2628–2631, June 2016.

[224] A. Rygula, K. Majzner, K. M. Marzec, A. Kaczor, M. Pilarczyk, and M. Baranska. Raman spectroscopy of proteins: A review. *Journal of Raman Spectroscopy*, 44(8):1061–1076, 2013.

List of publications in Journals/Conferences

- **M. Ghawas**, O. Zurita-Miranda, V. Freysz, and E. Freysz, "Fiber optical parametric oscillator delivering signal pulse tunable in wavelength and pulse duration," in Conference on Lasers and Electro-Optics/Europe (CLEO/Europe 2023) and European Quantum Electronics Conference (EQEC 2023), Technical Digest Series (Optica Publishing Group, 2023), paper cj-p-15.

- **Muhammad Ghawas**, Valerian Freysz, Lukas Müller, Sébastien Cassagnère, and Eric Freysz, "High power ytterbium rod-type fiber laser delivering tunable picosecond pulses," Opt. Express 30, 44569-44579 (2022).

- **M. Ghawas**, L. Müller, V. Freysz, and E. Freysz, "Self-mode locked ytterbium rod-type fiber laser yielding bandwidth limited and tunable picosecond pulses up to 25 W at 78 MHz," in Laser Congress 2021 (ASSL, LAC), (Optica Publishing Group, 2021), paper JTu1A.6.

Sources picosecondes et femtosecondes à base de fibre dopées ytterbium et applications

Résumé: Les recherches industrielles ou académiques autour laser délivrant des impulsions ultracourtes reposent de plus en plus sur la technologie des lasers à fibre. Elles s'appuient sur les avantages intrinsèques des systèmes à fibre, tels que leur stabilité, compacité, l'excellente qualité modale du faisceau délivré, leur robustesse et leur facilité d'utilisation. Au cours de ce travail, nous avons réalisé l'étude détaillée d'un laser à fibre délivrant des impulsions picosecondes fonctionnant dans un régime de dispersion normale (ANDi). Ce laser a par la suite été déployé pour étudier de la génération paramétrique dans une fibre à cristal photonique. Nous avons tout d'abord développé une source laser à fibre de haute puissance délivrant des impulsions picosecondes dont on peut accorder à la fois la longueur d'onde centrale et la largeur spectrale. À la longueur d'onde centrale de $\sim$ 1030 nm et à un taux de répétition de 78 MHz, ce laser délivre des impulsions picosecondes avec une puissance moyenne allant jusqu'à 25 W. La durée des impulsions peut être ajustée en continu entre $\sim$ 1.8 ps et $\sim$ 4.5 ps alors que l'énergie des impulsions varie entre $\sim$ 320 nJ et $\sim$ 225 nJ. Nous avons également démontré que la longueur d'onde centrale des impulsions laser peut-être finement réglée entre 1010 nm à 1060 nm tout en s'assurant que l'énergie de l'impulsion est supérieure $\sim$ 150 nJ. Les impulsions délivrées par cette source ont été utilisées pour étudier et réaliser un oscillateur paramétrique optique dans une fibre optique. Les ondes signal et idler générées résultent d'un mélange paramétrique à quatre-onde induit dans une fibre à cristal photonique. Cet OPO à fibre est simplement résonnant pour l'onde signal. L'efficacité de conversion pour l'onde signal est proche de 20 %. Le profil de dispersion spectrale de la fibre à cristal photonique et l'accordabilité spectrale de notre laser de pompe nous ont permis de générer des ondes du signal (resp. idler) comprises respectivement entre $\sim$ 770 nm et $\sim$ 1000 nm ($\sim$ 1130 nm et $\sim$ 1590 nm) lorsque la longueur d'onde des impulsions pompe est ajustée entre $\sim$ 1024 nm et $\sim$ 1059 nm.

Mots clés: Picoseconde, haute-puissance, auto-modelocké, laser-fibre, OPO-Fibre

---

Picoseconds and femtoseconds ytterbium fiber laser source and its applications

Abstract: Ultrashort laser pulses in both industrial and research applications progressively rely on fiber laser technology, guided by its intrinsic benefits, for instance, stability, compact nature, excellent beam quality, robustness, and easy operation. In this work, a detailed study has been done to investigate picosecond fiber laser working in an all-normal-dispersion (ANDi) regime for the application of parametric generation in photonic crystal fiber. In summary, we have developed a high-power fiber laser source delivering picosecond pulses with tunability both in central wavelength and spectral width. At the central wavelength of $\sim$ 1030 nm and with a repetition of 78 MHz, this laser delivers picosecond pulses with an average power of up to 25 W. The pulse duration can be continuously adjusted from $\sim$ 1.8 ps to $\sim$ 4.5 ps and pulse energy from $\sim$ 320 nJ and $\sim$ 225 nJ, respectively. Additionally, we have also demonstrated that the central wavelength of the laser pulse can be finely tuned from 1010 nm to 1060 nm while keeping the pulse energy above $\sim$ 150 nJ. The output of this fiber oscillator is propagated through the photonic crystal fiber for the parametric generation of the signal (higher frequencies than the pump) and idler (lower frequencies than the pump). The fiber OPO singly-resonant cavity was built in such a way that only signal wavelengths are allowed to propagate through it. The conversion efficiency for the signal was close to 20 % in the fiber OPO. Based on the dispersion profile of the photonic crystal fiber and our homebuilt tunable pump laser, the signal wavelength (resp. idler) was tuned from $\sim$ 770 nm to $\sim$ 1000 nm ($\sim$ 1130 nm to $\sim$ 1590 nm) for the corresponding pump wavelengths of $\sim$ 1024 nm to $\sim$ 1059 nm.

Keywords: Picosecond, High-power, Self-modelocked, Fiber-laser, Fiber-OPO

Unité de Recherche: LOMA - UMR 5798, Université de Bordeaux, 33405 Talence, France